

**INVESTIGATION OF SPONTANEOUS DIFFERENTIATION OF
NEURAL STEM CELLS ON SYNTHETIC SCAFFOLDS**

A THESIS SUBMITTED TO
GRADUATE SCHOOL OF ENGINEERING AND SCIENCE
OF BILKENT UNIVERSITY
IN PARTIAL FULFILLMENT OF THE REQUIREMENTS
FOR THE DEGREE OF
MASTER OF SCIENCE
IN
NEUROSCIENCE

By

İDİL UYAN

August, 2017

INVESTIGATION OF SPONTANEOUS DIFFERENTIATION OF NEURAL STEM CELLS ON SYNTHETIC SCAFFOLDS

By İdil Uyan,

August, 2017

We certify that we have read this thesis and that in our opinion it is fully adequate, in scope and in quality, as a thesis for the degree of Master of Science.

Ayşe Begüm Tekinay (Advisor)

Michelle Marie Adams

Memed Duman

Approved for the Graduate School of Engineering and Science:

Ezhan Karaşan

Director of the Graduate School of Engineering and Science

ABSTRACT

INVESTIGATION OF SPONTANEOUS DIFFERENTIATION OF NEUROSPHERES ON SYNTHETIC SCAFFOLDS

İdil Uyan

M.Sc. in Neuroscience

Advisor: Ayşe Begüm Tekinay, PhD

August, 2017

Despite the increasing incidents of brain injuries and neurodegenerative diseases, a definitive clinical therapy for these conditions has not been found yet. Nervous system injuries result in loss of neural cells, causing loss of function in the neural circuitry. As mature neurons do not divide, it is not possible to tolerate the loss of neurons by the production of new ones. In the central nervous system, even though neural stem cells are present, their number and regenerative capacity are very low. In addition, inhibitory molecules are released at the degeneration site which hinders reconnection of the remaining cells. As the damage is due to the loss of neurons, cell therapy is considered as a promising option. Neural stem cells are capable of differentiating into the three major cell types in the central nervous system: neurons, astrocytes, and oligodendrocytes. However, due to low rate of survival of the transplanted cells, there is still a need for a cell vehicle system to promote their survival, adhesion, migration, and differentiation. On the other hand, use of biological molecules such as growth factors or extracellular matrix proteins as vehicle systems should be minimized due to the immunological risks. Nanotechnological approaches serve as a great opportunity to mimic the native

environment of the cells. Peptide amphiphiles (PAs) are self-assembling molecules that provide precise control over their secondary structure and the amino acid sequence, which can mimic proteins and show hydrogel properties. In this thesis, self-assembling PA scaffolds that mimic laminin, heparan sulfate and cadherin, which are key players in nervous system regeneration, have been investigated as cell delivery vehicles. Neurospheres are great models for studying the behavior of neural stem cells within a heterogeneous 3-dimensional cell population. Migration and differentiation behavior of neurospheres were investigated on laminin (LN), heparan sulfate (GAG), and cadherin-mimetic (HAV) PA nanofiber scaffolds. The results indicated that LN and GAG mimicking PA scaffolds cooperatively enhanced the migration of neurospheres, whereas cadherin mimetic PA scaffolds were individually sufficient to promote their migration. Also, a fine neural network was observed to be established on HAV-PA. These scaffolds hold high potential to be used as cell delivery vehicles.

KEYWORDS: neural regeneration, neurospheres, peptide amphiphiles, laminin, heparin sulfate, cadherin, migration

ÖZET

NÖRAL KÖK HÜCRELERİN SENTETİK PLATFORMLAR ÜZERİNDEKİ SPONTANE FARKLILAŞMALARININ İNCELENMESİ

İdil Uyan

Nörobilim, Yüksek Lisans

Tez Danışmanı: Ayşe Begüm Tekinay

Ağustos, 2017

Artan beyin yaralanmaları vakaları ve nörodejeneratif hastalıklara rağmen fonksiyonel yenileşmeyi sağlayan kesin bir klinik terapi henüz bulunmamaktadır. Sinir sistemi yaralanmaları sinir hücrelerinin kaybına, dolayısıyla sinirsel devrede işlev kaybına neden olur. Olgun nöronlar bölünmediğinden, nöron kaybına, yeni nöronların üretilmesiyle tolere edilememektedir. Santral sinir sisteminde, sinir kök hücreleri mevcut olmasına rağmen, sayıları ve yenilenme kapasitesi çok düşüktür. Buna ek olarak, dejenerasyon bölgesinde, geri kalan hücrelerin yeniden ağ kurmasını engelleyen inhibe edici moleküller salgılanmaktadır. Fonksiyonel hasar, nöronların kaybından kaynaklandığından, hücre tedavisi umut verici bir seçenek olarak düşünülür. Sinir kök hücreleri merkezi sinir sistemindeki üç ana hücre türüne farklılaşabilme yeteneğine sahiptir; nöronlar, astrositler ve oligodendrositler. Bununla birlikte, transplante edilen hücrelerin düşük sağkalımından ötürü, hayatta kalma, adezyon, migrasyon ve farklılaşmayı teşvik etmek için hâlâ bir hücre taşıma sistemine ihtiyaç duyulmaktadır. Bu durumda, immünolojik riskler nedeniyle

büyüme faktörleri veya hücre dışı matris proteinleri gibi biyolojik moleküllerin kullanılması en aza indirgenmelidir. Nanoteknolojik yaklaşımlar, hücrelerin doğal ortamını taklit etmek için oldukça uygundur. Peptit amfifil molekülleri (PA'lar), proteinleri taklit edebilen ve hidrojel özelliklerini gösterebilen, sekonder yapıları ve amino asit dizisi üzerinde kesin kontrol sağlayan kendinden bir araya gelebilen molekülleridir. Bu tezde, sinir sistemi yenilenmesinde önemli rol oynayan laminin, heparan sülfat ve kaderin proteinlerini taklit eden kendiliğinden bir araya gelen PA iskeleleri hücre taşıma araçları olarak araştırılmıştır. Nöroküreler, heterojen bir 3 boyutlu hücre popülasyonu içindeki sinir kök hücrelerinin davranışını incelemek için mükemmel modellerdir. Nörokürelerin migrasyon ve farklılaşma davranışları, laminin (LN), heparan sülfat (GAG) ve kaderin benzeri (HAV) PA nanofiber iskeleler üzerinde araştırılmıştır. Sonuçlar, PA iskeletlerini taklit eden LN ve GAG'ın kooperatif etkisi ile nörokürelerde migrasyonun arttığı, buna karşın kaderin benzeri PA iskeletlerinin ise migrasyonu kendi başına desteklemek için tek yeterli olduğunu görülmüştür. Ayrıca, HAV-PA'da iyi bir sinir ağı kurulduğu gözlenmiştir. Bu iskeleler, hücre dağıtım araçları olarak kullanılma potansiyeline sahiptir.

ANAHTAR SÖZCÜKLER: nöral yenilenme, nöroküre, peptit amfifil, laminin, heparan sülfat, kaderin, migrasyon

ACKNOWLEDGEMENTS

First and foremost, I would like to express my sincere gratitudes to my advisor Prof. Ayşe Begüm Tekinay for giving me the opportunity to be a member of this huge research group. I am grateful to her for her guidance, especially for teaching me the how to conduct research from the beginning till the end, how to multitask, and how to cope with lab crises. This master's has been a lifetime of experience. I also would like to thank Prof. Mustafa Özgür Güler and Prof. Aykutlu Dana for their valuable guidance and support during my master's education.

I would like to acknowledge the graduate scholarship from BİDEB 2210-C TÜBİTAK (The Scientific and Research Council of Turkey) for supporting me financially.

From my colleagues, I firstly would like to express my thanks to Dr. Özlem Erol, for being a perfect supervisor, for her mental and technical guidance, for always helping me with my experiments and more importantly for her great friendship.

I would like to thank the former Ph.D. students of the neuroscience subgroup; Dr. Melike Sever and Dr. Büşra Mammadov for teaching me how to perform experiments, guiding me throughout my studies and always answering me with a smiling face.

I would like to thank my İYTE family, my lifetime friends; Merve Şen, Nurcan Haştar, Zeynep Okur, Gökhan Günay and Fatih Yergöz for always being there for me as my sisters and my brothers and for their extremely fun friendship and cheerful breakfasts, lunches and dinners. We've always supported each other in ups and downs. My last 2.5 years have been much easier with them.

I have also gained great friends in Ankara. I would like to thank the UNAM 5th floor team; Canelif Yılmaz, Özge Uysal, Nuray Gündüz, Mustafa Beter, Ahmet Emin Topal, Begüm Dikeçoğlu, Nuray Gündüz, Zehra Yıldırım, Aslı Ekin Doğan, Dr. Elif Arslan, Hatice Kübra Kara, Gülistan Tansık, Alper Devrim Özkan, Aref Khalily, Melis Ekiz Şardan, Şehmus Tohumeken, Yasin Tümtaş, Seher Yaylacı, Göksemin Fatma Şengül, Recep Erdem Ahan, İbrahim Çelik, Mustafa Fadlemula, Faruk Okur, Muhammad Fathi Tovini, Özlem Tufanlı, Buket Gültekin, Dr. Begüm Kocatürk, Dr. Hamid Muhammed Seyid for bring great friends and colleagues to me.

I would like to thank my dearest friends from my university; Gözde Serim, Fırat Aşır, Tuğcan Korak, Cansu Küçükköse, Duygu Koca, Mehtap Çoban, Edanur Ates, Sevgi Önal, Esin Işık, Müge Molbay, Pelin Kaya Hicret Aslı Yalçın, Nur Cengiz, Miray Fidan and Kamer Burak İşçi.

I would like to thank my family members Mehtap Dutar, Mustafa Uyan, Gülten Dutar, Şahra Uyan, Serap Artun, Mehmetcan Artun, Güldemet Artun, Alidost Artun, Kerimcan Artun as well as my new family members Gülsüm Arıöz, Bülent Arıöz and Berk Arıöz, for always believing and supporting in me.

Finally I would like to thank my husband, my life partner, my best friend Burak Arıöz for everything he has given me.

This thesis is dedicated to the people who always believed in me.

Contents

Abbreviations	xvii
Chapter 1	1
1.1. Nanomaterials for Biomedical Applications	1
1.2. Regenerative medicine	3
1.3. Self-Assembly	4
1.4. Peptide Amphiphiles (PAs) as Self-Assembling Monomers	6
1.5. Self-Assembling PAs in Regeneration of the Nervous Tissue.....	9
1.5.1. Nerve Regeneration and the Roles of ECM	9
1.5.2. Peripheral Nervous System	10
1.5.3. Central Nervous System	12
1.5.4. Challenges in Engineering Biomaterials For Nervous System Repair	13
Chapter 2	16
2. Objectives	16
2.1. Introduction	16
2.2. Experimental Section	20
2.2.1. Materials	21
2.1.2. Synthesis of PA molecules	21
2.1.3. Characterization of PA Molecules.....	22
2.1.3.1. Purification of PA Molecules by Prep-HPLC	22
2.1.3.2. Liquid Chromatography-Mass Spectrometry (LC-MS) Analysis	23
2.1.4. Secondary Structure Analysis with CD	23
2.1.5. Atomic Force Microscopy (AFM).....	23

2.1.6.	Generation of Neurospheres from Mouse E13.5 Embryos.....	23
2.1.7.	Preparation of Peptide Coatings for Cell Culture	25
2.1.8.	Cellular Viability Analysis	26
2.1.9.	Spontaneous Differentiation of Neurospheres.....	26
2.1.10.	Migration of Neurospheres	26
2.1.11.	Immunocytochemical Stainings of Neurospheres	26
2.2.	Results and Discussion	27
2.2.1.	Design, Synthesis and Characterization of PAs	27
2.2.2.	Characterization, Viability and Migration Capacity of Neurospheres on PA nanofibers.....	33
2.2.3.	Immunocytochemical Stainings of Migrated Neurospheres on PA Nanofibers.....	38
2.2.4.	Conclusion	41
Chapter 3	43
3.1	Objectives	43
3.2.1.	Introduction.....	44
3.2.2.	Limitations of Conductive Polymers	45
3.3.	Experimental Section	48
3.3.1.	Materials	48
3.3.2.	Synthesis of Tetra(Aniline)	48
3.3.3.	Synthesis of Peptide Amphiphile Molecules.....	48
3.3.4.	Characterization of PA molecules by LC-MS	49
3.3.5.	Purification of PA Molecules	50
3.3.6.	FTIR Spectroscopy	50

3.3.7.	Transmission Electron Microscopy	50
3.3.8.	Scanning Electron Microscopy.....	50
3.3.9.	Secondary Structure Analysis.....	51
3.3.10.	Rheological Measurements.....	51
3.3.11.	UV-vis-NIR Spectroscopy.....	52
3.3.12.	Conductivity Measurements	52
3.3.13.	Peptide Coating and Cell Culture	52
3.3.14.	Biocompatibility of PC-12 Cells	53
3.3.15.	Quantification of Neurite Lengths	54
3.3.16.	Immunocytochemical Stainings.....	54
3.3.17.	Western Blotting.....	55
3.3.18.	Statistical Analysis.....	55
3.4.	Results and Discussion.....	55
3.4.1.	Design and Characterization of Peptide Amphiphile Nanofibers.	56
3.4.2.	Conclusion and Future Perspectives	75
	Bibliography	76

LIST OF FIGURES

Figure 1 The distribution of different materials within the nanoscale.....	1
Figure 2 Top down and bottom up approaches of nanomaterial synthesis. Reprinted from ref [2] with permission.	3
Figure 3 Self assembling monomers forming various secondary structures [1]. Reprinted with permission from Nature Publishing Group.	5
Figure 4 (A) The chemical structure of self-assembling peptide amphiphiles, (B) the 3D model of self-assembled nanofibers, their (C) SEM and (D) TEM images [23]. Reprinted with permission from Soft Matter.	9
Figure 5 Directing the NSC fate by ECM molecules and other exogenous factors <i>in vivo</i> and <i>in vitro</i> [3]. Reprinted with permission from Elsevier.....	18
Figure 6 (a) The location of HAV peptide on the EC1 domain on the extracellular portion of the N-cadherin protein structure. (b) HAV motif is conserved in mouse, rat, human and chick [93]. Reprinted with permission from. Elsevier.	20
Figure 8 Chemical structures of PA molecules used in this study.....	28
Figure 9 The LC-MS of the positively charged PAs; (a) LN-PA; $[M+H]^+$ (calculated): 1292.93, $[M+H]^+$ (observed): 1292.95, $[M+2H]^{+2/2}$ (calculated): 646.96, $[M+2H]^{+2/2}$ (observed): 646.98, (b) HAV-PA; $[M+H]^+$ (calculated): 1149.4, $[M+H]^+$ (observed): 1149.78, $[M+2H]^{+2/2}$ (calculated): 574.7, $[M+2H]^{+2/2}$ (observed): 573.89, (c) KK; $[M+H]^+$ (calculated) = 782.58, $[M+H]^+$ (observed) = 782.59.	29
Figure 10 The LC-MS of the negatively charged PAs. (a) GAG-PA; $[M-H]^-$ (calculated): 1225.59, $[M-H]^-$ (observed):1224.61, $[M- 2H]^{-2/2}$ (calculated): 612.29,	

[M-2H] ⁻² /2 (observed): 611.81, (b) EE; [M-H] ⁻ (calculated) = 782.47, [M-H] ⁻ (observed) = 782.49.	30
Figure 11 CD spectra of the individual PA solutions.	31
Figure 12 CD spectra of the PA mixtures.	32
Figure 13 Height map of peptide nanofibers imaged by AFM. (a) LN/GAG, (b) LN/EE, (c) KK/GAG, (d) HAV/EE, (e) KK/EE.	32
Figure 14 Characterization of neurospheres by (a) sox-2, (b) nestin, (c) βIII tubulin and S-100 markers.	34
Figure 15 Viability of dissociated neurospheres on (a) LN/GAG, (b) LN/EE, (c) KK/GAG, (d) HAV/EE, (e) KK/EE and (f) PLL coated surfaces. (g) Percentage viability of cells on the PA nanofiber and PLL coated groups. Values represent mean ± SEM, **p<0.01.	35
Figure 16 Migration of neurosphere derived cells 2 days after seeding under spontaneous differentiation conditions on (a) LN/GAG, (b) LN/EE, (c) KK/GAG, (d) HAV/EE, (e) KK/EE PA nanofibers.	36
Figure 17 Migration of neurosphere derived cells 4 days after seeding under spontaneous differentiation conditions.	37
Figure 18 Sox-2 stained neurospheres on LN/GAG, LN/EE, KK/GAG, HAV/EE and KK/EE PA nanofibers. Scale bars are 50 μm.	39
Figure 19 βIII tubulin stained neurospheres on LN/GAG, LN/EE, KK/GAG, HAV/EE and KK/EE PA nanofibers. Scale bars are 50 μm.	40
Figure 20 Mass spectrum of TA-EB in acetonitrile, [M+H] ⁺ (calculated) = 365.17, [M+H] ⁺ (observed) = 365.18.	56
Figure 21 Chemical structures of peptide amphiphiles.	57

Figure 22 LC-MS spectrum of (a) E₂, [M-H]⁻ (calculated) = 782.47, [M-H]⁻ (observed) = 782.51, [M-2H]²⁻ (calculated) = 390.74, [M-2H]²⁻ (observed) = 390.75, (b) K₂, [M+H]⁺ (calculated) = 782.58, [M+H]⁺ (observed) = 782.59, [M+2H]²⁺ (calculated) = 391.79, [M+2H]²⁺ (observed) = 391.78, (c) E₂-TA, [M-H]⁻ (calculated) = 1046.48, [M-H]⁻ (observed) = 1046.50, [M-2H]²⁻ (calculated) = 522.74, [M-2H]²⁻ (observed) = 522.75, and (d) K₂-TA, [M+H]⁺ (calculated) = 1046.59, [M+H]⁺ (observed) = 1046.60, [M+2H]²⁺ (calculated) = 523.80, [M+2H]²⁺ (observed) = 524.31, [M+3H]³⁺ (calculated) = 349.53, [M+3H]³⁺ (observed) = 349.54. 57

Figure 23 FTIR analysis of PAs..... 59

Figure 24 SEM and TEM analysis of PA mixtures..... 60

Figure 25 CD spectra results of individual PAs and their mixed forms. 61

Figure 26 UV-vis-NIR absorption spectroscopy of PA molecules and their mixed forms. 62

Figure 27 Current/voltage (*I/V*) curves of E₂/K₂ and E₂-TA/K₂-TA. 64

Figure 28 Representative AFM images and height profiles of (a) E₂/K₂ (b) E₂-TA/K₂-TA (c) TA-dedoped, (d) TA-doped samples casted on glass substrate (a scratch has been made in the film closed to the contact gold electrode to determine film thickness)..... 66

Figure 29 Gel formation and rheological analyses of PA hydrogels. The photo of the solution of non-electroactive and electroactive PAs and self-supporting gel behaviors upon their corresponding mixture (a). Elastic and viscous modulus of E₂/K₂ and E₂-TA/K₂-TA gels (b). Time sweep test at constant angular frequency ($\omega = 10$ rad/s) (c). Strain (d) and frequency sweep tests of E₂/K₂, E₂-TA/K₂-TA gels (e)..... 67

In biomedical applications, the biocompatibility of a biomaterial is crucial. Ideally, the biomaterial should support adhesion and survival of the cells. To evaluate the biocompatibility and further investigate the bioactivity of E₂-TA/K₂-TA gels, PC-12 cells, derived from rat pheochromocytoma were used as a model cell line for

Figure 30 Biocompatibility of PC-12 cells on (a) E₂-TA/K₂-TA and (b) E₂/K₂ gels and (c) PLL coated surfaces. (d) AlamarBlue® viability analysis of PC-12 cells on E₂-TA/K₂-TA and E₂/K₂ gels and PLL coated surfaces. 69

Figure 31 The effect of E₂-TA/K₂-TA gels on neural differentiation, the neurite processes of PC-12 cells. Bright field images of neurite outgrowth of PC-12 cells on E₂-TA/K₂-TA, E₂/K₂ gel and PLL coated surfaces (a-c), scale bars=100 μm. Percentage relative frequency distribution of neurite lengths (d). Average neurite length and percentage of neurite bearing PC-12 cells on E₂-TA/K₂-TA and E₂/K₂ gels and PLL coated surfaces (e-f). 70

Figure 32 Confocal images of βIII tubulin stained PC-12 cells grown on E₂-TA/K₂-TA, E₂/K₂ gel and PLL coated surfaces (a-c). Scale bars=20 μm. 72

Figure 33 Bright-field images of PC-12 cells on E₂-TA/K₂-TA, E₂/K₂ gels and PLL coated surfaces on day 6 without NGF induction (a-c). 73

Figure 34 Protein expression levels of ERK1/2 phosphorylation of PC-12 cells cultured on E₂-TA/K₂-TA and E₂/K₂ gels and PLL coated surfaces. Data presented as mean±SEM (n=3), *p<0.05. 74

LIST OF TABLES

Table 1 Histogram data of relative percentage frequency distribution of neurite length values on E ₂ -TA/K ₂ -TA and E ₂ /K ₂ gels and PLL.....	72
--	----

Abbreviations

ANOVA	Analysis of variance
CD	Circular dichroism
DCM	Dichloromethane
DIEA	<i>N,N</i> -diisopropylethylamine
DMEM	Dulbecco's modified Eagle's medium
DMF	<i>N,N</i> -Dimethylformamide
ECM	Extracellular matrix
FBS	Fetal bovine serum
Fmoc	9-Fluorenylmethoxycarbonyl
GAPDH	Glyceraldehyde 3-phosphate dehydrogenase
HBTU	<i>N,N,N',N'</i> -Tetramethyl- <i>O</i> -(1 <i>H</i> -benzotriazole-1-yl)uronium hexafluorophosphate
HPLC	High pressure liquid chromatography
LC-MS	Liquid chromatography-mass spectroscopy
PA	Peptide amphiphile
PBS	Phosphate buffered saline
SEM	Scanning electron microscopy
TA	Tetra(aniline)
TCP	Tissue culture plate
TEM	Transmission electron microscopy
TFA	Trifluoroacetic acid
TIS	Triisopropyl silane
UV	Ultraviolet

Chapter 1

1. Introduction

1.1. Nanomaterials for Biomedical Applications

Design and advancement of nanotechnology-based diagnostics, drug discovery and delivery systems have led to many breakthroughs over the last decade thanks to the scientific contributions from multiple disciplines such as physics, chemistry, engineering, materials science, medicine, biology and many others [4]. Nanotechnology can be used to develop functional systems for diverse applications. The starting points of these breakthroughs are the development of novel nanomaterials and control over their size, shape, structure, functionality, processability and stability, eventually leading to the creation of building blocks to

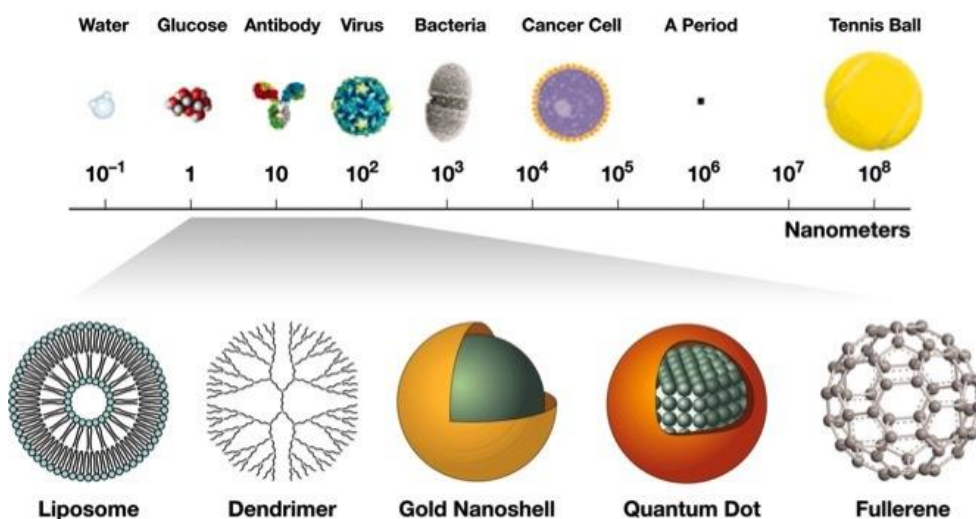


Figure 1 The distribution of different materials within the nanoscale.

monitor molecular events as well as advancement of therapies for diseases or disorders. As a definition, nanomaterials are structural units, particles, fibers or

components with other shapes that have a size smaller than 100 nm in at least one dimension (Figure 1) [5]. Studying at the nano-scale enables higher sensitivity, selectivity and throughput. Nanomaterials can consist of polymers, composites, organic materials, metals, ceramics, etc. and can have many shapes such as nanofibers, nanoparticles, nanocrystals, nanotubes, nanorods, nanowires, etc. Two approaches can be applied for the synthesis of nanomaterials; bottom-up and top-down (Figure 2). Top-down approaches use macroscopic materials as initial structures and include further processing of these materials to form nanostructures. Currently, lithography techniques are the most commonly used top down approaches. Top-down methods are usually expensive, time consuming, and not suitable for large scale production, since high technology complex devices are required for the synthesis process. Whereas bottom-up approaches include assembly of the starting material, which can be atoms or molecules, to form nano-scale materials. Bottom up approaches relies on the chemical properties of the single molecules or atoms to self-assemble or self-organize into more complex nanostructures and uses intermolecular forces.

Another importance of working with nanomaterials is because of the fact that the material properties undergo a drastic change when the material size decreases to the nanoscale. Surface area, surface roughness and surface to volume ratio properties vary between the bulk and nanoscale versions of the same material which gives nanomaterials superior physiochemical properties. By having control over these properties, optical, electrical, mechanical and magnetic properties can be further customized [6]. Therefore, materials with such excellent properties are preferred

and investigated in biomedical applications due to the limitations of conventional therapies and can overcome the inadequacies of existing treatment strategies [7].

1.2. Regenerative medicine

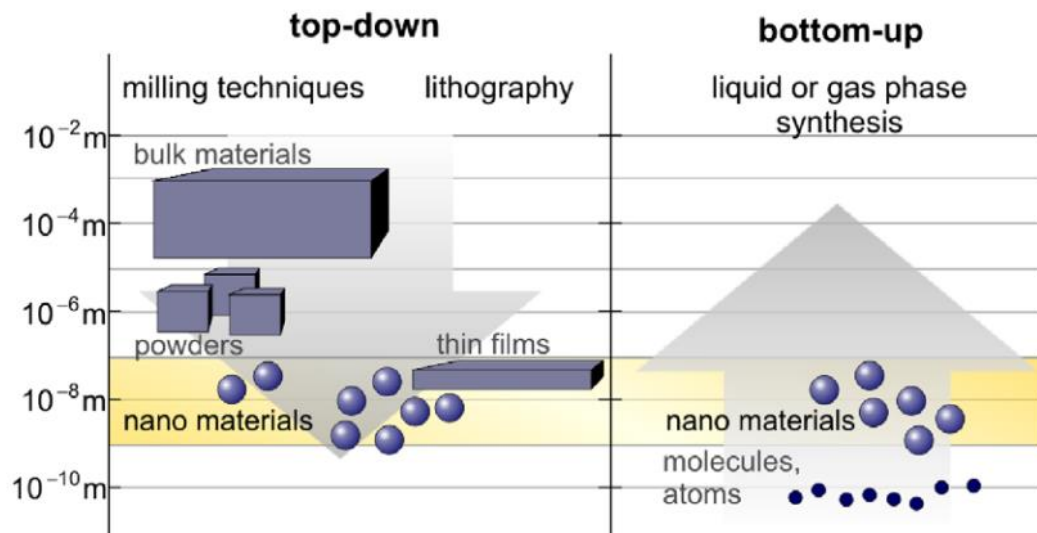


Figure 2 Top down and bottom up approaches of nanomaterial synthesis. Reprinted from ref [2] with permission.

Regeneration is the process in which the loss of tissue is compensated by reformation of the ECM, cell proliferation and in certain cases subsequent differentiation. Regenerative medicine is a field where several disciplines from engineering and life sciences meet to develop functional therapies against diseases, disorders or injuries. These therapies aim to restore, maintain or improve the problematic tissue [8], and can have a variety of applications including transplantation of cells, application of biomaterials, small molecules, growth factors, implants or delivery of drugs. As mentioned previously, nanotechnological approaches come in handy with respect to designing therapies [7].

The structure and organization of the native tissue are of great interest while designing therapies for the damaged or diseased tissue. Therefore, we need to have a better understanding of the nanoscale properties of the native tissue in order to improve our approaches. The cells in the damaged or diseased tissue display behavioral changes depending on the interactions with its close proximity. Thus, the applied biomaterial should resemble the biological, physiological, topographical and physiochemical properties to the native tissue, show biocompatibility with the host tissue and should not cause aberrant bioactivity [9]. Within this context, the usage of nanotechnology in mimicking the signals in cell-cell, cell-ECM or cell-soluble factor interactions to promote cell proliferation, differentiation, migration and ECM restorage have been some of the promising approaches [10].

1.3. Self-Assembly

Self-assembly is a natural process, in which individual atoms or molecules organize themselves into supramolecular structures, forming ordered secondary structures. This process usually occurs through hydrogen bonds, electrostatic interactions, an organization of hydrophilic and hydrophobic segments of the molecules, repulsive forces and many other complex interactions [11, 12]. Supramolecular systems are dynamic systems which are in concert with the dynamic environment of the living tissue and are originally inspired by nature. For instance, lipid bilayer of the cell membrane is a very sturdy layer that surrounds the cell, protecting the intracellular components as well as serving as a selective barrier and a cell signaling platform between the extracellular space and intracellular environment. The basis of the membrane formation is self-assembly of phospholipid monomers, which occurs naturally [13]. As another example, ECM, which provides support to the cells, is

composed of fibrous-like elements such as fibronectin and collagen, which are

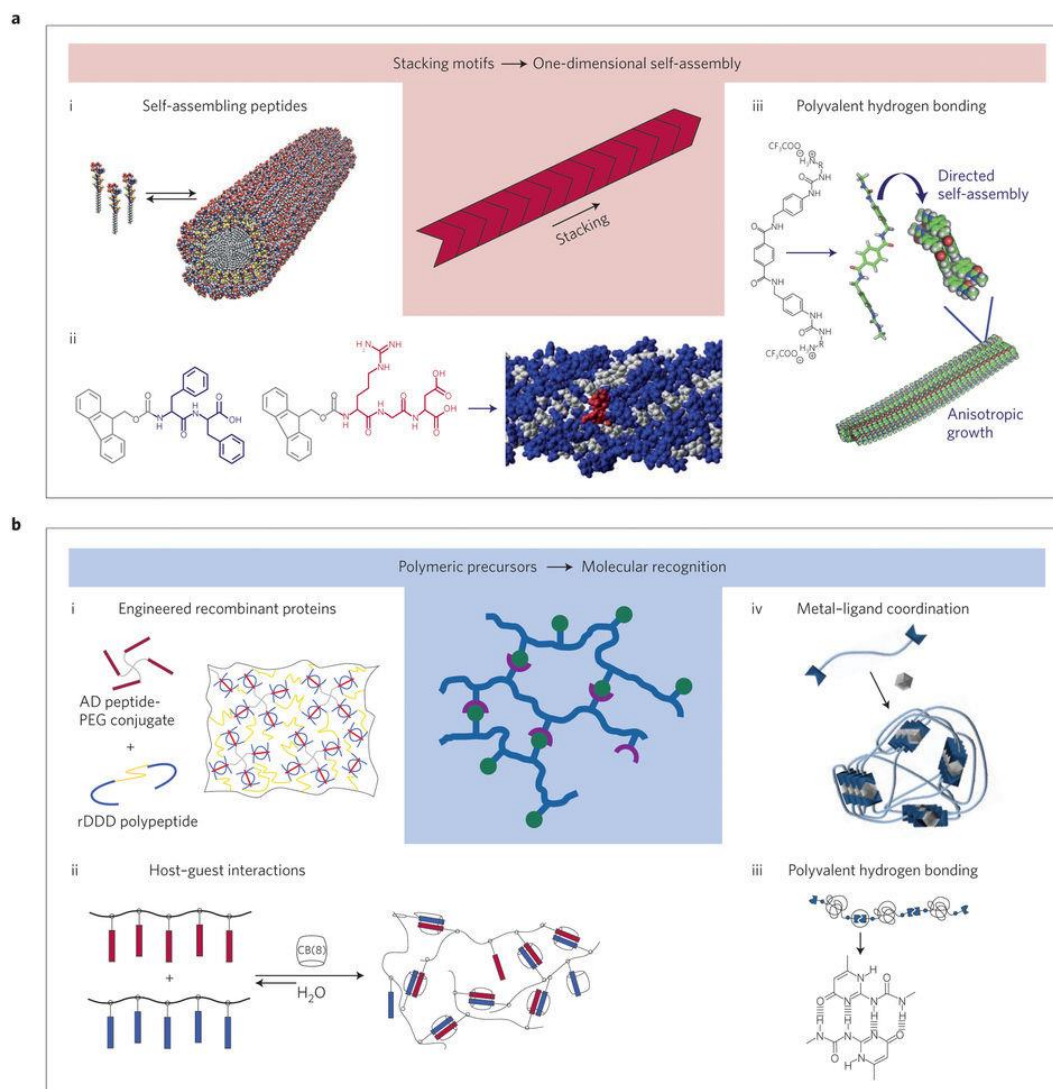


Figure 3 Self assembling monomers forming various secondary structures [1]. Reprinted with permission from Nature Publishing Group.

generally formed by self-assembly, [14], whereas inside the cells, microfilaments and microtubules are examples of self assembled components which have fundamental roles in cell motility and division [12, 15].

The use of self-assembling monomers to form hierarchical structures is a promising strategy to form functional biomaterials that resemble the native ECM. Biomimicking ECM elements, especially the ones that have roles in regeneration or developmental processes can be of great interest, these materials allow interaction at the nanoscale and molecular control over the biochemical signaling reactions required for the regeneration process. Ideally, biologically derived materials such as saccharides, amino acids, nucleotides and lipids should be incorporated into the nanomaterials to ensure biocompatibility and biodegradability after the applied material fulfills its function.

1.4. Peptide Amphiphiles (PAs) as Self-Assembling Monomers

Within the concept of designing promising platforms by using self-assembling biomaterials, PAs serve unique features. These molecules, with a hydrophobic and a hydrophilic part within the same molecule, provide precise control over the amino acid sequence, the structure of the hydrophobic part and the secondary structures. Peptides have been known as biological compounds or artificially synthesized materials that have great roles in various cellular processes. Since they are made up of amino acids, they are likely to have a biocompatible and biodegradable nature [16]. They have been investigated in biology and materials science in particular, to be used both in soluble form, immobilized on scaffolds or as self-assembling scaffolds. Due to their inherent capacity to self-assemble, they may form 3D networks through intermolecular weak bonds [17]. The variability in the design of peptide sequence also provides the opportunity to use combinations of amino acid sequences that are known to give rise to certain types of secondary structures at the nanoscale. Large scale synthesis of long sequences of aminoacids forming

functional proteins still remains as a challenge, whereas oligomers of the amino acids can be preferred due to the ease of standard solid-phase synthesis. These oligomers can be used for the purpose of producing functional protein mimicking structures. Although research on biomimicking short peptide chains is in its early stages, many ECM proteins can be biomimicked by peptides. Not only the peptide sequence itself, but also the specific folding of the peptide play a role on functional mimicry. With nanofiber forming PA design, the molecules self-assemble into ECM mesh like scaffolds which also play a critical role in the bioactivity of these molecules, mimicking also the structure of the ECM proteins, together with their function.

High purity large scale synthesis is possible by solid phase synthesis method [18]. In this method, the amino acids are conjugated on a solid support starting from the C-terminus of the first binding amino acid. The subsequent amino acid addition is performed by linkage of the C-terminus of the new-coming amino acid to the N-terminus of the existing amino acid [19].

For this thesis, PAs are designed with a lauric acid hydrophobic tail group and a β -sheet forming sequence “VVAG”. Upon mixing oppositely charged molecules under physiological conditions, these molecules self-assemble through hydrophobic-hydrophilic self-organization, eventually forming micelles. These micelles align themselves into form nanofibers [20, 21]. The hydrophilic part of the PA molecules have the capacity to bear bioactive signals, and, when self-assembly process occurs, these bioactive sequences are displayed on the outer surface of the nanofibers providing a high epitope density (Figure 4). Other charged groups may

also be incorporated into the structure to change the overall charge of the molecule. In addition to forming nanofibers upon mixing oppositely charged molecules, they form nanofibrous networks that have hydrogel properties, which is a very important property for soft tissue engineering. The resemblance of the mechanical properties of the biomaterial to have the target tissue is of vital importance in terms of allowing integration of the host or transplanted cells into the biomaterial, especially in soft tissues such as the nervous or cartilage tissue. The main reason for that is that, the residing cells display complex behaviors when a biomechanically different material is introduced into the tissue, which might change its physiological function [22]. Therefore, the ultimate goal in regenerative therapies is to supply multiple cues that will mimic the biological, physiological, mechanical and topographical properties of the surrounding of the cell. The ability of PAs to be tailored into various functional biomimetic nanomaterials gives them the opportunity to be used in various tissue engineering studies.



Figure 4 (A) The chemical structure of self-assembling peptide amphiphiles, (B) the 3D model of self-assembled nanofibers, their (C) SEM and (D) TEM images [23]. Reprinted with permission from Soft Matter.

Section 1.5 is partially described in the following book chapter;

M. Sever, I. Uyan, A.B. Tekinay & M.O. Guler, “Bioactive Nanomaterials for Neural Engineering. In Neural Engineering,” *Springer International Publishing*, pp. 181-206, 2016.

1.5. Self-Assembling PAs in Regeneration of the Nervous Tissue

1.5.1. Nerve Regeneration and the Roles of ECM

The nervous system is a highly complex interconnected network and higher organisms including humans have limited neural regeneration capacity. Because of this limitation, neurodegenerative diseases result in significant cognitive, sensory or motor impairments. Following an injury in the neural network, there is a balance between promotion and inhibition of regeneration and this balance is shifted towards different directions in central nervous system (CNS) and peripheral nervous system (PNS). More regeneration capacity is observed in the PNS compared to the CNS. Although several mechanisms play roles in the inhibitory and growth-promoting features of the CNS and PNS, ECM molecules are key players in this process.

ECM is the architecture where the cells migrate, proliferate and differentiate [24, 25]. After a comprehensive investigation of the interactions between the ECM proteins and cell receptors, the ECM environment was found to regulate significant cellular processes, such as survival, proliferation, differentiation, and migration [26,

27]. Its components have major roles not only throughout neurogenesis during development of the nervous system but also for normal neural functioning during adulthood [28].1

1.5.2. Peripheral Nervous System

In the PNS, neurons and Schwann cells are the major cellular elements. Endoneurium tissue is the connective tissue that surrounds individual axon-Schwann cell units, whereas perineurium covers a fascicle of axons. Perineurium also acts as a barrier against fluxes of ionic and macromolecular compounds between connective and vascular tissues and endoneurium [29]. Epineurium is the outermost connective tissue, which covers the entire nerve [30]. In the endoneurium, Schwann cells are abundant whereas fibroblasts form 10% of the cell population [31]. Myelination after axonal regeneration has a central role for functional outcomes and proper ECM formation has a strong influence on this process [32].

Basal lamina of PNS consists of laminin, fibronectin, entactin, and heparan sulfate proteoglycans [32] and collagens [33]. Laminin is synthesized by the Schwann cells, and it is considered to have the leading bioactivity in terms of growth, adhesion, and migration of these cells [34]. Laminin has also been shown to have a critical effect on myelination during peripheral nerve regeneration in culture systems [35]. As another basal lamina element, collagen is the major ECM protein and it is produced mostly by the fibroblasts and Schwann cells in fibrillary and nonfibrillar forms [36]. Fibrous types of collagens; collagen I, III and V are found in all three ensheathing layers of peripheral nerve tissue. Collagen type-I and III are

present in small diameters on the external face of Schwann cell basal lamina, whereas collagen type-V colocalizes with them in addition to enveloping myelinating Schwann cells in the basal lamina [37]. Schwann cells also produce a more glycosylated and non-fibrillar type of collagen, collagen IV, which is a principle component of the basal lamina. Collagen IV has a role in integrating laminin, perlecan, nidogen and other ECM proteins into a supramolecular structure [38] in the basal lamina surrounding Schwann cells, the perineurial cells and endoneurial capillaries [36]. Fibroblasts produce a fibrillary network of collagens and provide the framework required for Schwann cell ensheathing of regenerating axons [39]. Fibronectin is another important ECM protein that has a very defined and specific expression pattern to guide neuronal outgrowth [40]. Interaction of fibronectin with collagen, heparin, fibrin and integrins via its specific domains results in cellular responses as cell adhesion, Schwann cell motility and growth [41]. Chondroitin sulfate proteoglycans (CSPG) are also abundant in the Schwann cell ECM; however, they show inhibitory activity in contrast to other ECM elements in the PNS tissue [42].

Although complete recovery of PNS is not common, especially for large gaps, PNS injury environment is more permissive for regeneration compared to CNS. Non-neuronal cells respond to injury and start a key event called “Wallerian degeneration” [43]. This process initiates a series of events which together help clearance of inhibitory myelin debris and promotion of axon regrowth [44]. Axon degeneration starts several days after the injury, leaving the tissues denervated [45]. When calcium starts to influx from the ECM and internal Ca^{2+} stores to the injured axon [46], calpain is activated, which is a protease, which functions in cytoskeletal

degradation and axonal degeneration [47]. Schwann cells and fibroblasts secrete tropic factors and detached Schwann cells go through proliferation. The basal lamina remains and guides endoneurium towards the distal site [48]. Schwann cells form Bands of Büngner with the help of fibrin cables, where fibroblasts and blood vessels can also use as a guiding surface [49]. Fibrin is later on replaced by collagens produced by fibroblasts and laminin secreted by Schwann cells. Regeneration fails when the initial fibrin cable cannot be formed due to a large gap [50].

1.5.3. Central Nervous System

Following a damage to the CNS, a series of molecular and cellular events occur resulting in inhibition of regeneration. Glial scar tissue formation is triggered by the entrance of non-CNS elements to the CNS. Although it leads to inhibition of regeneration, one important beneficial role of glial scar is to preserve the damaged tissue, repair the blood brain barrier (BBB) and minimize cellular degeneration and inflammatory burden [51, 52]. First, macrophages migrate to the injury site from the blood due to BBB disruption. Then, oligodendrocyte precursors migrate to the injury site in massive numbers. Finally, astrocytes proliferate and migrate to the area to fill in the injury area and become reactive, which is a process called “reactive astrogliosis” [53]. Reactive astrocytes produce glial fibrillary acidic protein (GFAP) after CNS injury, which can also be used as a marker for glial scar formation. Although GFAP production is similar to collagen fibers, they are important in the regeneration process. ECM of CNS is composed of protein or proteoglycan based aggregates whereas native PNS ECM has a fibrous structure [54].

1.5.4.Challenges in Engineering Biomaterials For Nervous System Repair

Besides producing growth promoting factors, astrocytes also produce four different types of proteoglycans, which are made up of a core protein and sulfated glycosaminoglycan chains attached to the sides that are inhibitory to regeneration; heparan sulfate proteoglycan (HSPG), dermatan sulfate proteoglycan (DSPG), keratan sulfate proteoglycan (KSPG) and CSPG [55]. Hyaluronic acid is another carbohydrate, which is also present in the ECM of CNS. It interacts with proteoglycans to form a mesh-like structure in the perineuronal network [56]. During development, CSPG plays a role in inhibitory patterning of the neuronal pathway [57]. In healthy adult perineuronal networks, they are involved in stabilization of synaptic plasticity [58]. However, upregulated levels of CSPG are known to increase glial scar in the mature spinal cord and brain [59], and they inhibit neurite outgrowth extensively *in vitro* [60]. They are upregulated within 24 h following injury and they remain at the injury site for months [61, 62]. Mechanism of CSPGs inhibition is thought to be both nonspecific, through the contact of negatively charged glycosaminoglycan chains, and specific, through signaling mechanisms by interacting with PTP and receptors [60, 63].

Following a nervous system injury, regeneration capacity usually depends on the extent of the injury, the distance of the injury to the cell body and biological status of the patient (morbidity, age, etc.) [64]. The PNS and CNS respond to injury in their own unique way. In the PNS, Wallerian degeneration occurs in the distal end following a series of pathophysiological events. The distal portion of the nerve degenerates and the cellular debris is digested by the macrophages and monocytes [65]. Schwann cells form the Bands of Büngner in order to guide regenerating

axonal sprouts to their synaptic targets [66, 67]. During the extension process, bridging the gap between the two ends and optimizing the environment physically, chemically and biologically is a strategy that has been followed [67]. In PNS, the challenge is to find a perfect alternative to autologous nerve grafts; eliminating risks of secondary surgeries and precluding secondary damage on the body. Even though structural plasticity is achieved clinically, functional plasticity does not always reach complete state and it still is another principal consideration in PNS regeneration studies. Autologous nerve graft treatment shows 50% clinical functional recovery [68]. Furthermore, use of natural proteins for therapeutic purposes can cause immunogenic reactions. Sustained delivery or storage of growth factors are also required for effective usage of growth factors [67].

CNS has much smaller capacity to regenerate, thus CNS therapies are more challenging. Embryonic spinal cord and peripheral nerve grafts have been shown to support regeneration of CNS fibers; however, failed to successfully grow through the CNS – PNS transition zone [69, 70]. CNS does not have a permissive nature for regeneration. There are many reasons behind the obstructive environment of CNS injuries. Regeneration associated genes are expressed at low levels in the CNS [71]. Following the CNS injury, glial scar is formed and inhibitory molecules are released at the site of injury. Cellular debris and inhibitory myelin components are cleared much more slowly compared to the PNS as a result of low infiltration levels of macrophages through the brain-spinal cord barrier [72]. Moreover astrocytes proliferate at the site of injury, in a similar way to Schwann cell proliferation; however, in contrast, creating an inhibitory environment and becoming reactive astrocytes [73]. Thus, nerve regeneration studies focus on suppressing the

inhibitory nature of the nervous system injuries and future directions in PNS and CNS injuries include combining multiple cues at the same time to increase regeneration capacity [67]. BBB is another obstacle for drug delivery to the brain, considering that intracranial injections are much more invasive than other administration (intravenous, oral) methods. Another challenge for drug delivery is accurate targeting of the correct population of the cells.

Chapter 2

2. Objectives

Although there are neural stem cells in the brain that can potentially regenerate the cell loss, their number is limited and their intrinsic in vivo capacity to compensate the lost tissue following an injury is very low. The nervous tissue has low regeneration capacity and neural stem cell (NSC) transplantation has been considered as a promising approach. However, there is a need for an effective vehicle to support the adhesion, viability and migration of the transplanted cells. Laminin and heparan sulfate are two major ECM elements that have important roles both in the CNS and the PNS. Also, Cadherins are known to play key complex roles during development and patterning of the nervous system. Their regional specificity and differential expression patterns in the brain make them an adhesive code for the functioning of the nervous system [74]. The biocompatible, biodegradable, porous, hydrogel, nanofibrous and biomimicking potential of self assembling PAs makes them ideal candidates as cell delivery vehicles. In this work, the cooperative effect of laminin mimetic and heparan sulfate mimetic, as well as cadherin mimetic PAs were investigated for their migratory potential on embryonic mouse neurospheres in vitro. In addition, differentiation and neurite outgrowth potential of neurospheres were qualitatively assessed.

2.1. Introduction

The incidence of neurodegenerative diseases is increasing day by day, and no definitive treatment has yet been found for both for nervous system diseases and

damages. After a trauma, the unfavorable extracellular environment and the quite low regenerative capacity of nervous system cause detrimental outcomes and, unfortunately, current treatments cannot provide complete functional recovery. Hypothetically, NSCs have the potential to compensate for the loss of neurons and regenerate the traumatized region by differentiating into mature neurons, oligodendrocytes and astrocytes under appropriate conditions in theory, however, in the brain, they are found in low abundance and in a limited number of regions. In the adult mammalian brain, NSCs are restricted to dentate gyrus in the subgranular layer in hippocampus and the subventricular zone (SVZ) [75, 76]. Neurogenesis in the olfactory bulb occurs through the migration of SVZ NSCs to their final destination through the rostral migratory stream [77]. Throughout the life, limited neurogenesis occurs in some cortical regions, hippocampus and olfactory bulb [78]. Although these neural stem cells have the capacity to differentiate into neurons, oligodendrocytes and astrocytes, it is still a challenge to successfully differentiate them into a defined cell type, primarily into the neurons. Although some neurotrophic factors may play roles in this process, there are limitations in the traditional delivery methods because of the presence of BBB which does not allow diffusion of certain molecules. After all, exogeneous application of these factors as well as other biological molecules may lead to biocontamination, may cause immunological risks and have high cost. Moreover, the lesion becomes an unfavorable environment for NSC growth or axonal elongation due to the inhibitory components of glial scar [79, 80]. NSC transplantation studies have been promising approaches to treat brain injuries; however, there are still major problems to overcome. Cells are usually transplanted by injecting into a physiological liquid and

struggle to attach, completely survive or reach to the target site in the brain [81]. In this regard, the extracellular environment of the cells and the surrounding signals are of great importance to ensure cell survival, adhesion, migration and differentiation. Many types of growth factors, small molecules, ECM or other types of proteins have been utilized to differentiate NSCs *in vitro*. However intensive usage of biological molecules may lead to biocontamination, may cause immunological risks *in vivo* and have high costs. For this reason, minimizing the use of biological materials should be considered. Also, transplantation of cells in the liquid may cause the cells to sediment, resulting in failure of cell adhesion. At this point, usage of biomaterials to promote the efficiency of cell transplantation becomes a favorable option (Fig. 5). PAs can be designed to form nanofibrous mesh-like hydrogels that can provide a biocompatible, biodegradable and porous environment for the host as well as guest cells. The surface of the nanofibers can be

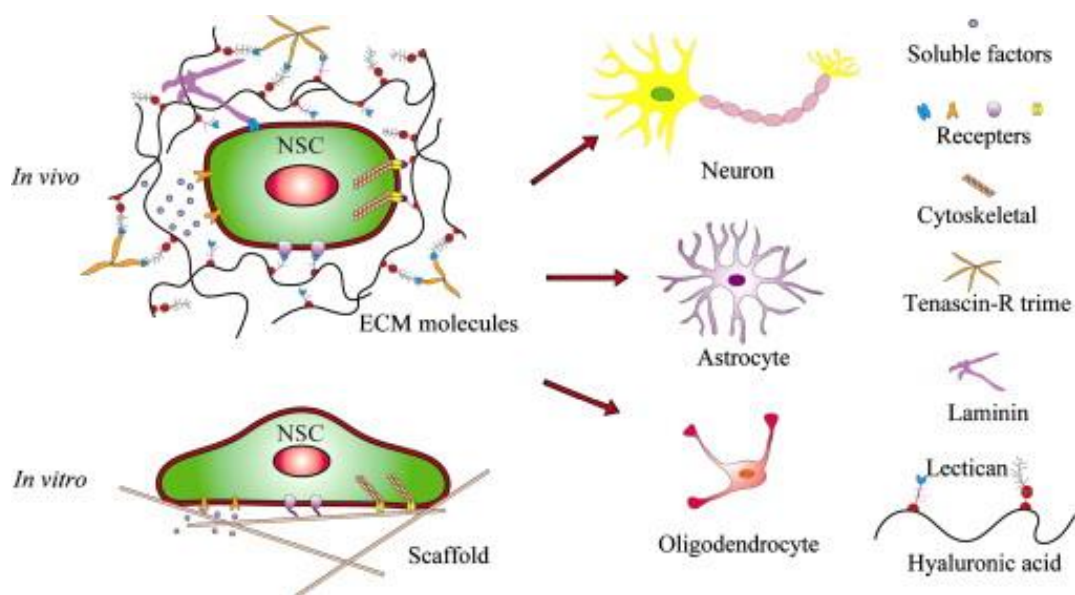


Figure 5 Directing the NSC fate by ECM molecules and other exogenous factors *in vivo* and *in vitro* [3]. Reprinted with permission from Elsevier.

decorated to mimic the function of proteins, especially the ECM proteins. Furthermore, their nanofibrous mesh-like structure mimics the topography of the ECM. In addition, the stiffness of the PA nanofiber hydrogels can be designed to match the target tissue stiffness. Ultimately, delivery of multiple signals helps cells to survive, adhere, migrate, proliferate and differentiate. Laminin is a heterotrimeric major ECM protein present both in the CNS and the PNS and is known to promote axonal outgrowth as well as myelination [82]. It not only plays a structural role but also has functions in signal transportation. For instance, laminins from the fractures of the basal lamina extend from the blood vessels to contact the stem cells in the niche [3]. Also, they are known to be involved in migration through the rostral migratory system [83, 84]. Heparan sulfates are also important elements of the ECM and are known to play significant roles in proliferation, differentiation and migration of NSCs [3]. Laminin, besides interacting with the cells through integrins, also interacts with other ECM molecules, such as heparan sulfates. The cooperative effect of laminin with heparan sulfate has been shown to promote neurite outgrowth *in vitro* [85, 86]. Furthermore, in our lab, laminin and heparan sulfate mimicking PA nanofibers were also shown to cooperatively promote neurite outgrowth and overcome the inhibitory effects of CSPGs.

Cadherins are important regulators of cell migration, and cellular differentiation and have been known to play critical and complex roles during development. N-cadherin binding is associated with enhanced adhesion and neurite outgrowth; however, activation of further downstream signaling events such as β -catenin pathway and adherens junction formation may cause hindered neurite outgrowth [87, 88]. Although some conflicting reports have been found in the literature, these

differential effects may be caused by the usage of different cell types. There are studies that showed the neurite outgrowth [89] and neuronal differentiation promoting [90] capacity of N-cadherins, however, they have also been shown to be insufficient in supporting the adhesion of cells alone [91]. HAV is a conserved peptide motif found in the extracellular region of classical cadherins (Figure 6) and its soluble treatment is known to inhibit cadherin mediated neurite outgrowth by binding to cadherins as antagonists [92, 93]. HAV motif, when given as a soluble mediator, might play neurite inhibiting properties, but we wanted to, however we would like to investigate the effect of HAV peptide displayed on nanofibrous scaffolds. By this way, the peptide sequence is immobilized on the scaffolds. In this study, we have used laminin, heparan sulfate and cadherin mimetic peptide nanofibers to promote migration and differentiation of embryonic mouse neurospheres *in vitro*.

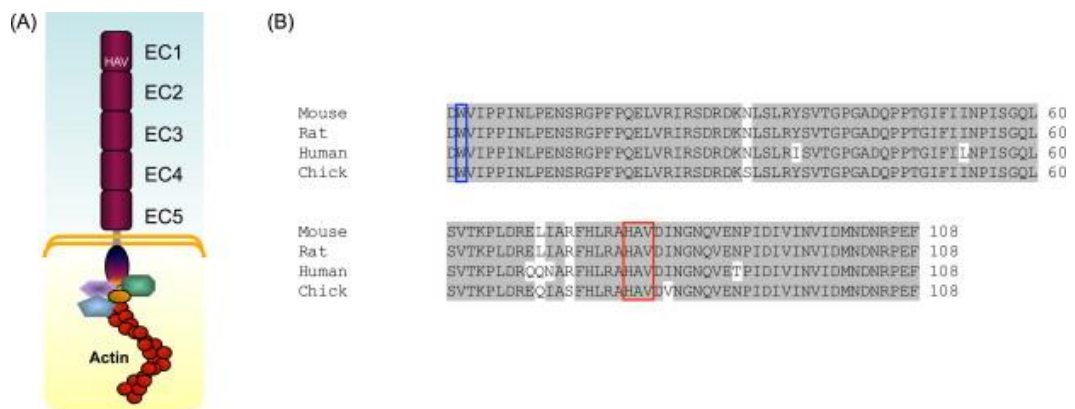


Figure 6 (a) The location of HAV peptide on the EC1 domain on the extracellular portion of the N-cadherin protein structure. (b) HAV motif is conserved in mouse, rat, human and chick [93]. Reprinted with permission from Elsevier.

2.2. Experimental Section

2.2.1. Materials

[4-[α -(2',4'-dimethoxyphenyl) Fmoc aminomethyl] phenoxy] acetamidonorleucyl-MBHA resin (Rink amide MBHA resin), 9-fluorenylmethoxycarbonyl (Fmoc) protected amino acids, and 2-(1H-benzotriazol-1-yl)-1,1,3,3-tetramethyluronium hexafluorophosphate (HBTU) were purchased from NovaBiochem. Fmoc-Ser[β -Glc(OAc)₄]-OH was purchased from AAPPTec. N,N-diisopropylethylamine (DIEA) and lauric acid were purchased from Merck. Other chemicals were purchased from Alfa Aesar or Sigma-Aldrich and considered as pure and were not further purified.

2.1.2. Synthesis of PA molecules

PA molecules were synthesized by Fmoc-protected solid phase peptide synthesis method. Rink amide was used as the solid support. LN-PA (Lauryl-VVAGKKIKVAV-Am), GAG-PA [Lauryl-VVAGEGDK(psulfobenzoate)-Am], and HAV-PA (Lauryl-VVAGKKHAV-Am) were used as the bioactive PA molecules whereas KK-PA (lauryl-VVAGKK-Am) and EE-PA (lauryl-VVAGEE-Am) were used as nonbioactive molecules. Theoretical charges of the PAs at neutral pH are as follows; LN-PA: +3, GAG-PA: -3, HAV-PA: +2, EE-PA: -2 and, KK-PA: +2. Gel formation done by neutralizing the theoretical charges. Resins were swollen in DCM for 30 min prior to synthesis. Next, resins were washed with DMF. Amino acids were coupled to the resins in the hydrophilic to hydrophobic order. Fmoc protecting groups on each amino acid were removed prior to each coupling by incubating the resin in piperidine/DMF (20% v/v) solution for 20 min. Carboxylate groups were activated by addition of 1.95 mole equivalents of HBTU to 2 mole equivalents of each amino acid and 3 mole equivalents of DIEA for 1

mole equivalent of functional sites on the solid resin and eventually dissolved in 10 mL DMF. Coupling duration was set to be 2.5 h for each cycle. At the end of each coupling reaction, peptide-resin complexes were washed 3x with DMF, DCM and DMF. Couplings were verified by Kaiser Test. After complete coupling, the peptide resin complexes were treated with 10% acetic anhydride/DMF solution for 30 min in order to permanently acetylate the unreacted amine groups. After completion of the peptide sequence, lauric acid was added to the chain which forms the hydrophobic end of the PA molecule by performing coupling for 4 h. In order to synthesize GAG-PA, 4-methyltrityl (MTT) linked lysine amino acid was used, in which, MTT provides selective side chain protection. After the completion of the complete chain of amino acid couplings, MTT group was cleaved by adding TFA/TIS/H₂O/DCM mixture at 5:2.5:2.5:90 ratio and treatment was carried out for 5 min. Excess TFA removal was performed by rotary evaporation and followed by peptide precipitation in diethyl ether overnight at -20 °C. Next, the PA precipitate was centrifuged at 8000 rpm for 20 min. Supernatant was discarded and PAs were dried. The PAs were dissolved in ddH₂O, frozen overnight at -80 °C and lyophilized until no frozen parts were left. PA powders were stored at -20 °C.

2.1.3. Characterization of PA Molecules

2.1.3.1. Purification of PA Molecules by Prep-HPLC

Peptide purification was performed by an Agilent preparative reverse-phase HPLC system equipped with a Zorbax Extend-C18 21.2x150 mm column for basic conditions and a Zorbax SB-C8 21.2x150 mm column for acidic conditions. As the mobile phase, 0.1% NH₄OH or 0.1% formic acid gradient in water and in

acetonitrile were used. Positively charged PAs were treated with 1 mM HCl solution if purity is above 95% and freeze dried.

2.1.3.2. Liquid Chromatography-Mass Spectrometry (LC-MS) Analysis

PA molecules were chemically characterized by LC-MS for their identity and purity. PA solutions were prepared as 1 mM in ddH₂O. LC-MS, Agilent Technologies 6530 Accurate-Mass QTOF system equipped with a Zorbax Extend-C18 column was used to perform the characterizations. PAs were detected according to the optical density at 220 nm.

2.1.4. Secondary Structure Analysis with CD

For investigating the secondary structure of the PA mixtures, PAs were prepared as 1 mM and necessary volumes of PAs were mixed to equalize their theoretical charges. Mixtures and individual PAs were incubated overnight to allow stabilization of the system. A Jasco J-815 CD spectrophotometer was used to perform CD measurements. Samples were prepared at physiological pH and diluted to have a concentration of 0.125 mM prior to the measurement. Measurements were performed with 1 mm quartz cuvette in the range of 190 nm to 300 nm. Data interval was set as 1 nm and scanning speed was set as 100 nm/min.

2.1.5. Atomic Force Microscopy (AFM)

0.1 mM PA solutions were mixed on the 13 mm coverslips at necessary volumes to neutralize the theoretical charges to have a final volume of 60 μ L. The coatings were dried overnight at room temperature. 5 μ m x 5 μ m imaging was performed in tapping mode by using Asylum Atomic Force Microscopy.

2.1.6. Generation of Neurospheres from Mouse E13.5 Embryos

Pregnant Balb-c mice with vaginal plaque follow-up were sacrificed by cervical dislocation at 13.5 days of gestation. After the uterus was opened, the mouse embryos were harvested into tubes containing cold L-15 medium. The heads of the embryos were cut nearly between the eye and the nose, perpendicular to the cervical vertebrae. After the brain was separated from the head, a transverse cut was made on the telencephalic vesicles. The lateral and medial ganglionic eminences (LGE and MGE) were collected in a tube containing L-15 medium with the help of microscissors (Figure 7). After all embryos have been subjected to the same procedure, the pieces were washed several times with the medium. The dissected brain pieces were then subjected to mechanical dissociation and triturated with the

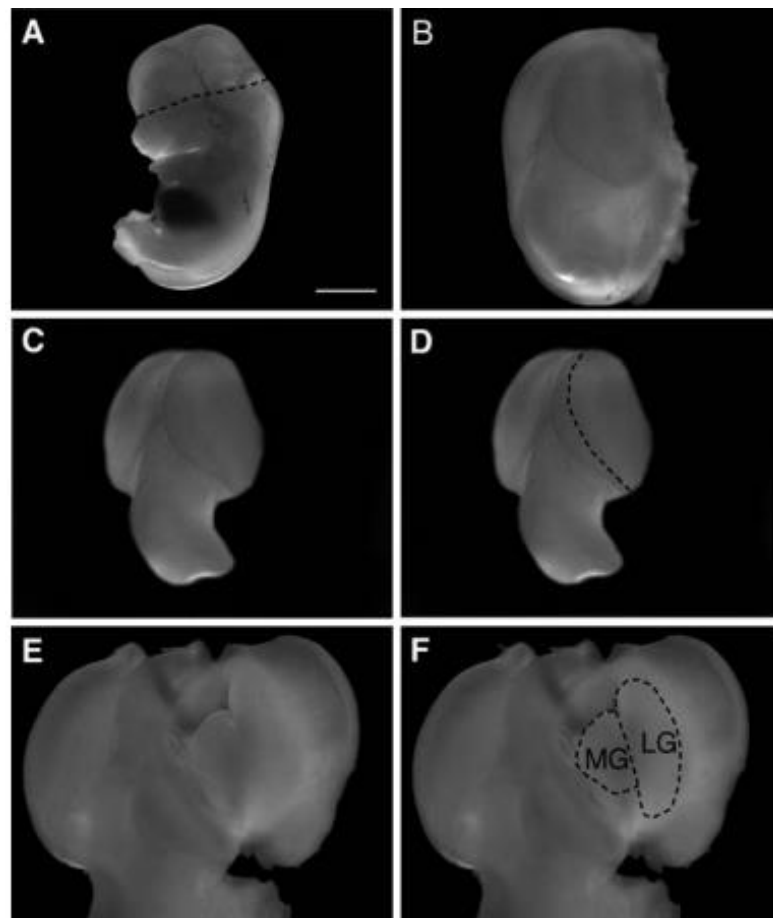


Figure 7 Isolation of neurospheres from the embryonic medial and lateral ganglionic eminences [93]. Reprinted with permission from Elsevier.

help of a sterile pipette tip on a 200 μ L micropipette in the bottom of the tube until the solution appeared milky. Cells were counted using trypan blue and seeded at a density of 10-50 cells per μ L in Neurosphere Expansion Medium (DMEM/F12, 0.5% Gentamicin, 0.6% Glucose, 2% N2 Supplement) supplemented with 10 ng/mL fibroblast growth factor-2 (FGF-2) and 20 ng/mL epidermal growth factor (EGF). Cells were cultured at 37 °C in 5% CO₂ incubator. Undesired cells attach to the tissue culture and are eliminated after 2 passages as suggested by the manual. Floating neurospheres after the passage 2 were used in the experiments. Cells formed floating neurospheres in the medium within 4-7 days depending on the seeding density. In neurosphere culture, the progenitor and stem cells are found heterogeneously. Optimally, neurospheres are comprised of NSCs, neural restricted progenitors, glial restricted progenitors, neurons, astrocytes and oligodendrocytes. All experiments were performed under the approval of Bilkent University Animals Ethics Committee.

2.1.7. Preparation of Peptide Coatings for Cell Culture

PAs were mixed in corresponding volumes to neutralize the theoretical charges. The negatively and positively charged PAs were mixed to have a final volume of 80 μ L for 96 well-plate, 250 μ L for 24 well-plate and 800 μ l for 6 well-plate wells. PAs were prepared as 1 mM, dissolved in ddH₂O sonicated for 20 min and their pH was adjusted to 7.4 prior to coating. The negatively charged PA was firstly coated onto the well and the positively charged PA was added onto the negatively charged

one in a dropwise manner and pipetted a few of times to allow mixing of two components and nanofiber formation. The coatings were then overnight dried in biological safety cabinets and UV sterilized for 1 h prior to cell seeding.

2.1.8. Cellular Viability Analysis

Neurospheres were dissociated mechanically and seeded onto 96 well plates at a density of 10000 cells/well in spontaneous differentiation medium. 24 h after seeding, cells were stained with Calcein-AM and ethidium homodimer for 30 min at room temperature in dark according to the manufacturer's instructions. 5 images per each well were taken and live and dead cells were counted by "Cell Counter" plugin in ImageJ software.

2.1.9. Spontaneous Differentiation of Neurospheres

Floating neurospheres after the 2nd passage were collected when the sphere diameter was approximately 200 μm by centrifuging the supernatant at 1000 rpm for 3 min and seeded onto the coatings or PLL without dissociating. Spheres were cultured in spontaneous differentiation medium (expansion medium lacking the growth factors; DMEM/F12, 0.5% gentamicin, 0.6% glucose, 2% N2 supplement).

2.1.10. Migration of Neurospheres

Roughly 10 to 20 floating neurospheres with approximately 150 μm diameter were seeded onto PA coated 13 mm coverslips in 24 well-plates in spontaneous differentiation medium. On days 2 and 4, images of attached and migrated neurospheres were imaged under inverted microscope.

2.1.11. Immunocytochemical Stainings of Neurospheres

On day 7, the behavior of NSCs and resident and differentiated neurons were qualitatively analyzed by immunocytochemical stainings of SOX-2 and β III-tubulin stainings. Cells were fixed with 4% PFA for 15 min at room temperature and permeabilized with 3% Triton-X for 20 min at room temperature. Next, the cells were treated with either SOX-2 (abcam, ab79351, 1:200) or β III-tubulin (abcam, cat#78078, 1:1000) overnight at 4 °C. The next day, the cells were subjected to goat anti-mouse Alexa-488 conjugated secondary antibody. Cells were mounted onto slides and visualized by Laser Scanning Confocal Microscope (LSM 510, Zeiss).

2.2. Results and Discussion

2.2.1. Design, Synthesis and Characterization of PAs

In this study, the effect of laminin (LN), heparan sulfate (GAG) and cadherin (HAV) mimetic PAs were used as the bioactive groups. The chemical structures of the PAs were displayed on Figure 8. PAs were designed to have a fatty acid chain, lauric acid, a β -sheet forming sequence, VVAG, and a bioactive amino acid group. Oppositely charged PAs were mixed to obtain nanofibers by neutralizing their total charge. The purity and identity of PAs were assessed by LC-MS and revealed a successful synthesis of the molecules (Figure 9 and 10). Secondary structure analysis was performed with CD analyses. Oppositely charged PA samples were mixed and incubated overnight to allow stabilization of the system and diluted. Since the VVAG motif was incorporated to the PA structure, they are expected to have a β -sheet structure as their secondary structure. Except for LN-PA, which spontaneously self-assembled due to its, individual PA samples displayed a negative peak approximately at 190 nm, which is indicative of random coil

structure (Figure 11). However, the PA mixtures exhibited a positive peak approximately at 190 nm and a negative peak approximately at 220 nm, which is indicative of the β -sheet conformation of the secondary structure of self assembled

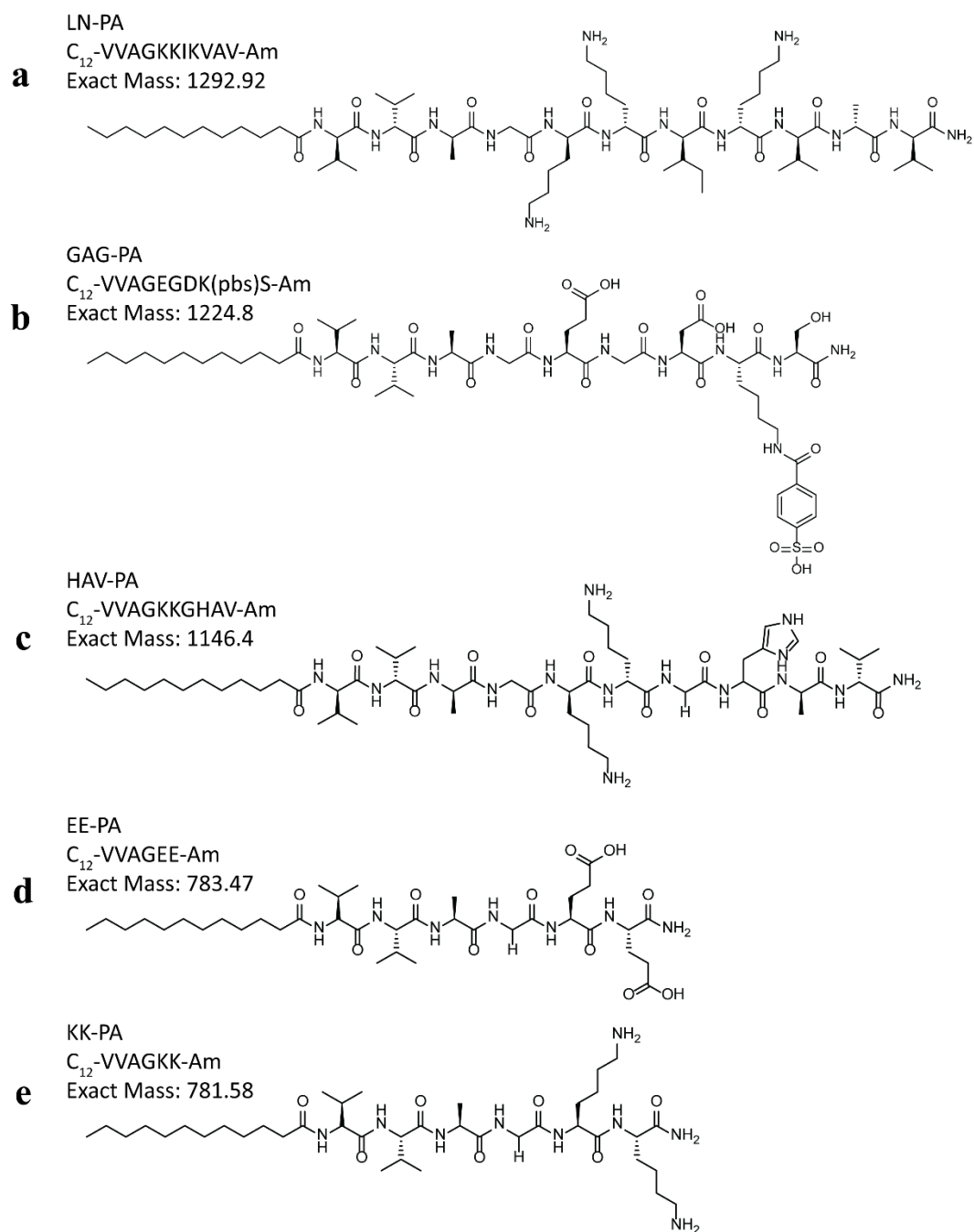


Figure 8 Chemical structures of PA molecules used in this study.

PAs (Figure 12). Noncovalent forces such as hydrophilic/hydrophobic interactions, hydrogen bonding or electrostatic interactions between two charged amino acids play role in the self assembly of PAs.

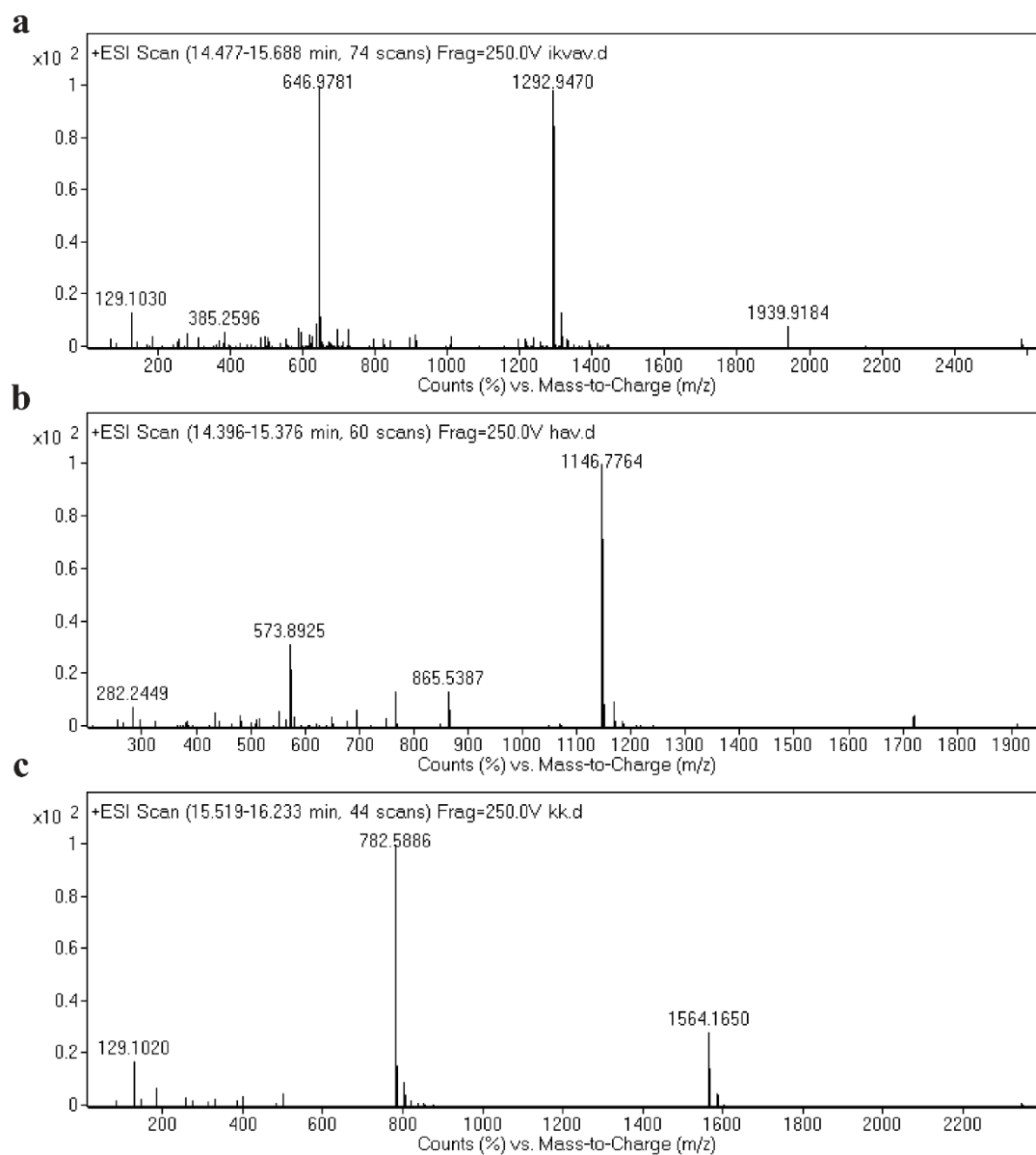


Figure 9 The LC-MS of the positively charged PAs; (a) LN-PA; $[M+H]^+$ (calculated): 1292.93, $[M+H]^+$ (observed): 1292.95, $[M+2H]^{2+}$ (calculated): 646.96, $[M+2H]^{2+}$ (observed): 646.98, (b) HAV-PA; $[M+H]^+$ (calculated): 1149.4, $[M+H]^+$ (observed): 1149.78, $[M+2H]^{2+}$ (calculated): 574.7,

$[M+2H]^{2+}$ (observed): 573.89, (c) KK; $[M+H]^+$ (calculated) = 782.58, $[M+H]^+$ (observed) = 782.59.

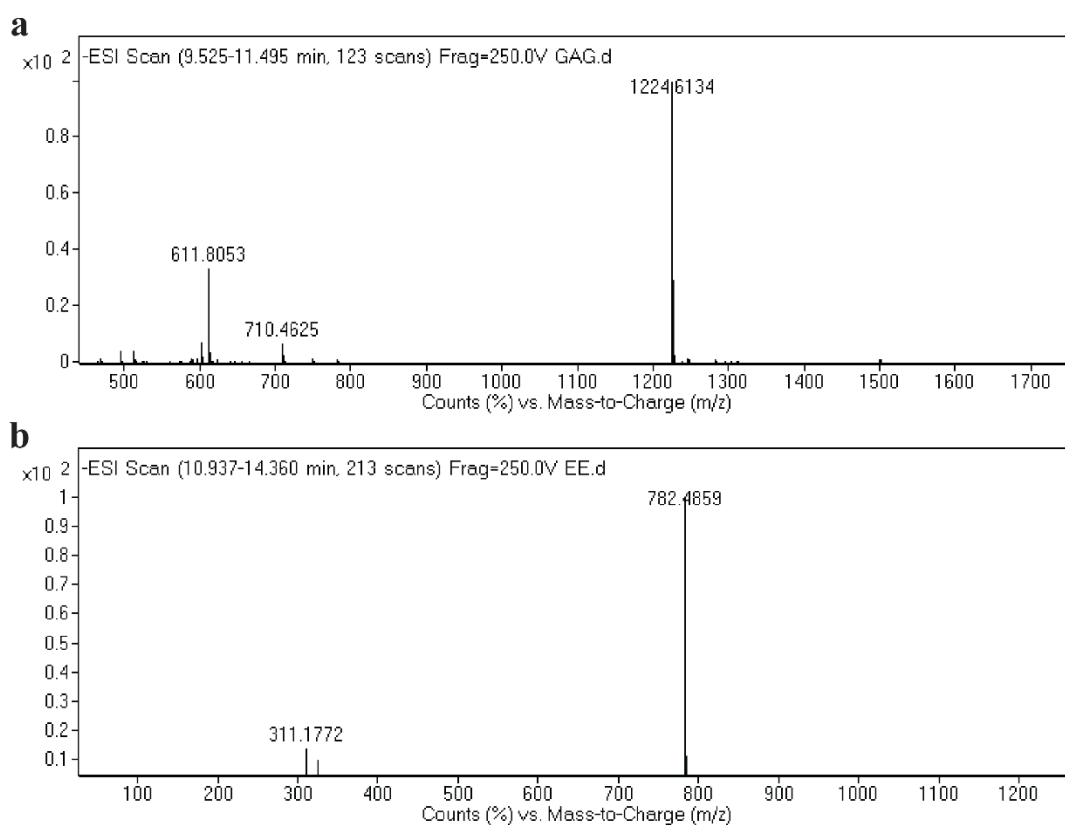


Figure 10 The LC-MS of the negatively charged PAs. (a) GAG-PA; $[M-H]^-$ (calculated): 1225.59, $[M-H]^-$ (observed):1224.61, $[M-2H]^{-2}/2$ (calculated): 612.29, $[M-2H]^{-2}/2$ (observed): 611.81, (b) EE; $[M-H]^-$ (calculated) = 782.47, $[M-H]^-$ (observed) = 782.49.

The PA nanofibers were further characterized by AFM imaging. AFM was preferred due to its high sensitivity. The nanofibers were imaged in non-contact mode, spanning a 5 μm x 5 μm region to observe the fine structure of the nanofibrous mesh and the visible nanofibers. In Figure 13, the height map of the

PA nanofibers can clearly be seen. In all samples, the PA nanofibers were seen to represent a mesh structure. The appearance of the mesh varied depending on the imaging location on the sample. Usually, when the gel is established on the glass overlips, the gels are formed in the concave shape of and the middle parts become relatively more crowded.

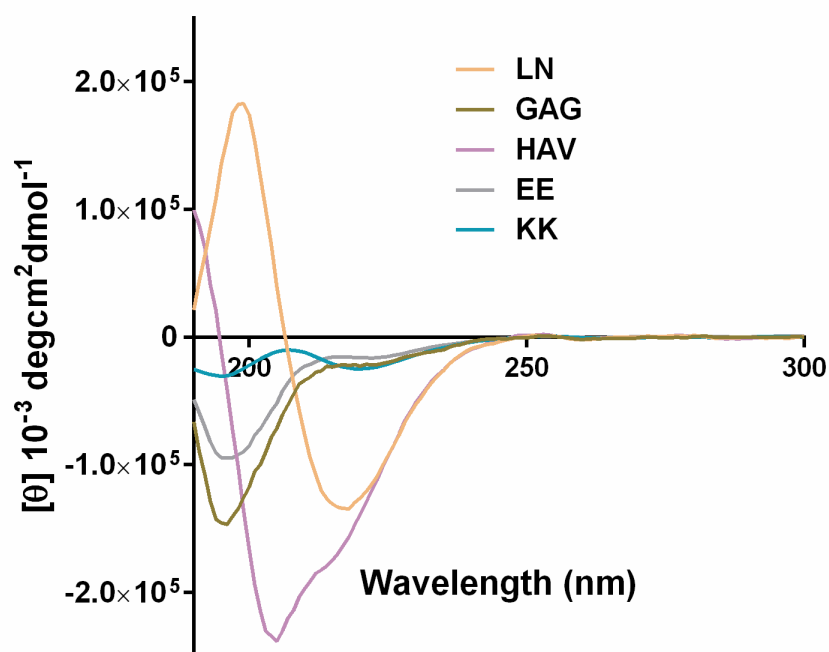


Figure 11 CD spectra of the individual PA solutions.

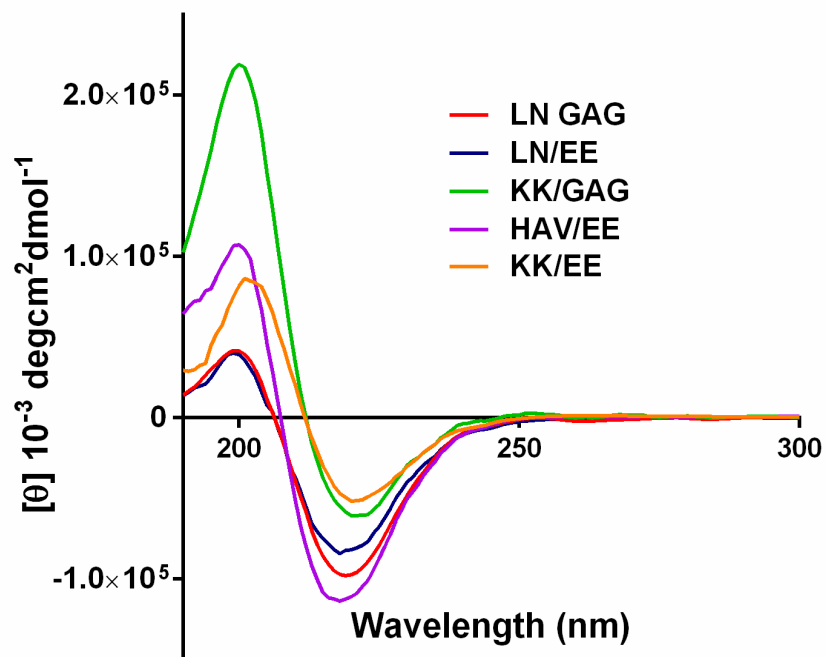


Figure 12 CD spectra of the PA mixtures.

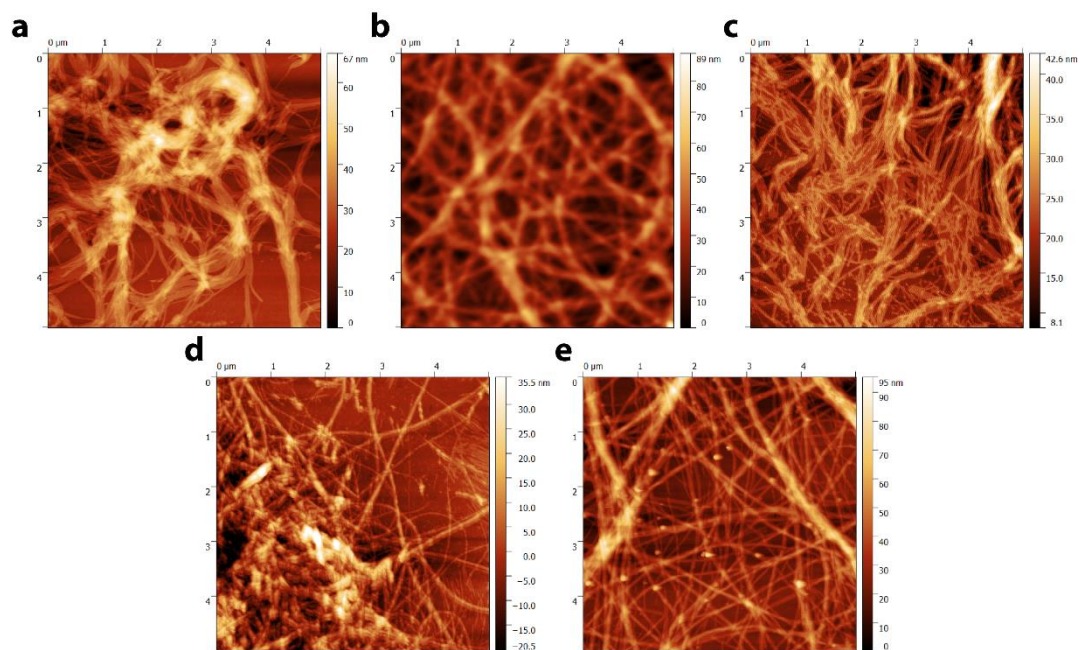


Figure 13 Height map of peptide nanofibers imaged by AFM. (a) LN/GAG, (b) LN/EE, (c) KK/GAG, (d) HAV/EE, (e) KK/EE.

2.2.2. Characterization, Viability and Migration Capacity of Neurospheres on PA nanofibers

Neurospheres were isolated from the embryonic E13.5 mice brains. Ganglionic eminences, which are rich in NSCs were collected and mechanically triturated into a single cell suspension and cultured in medium supplemented with EGF and bFGF. The number of NSCs peak at the ganglionic eminences at the 13.5th day of embryonic development, which was chosen as the day of neurosphere isolation. EGF and bFGF play roles in asymmetric and symmetric cell division during NSC proliferation and are required to be supplemented when embryonic neurospheres are cultured. In neurosphere culture, neurons, oligodendrocytes, astrocytes and NSCs are found together in a 3D environment. This provides an advantage to the NSCs due to the similarity of the cellular mixture in the brain and serves as a model system to investigate how NSCs would behave in a defined 3D matrix, consisting of the naturally abundant cell types in the brain, compared to the conventional 2D monolayer culture systems. In Figure 14, one can see that neurospheres consist of Sox-2 (NSC marker), Nestin (NSC/neural progenitor marker), β III tubulin (neuron specific marker) and S-100 (oligodendrocyte marker) positive cells, mostly comprising of neural stem and progenitor cells.

The ultimate aim of designing cell delivery scaffolds is to promote delivered cells to successfully integrate into the existing tissue and compensate for the cell loss. Therefore, the cell delivery agent should support the host and residing cell viability and primarily be non-toxic. Cell viability was assessed by Calcein-AM/Ethidium Homodimer-1 staining on dissociated neurospheres seeded on PA and PLL coatings. PLL was used as a conventional method to attach embryonic

neurospheres. PA nanofibers were observed to provide a biocompatible environment for the neurospheres 24 h after seeding where percentage viabilities were substantially high. Even a higher percentage viability was observed for LN/GAG and KK/EE groups compared to PLL (Figure 15).

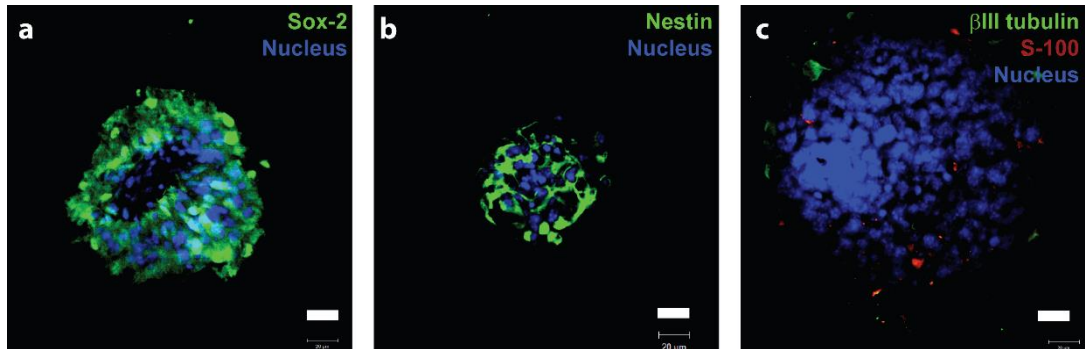


Figure 14 Characterization of neurospheres by (a) sox-2, (b) nestin, (c) β III tubulin and S-100 markers.

Next, the migratory induction potential of the PA nanofibers was assessed. Cells were seeded on the PA nanofiber coatings in spontaneous differentiation medium and the spontaneous migratory behavior of neurospheres was investigated. The radial migration of neurosphere derived cells is referred to as neurosphere migration. Here, the individual potential of LN-PA and GAG-PA, as well as their cooperative effect were investigated. KK/EE group, being the nonbioactive group, was used as the negative control for LN/EE, KK/GAG and HAV/EE experimental groups. As one can see, neurospheres attached and migration on LN/GAG and HAV/EE groups were improved compared to LN/EE, KK/GAG and KK/EE groups on day 2 and 4 *in vitro* (Figure 16 and 17).

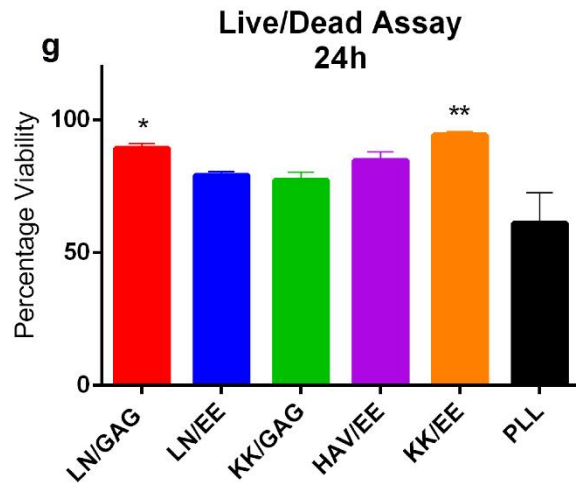
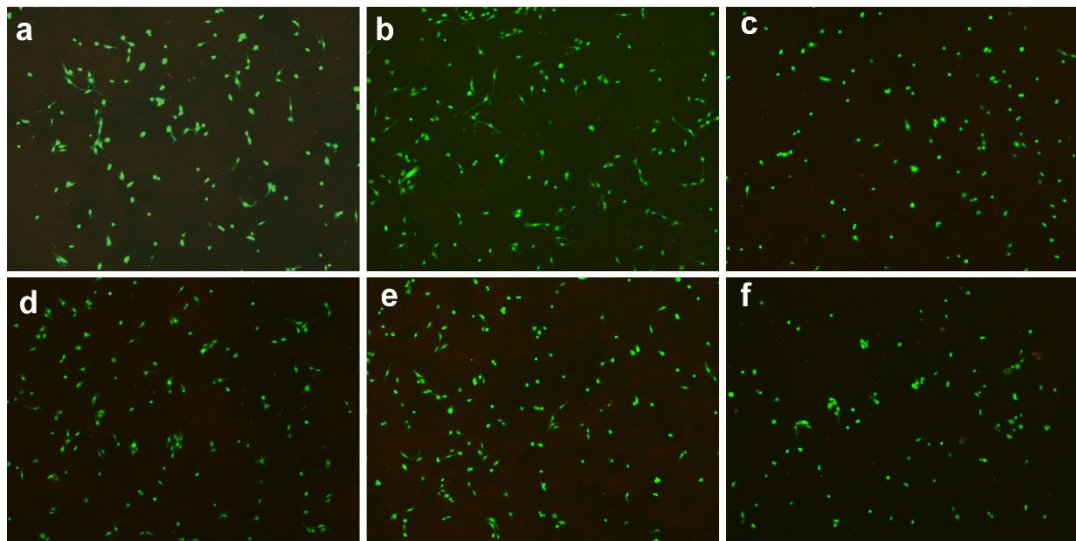


Figure 15 Viability of dissociated neurospheres on (a) LN/GAG, (b) LN/EE, (c) KK/GAG, (d) HAV/EE, (e) KK/EE and (f) PLL coated surfaces. (g) Percentage viability of cells on the PA nanofiber and PLL coated groups. Values represent mean \pm SEM, ** $p < 0.01$.

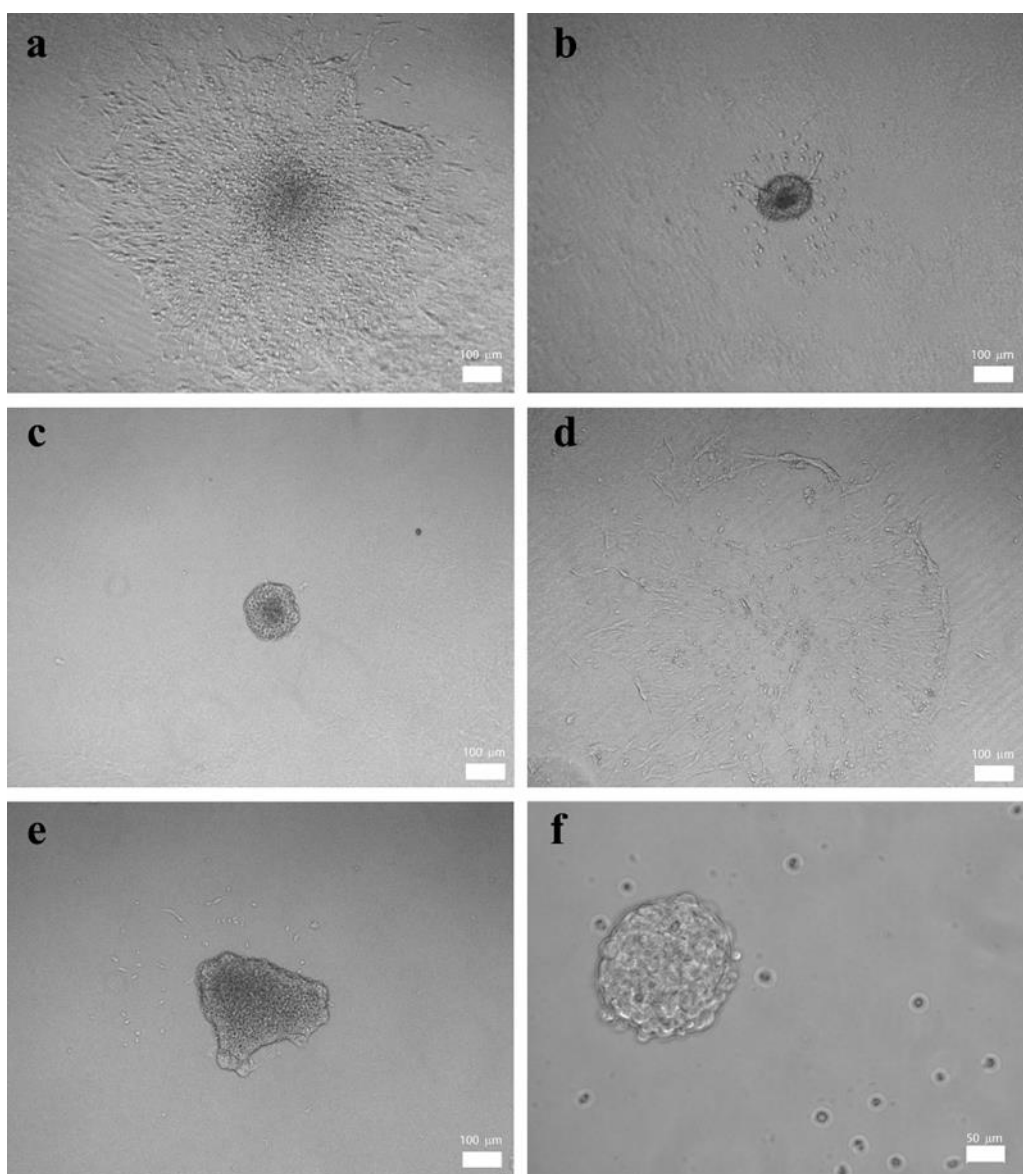


Figure 16 Migration of neurosphere derived cells 2 days after seeding under spontaneous differentiation conditions on (a) LN/GAG, (b) LN/EE, (c) KK/GAG, (d) HAV/EE, (e) KK/EE PA nanofibers.

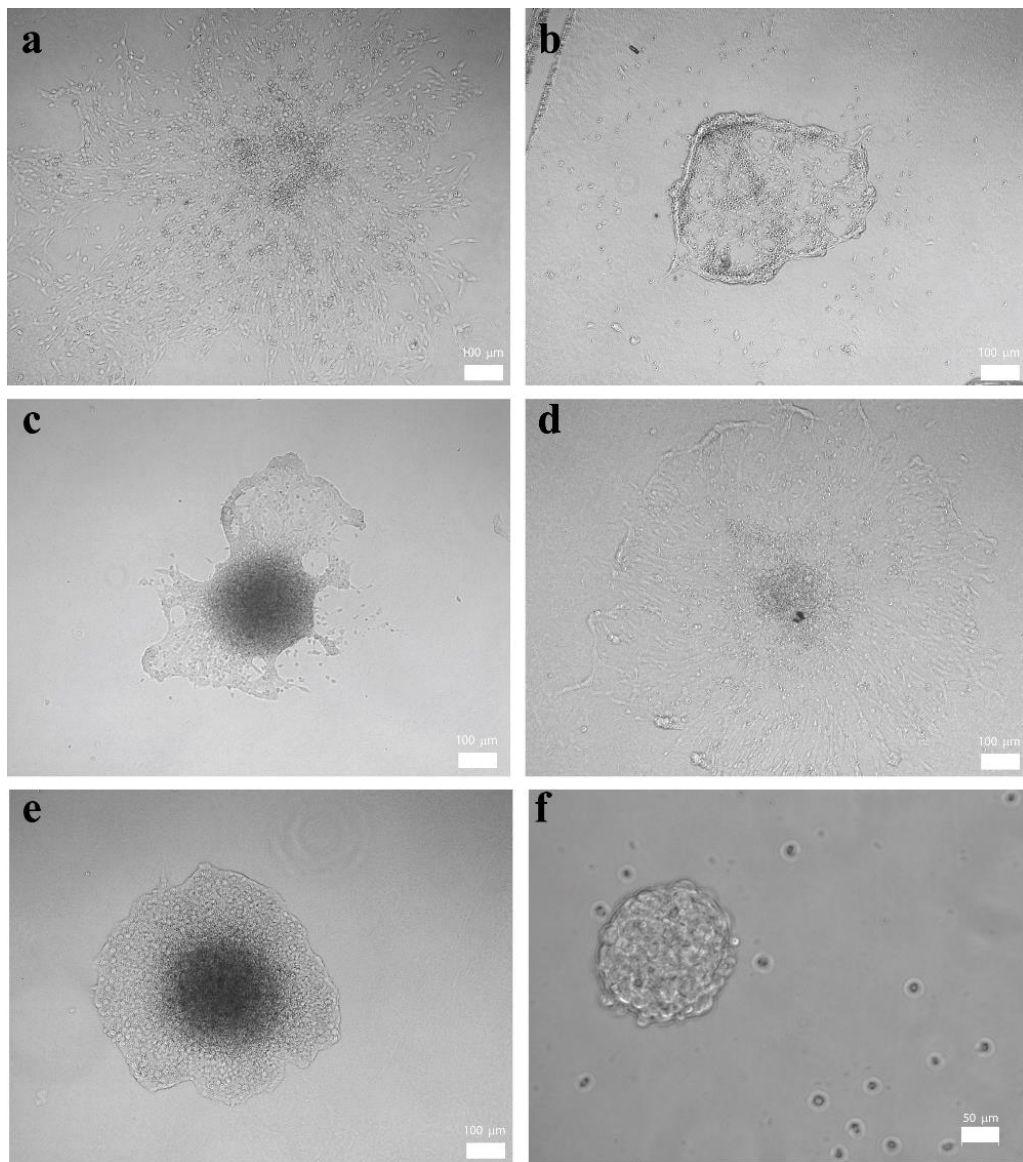


Figure 17 Migration of neurosphere derived cells 4 days after seeding under spontaneous differentiation conditions.

The LN-PA and GAG-PA were seen to cooperatively act on migration of the cells. Also, after day 2, cell migration was seen to continue until the day 4 on each experimental group to some extent. Migration of the cells is important, since after the transplantation of the cells, the cells are aimed to reach to the degenerated part of the brain, rather than being inactive and immobile. The driving forces of NSC

migration from the SVZ are not well known, therefore identification of cues that promote NSC migration is considered to be very significant.

2.2.3. Immunocytochemical Stainings of Migrated Neurospheres on PA Nanofibers

To assess the bioactivity of PA nanofibers on neurospheres, immunocytochemical stainings were performed with either Sox-2 or β III-tubulin antibody on day 7 under spontaneous differentiation conditions. Sox-2 staining showed that NSCs in the neurospheres migrate well on the PA nanofibers. However, the lowest migration capacity was observed on KK/GAG group (Figure 18). Another important criterion is the axonal outgrowth capacity of the existing neurons on the PA nanofibers. It is likely that NSCs underwent differentiation to some extent until day 7, but it should not be assumed that all of these neurons were differentiated from the stem cells in the brain. However, here, axon elongating capacity of the existing neurons on PA nanofibers was also substantially important. On LN/GAG nanofibers, axons were observed to radiate from the neurosphere. In the literature, this is referred to as neurite outgrowth of neurospheres. However, the most striking results on neurite outgrowth was observed on HAV-PA. Neurites were seen to grow radially and a neuronal circuitry was formed. Despite the neurite outgrowth inhibiting activity of HAV peptide, when used as self assembling PA nanofiber scaffolds, they were seen to cause increased neurite outgrowth and formation of a complex neuronal network (Figure 19).

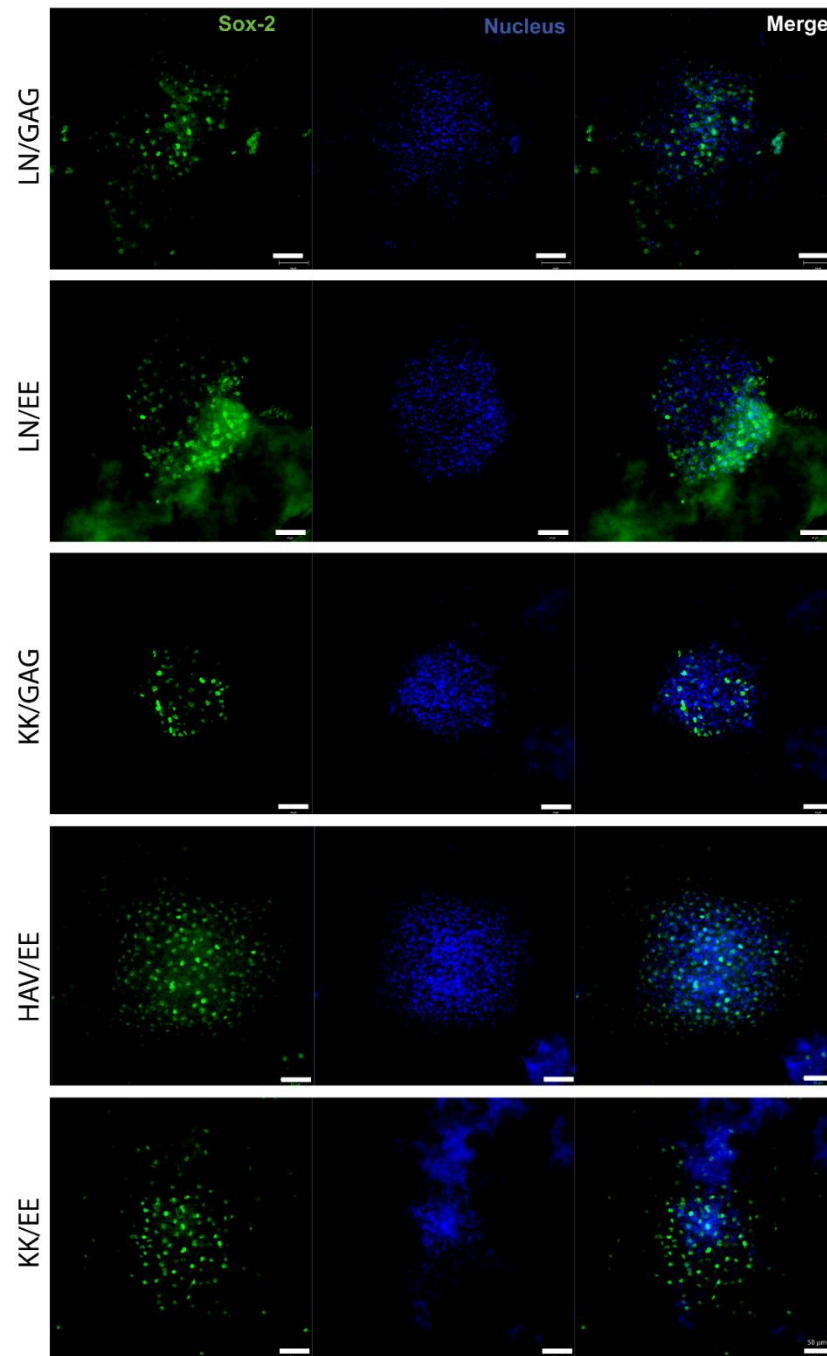


Figure 18 Sox-2 stained neurospheres on LN/GAG, LN/EE, KK/GAG, HAV/EE and KK/EE PA nanofibers. Scale bars are 50 μm .

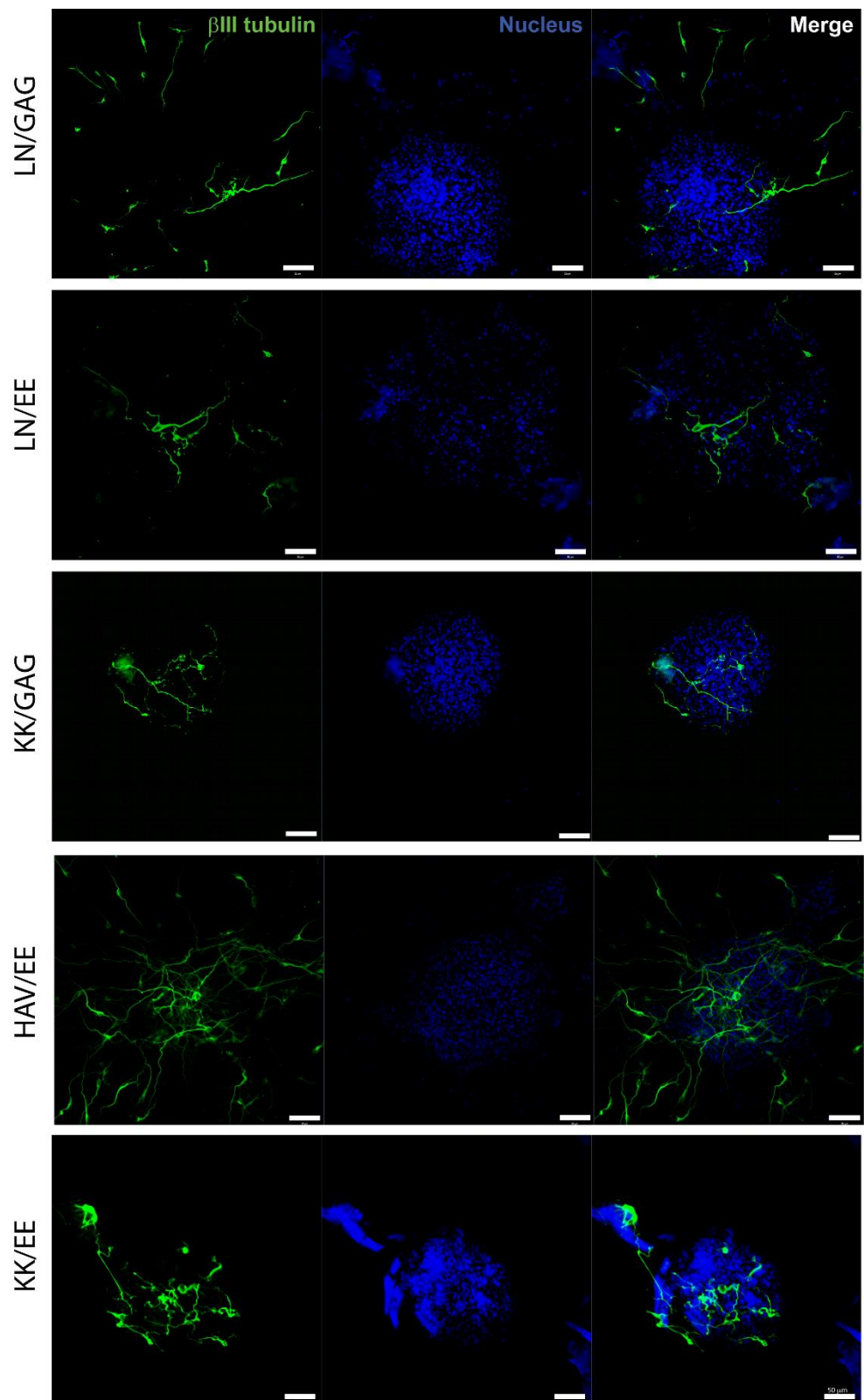


Figure 19 β III tubulin stained neurospheres on LN/GAG, LN/EE, KK/GAG, HAV/EE and KK/EE PA nanofibers. Scale bars are 50 μ m.

2.2.4. Conclusion

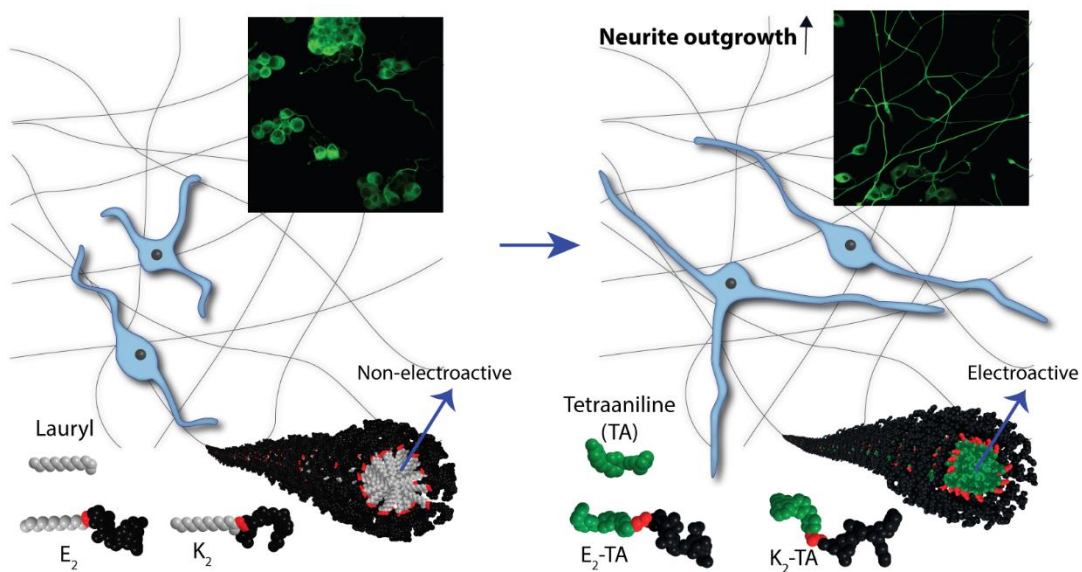
Neural stem cell transplantation has been becoming a promising approach to treat neurodegenerative diseases and brain injuries. Neural stem cells are able to differentiate into the three major cell types in the brain; neurons, astrocytes and oligodendrocytes. However, their abundance, as well as intrinsic capacity to migrate and form neurons at the injury site is very low. Also, even when exogenous cell transplantation is an attractive approach, cells usually do not attach or survive in the lesion following transplantation. The inhibitory molecules in the glial scar further inhibit the regenerative potential. Therefore, there arises a need for usage of exogenous factors to increase the survival, adhesion, migration and differentiation of the transplanted cells. Hydrogels are preferred in this regard in NSC transplantation investigations, due to their porous, and soft nature which is similar to the mechanical properties of the brain. Natural hydrogel such as laminin, collagen or hyaluronic acid can also be used; however their usage in clinical applications is limited due to the potential immunological risks [94]. Alternatively, synthetic hydrogels that have controllable biochemical, mechanical and topographical properties have been attractive and they can be tailored to have specific properties. Self-assembling PAs are good examples of hydrogels. They can be tailored to have a desired secondary structure, and bioactivity can be introduced by incorporating biomimicking peptide sequences. In this study, ECM mimicking PAs (LN-PA and GAG-PA) and cadherin mimicking PA (HAV-PA) were investigated for their potential to promote the migration and neurite outgrowth of neurosphere derived cells. In neurosphere migration assay, LN-PA and GAG-PA

were observed to cooperatively promote migration. moreover, HAV-PA was seen to show striking results in terms of neurite outgrowth.

Chapter 3

3. Biocompatible Electroactive Tetra(aniline) Conjugated Peptide Nanofibers for Neural Differentiation

3.1 Objectives



Following a damage to the peripheral nervous system, limited regeneration can occur depending on the degree of the damage. Peripheral nerve injuries cause devastating problems for the quality of the patient lives. Use of nanobiomaterials can provide therapeutic approaches to treat peripheral nerve injuries. Electroactive biomaterials, in particular, can provide a promising cure for the regeneration of nerve defects. Here, a supramolecular electroactive nanosystem with tetra(aniline) (TA) containing peptide nanofibers was developed and utilized for nerve regeneration. Self-assembled TA-conjugated peptide nanofibers demonstrated conductive and electroactive behavior. The electroactive self-assembled peptide nanofibers formed a well-defined 3D nanofiber network mimicking the

extracellular matrix of the neuronal cells. Neurite outgrowth was improved on the electroactive TA nanofiber gels. The neural differentiation of PC-12 cells is more advanced on electroactive peptide nanofiber gels and these biomaterials are promising for further use in therapeutic nerve tissue regeneration applications.

3.2.1. Introduction

Electrical stimulation is one of the techniques that can accelerate nerve regeneration [95]. Since neurons are electroactive cells, they respond to electrical stimulation by neurite extension and differentiation. Both direct and alternating current (DC and AC) within a voltage range is known to promote neurite outgrowth. DC current was shown to enhance increased and directed neurite outgrowth [96]. One mechanism of promotion of neurite outgrowth by electrical stimulation is by upregulation of growth-associated genes. For instance, cyclic adenosine monophosphate (cAMP) production was upregulated upon electrical stimulation of DRG cells [97]. Polyaniline, polypyrrole, polythiophene, and polyacetylene are some of the known conductive substrates [98, 99].

Usage of conductive materials facilitates the delivery, localization and more effective utilization of the stimulation [100]. In addition to directing the stimulation, since biomaterials should have resembling properties to the target tissue, insulant biomaterials may disturb the physiological integrity of the tissue [101]. As a subcategory of the family of conductive materials, conductive polymers are one of the most frequently investigated materials in tissue stimulation studies. The family of conductive biomaterials also include electrets, piezoelectric and photovoltaic materials [102].

3.2.2. Limitations of Conductive Polymers

Electroactive materials used in nerve cell culture are typically composed of various polymers with electrical conductivity. They are often used to functionalize nerve guidance conduits, nerve implants or as tissue scaffolds. Polymers such as polypyrrole are materials that have become attractive due to their inherent electrical conductivity properties, relatively easy preparation, cell compatibility in vitro and biocompatibility in vivo. Polypyrrole is the most widely used of these polymers [103-106]. Several studies have shown that electrical stimulation of nerve cells cultured on conductive polymer surfaces has positive effects on neurite outgrowth. For example, it has been shown that electrical stimulation results in neurite outgrowth in PC-12 cells grown on electrically stimulated polypyrrole surfaces compared to poly (styrene sulfonate) based surfaces. Also, there is relatively lower neurite outgrowth in the absence of electrical stimulation [107]. In another study, porous conductive polymers loaded with nerve growth factor (NGF) by electrochemical deposition using pyrrole monomers were used to culture PC-12 cells. Electrical stimulation was applied to observe cellular behavioral changes on conductive surfaces. The results showed that surface morphology and electrical stimulation were effective in neurite outgrowth. Another example of polypyrrole functionalization is with poly (d,l-lactide-co-epsilon-caprolactone) (PDLLA/CL) nerve guidance conduits, which enhanced neurite outgrowth compared to PDLLA/CL conduits alone [108]. While biomaterial structure is important for providing facilitated diffusion of neurotrophic factors and nutrients, electrical stimulation has role in increasing cellular behavior such as adhesion, metabolic activity, and neurite outgrowth [109]. It can be produced easily in large amounts

and can be adjusted to have different porosities. However, once it is synthesized, its further processing is very difficult. Mechanically, it is very brittle, has a rigid structure and cannot be dissolved in water after synthesis. Besides polypyrrole, polyaniline (PANI) is another extensively investigated organic conductive polymer. It is formed by repeating units of aniline and is a cost effective, easy to synthesize polymer with relatively good biocompatibility. In one study, neurite outgrowth behavior of NSCs on PANI containing poly (ϵ -caprolactone)/gelatin (PG) conductive platforms was investigated. Conductive nanofibrous PANI/PG scaffolds were observed to be more effective in cell proliferation and neurite outgrowth in NSCs, observed by SEM morphology analysis [7]. However, the biggest problem in the usage of conductive polymers is the insufficiency of their biodegradability and biocompatibility, which limits their usage in nerve regeneration studies [110]. As an alternative strategy, blending of these materials with other biodegradable biomaterials have been proposed to make these polymers biodegradable [100, 111]. Rivers et al. were successful in synthesizing a conductive polymer by binding pyrrole oligomers to thiophene via ester linkages, so that ester linkages get cleaved by esterases *in vivo* [102]. In another study, a block copolymer of polyglycolide and aniline pentamer showed electroactivity and degradability [112]. Several studies showed the effect of electrical stimulation on the axis of neural cell division, neuronal polarity and directed neurite outgrowth [113-115]. However, recently, a significant amount of attention has been given to investigating the effects of conductive biomaterials on tissue regeneration without electrical stimulation [116]. Given the insufficient biodegradability of these polymers, the incorporation of these polymers into peptide nanofibers appears to be more advantageous. Peptide

nanofibers are chemically easily modified, injectable, biocompatible, bioactive, chemically defined synthetic materials. Peptide nanofibers containing bioactive signals have been shown to stimulate neurite growth by mimicking the natural environment of intracellular sclerosis in neuronal cell cultures *in vitro* and have been shown to increase axonal growth *in vivo* in spinal cord injury and to increase glial scar formation and apoptosis by increasing the plasticity of serotonergic neurons [117]. When the peptide amphiphile molecules self-assemble, they form nanofiber structures with signal peptides on the surface where hydrophobic moieties are presented, and these nanofibers come together via electrostatic interactions and hydrogen bonds to form scaffold-like structures. These porous scaffolds can form hydrogels with more than 99% water retention capability at physiological pH [118-120].

Self-assembling peptide amphiphiles have been extensively investigated in neural regeneration studies due to their capability to bear ECM biomimicking signals, hydrogel forming capability and ability to deliver topographical signals. In addition to these properties, considering the brittle, nonbiodegradable and stiff nature of the conductive polymers, covalent linking of the oligomers of polymers to the hydrophobic site of the peptide amphiphiles can be a promising approach in order to obtain hydrogels with conductive properties. By this way, the monomers of the conductive polymers are not covalently linked to each other, however, are found in their immediate vicinity of one another and potentially facilitate charge transfer. By this approach, biodegradable hydrogels are formed and the biocompatibility of the conductive oligomers is possibly improved.

3.3. Experimental Section

3.3.1. Materials

N-phenyl-1,4-phenylenediamine, ammonium persulfate (APS), succinic anhydride, 4-(2',4'-dimethoxyphenyl- Fmoc- aminomethyl)- phenoxyacetamido-norleucyl-MBHA resin (Rink amide MBHA resin), all protected amino acids, lauric acid, HBTU, DIEA, and TFA were purchased from Merck or Sigma-Aldrich. All other chemicals and materials used in this study were purchased from Sigma-Aldrich and used as received. Cell culture materials were obtained from Invitrogen.

3.3.2. Synthesis of Tetra(Aniline)

Tetra(aniline) (TA) was synthesized according to the protocols described in the literature [121]. N-phenyl-1,4-phenylenediamine (0.46 g, 2.5×10^{-3} mol) was dissolved in a mixture solution of acetone (50 mL), deionized water (50 mL) and concentrated hydrochloric acid (HCl) (12.5 mL) and stirred in an ice bath to cool to 0 °C for 30 min. A solution of APS (0.57 g, 2.5×10^{-3} mol in 12.5 mL deionized water) was added dropwise to the reaction mixture over 30 min under vigorous stirring. After the addition of APS, the resulting solution was stirred for 3 h at 0 °C. The dark green crude product was centrifuged and washed with 0.6 M HCl solution and acetone at least three times and tetraaniline in the emeraldine salt state (TA-ES) was obtained. Then, it was dedoped with 0.1 M NH_4OH solution for 1.5 h and washed with deionized water until the pH reached 7 to get TA in emeraldine base state (TA-EB). After drying at 40 °C under vacuum for 24 h, blue-purple TA-EB was obtained. The molecular weight of TA-EB was measured by mass spectrometry to be 365.2 (MH^+/e) (Figure 20).

3.3.3. Synthesis of Peptide Amphiphile Molecules

Solid phase peptide synthesis method was used for the synthesis of non-electroactive oppositely charged lauryl-VVAGEE-Am (E_2) and lauryl-VVAGKK-Am (K_2) and electroactive oppositely charged carboxyl-capped tetra(aniline)-VVAGEE-Am (E_2 -TA) and carboxyl-capped tetra(aniline)-VVAGKK-Am (K_2 -TA) (Figure 21). Peptides were constructed on Fmoc-Rink amide resin. Amino acid couplings were performed with 2 equivalents of Fmoc-protected amino acid, 1.95 equivalents HBTU and 3 equivalents of DIEA for at least 4 h. Fmoc removals were performed with 20% piperidine / dimethylformamide solution for 20 min. For the synthesis of E_2 and K_2 , lauric acid was used as the final sequence. For E_2 -TA and K_2 -TA, before the TA coupling, the free amino group of the valine was conjugated with the linker by reaction with succinic anhydride (2 equivalents) overnight to form free carboxylic acid groups. Then, 2 equivalents of TA, 1.95 equivalents HBTU and 3 equivalents of DIEA were added as the last coupling. Cleavage of the peptides from the resin was carried out with a mixture of TFA:triisopropylsilane:water in a volume ratio of 95:2.5:2.5 for 2 h. The remaining solution was collected and the resin was washed with DCM. Excess TFA and DCM were removed by rotary evaporation. The remaining mixture was triturated with cold ether and precipitate was separated from ether by centrifugation. The precipitate was dissolved in water, and finally, freeze dried. The PAs were further purified by prep-HPLC. After prep-HPLC treatment and freeze drying, white colored E_2 and K_2 , and violet colored E_2 -TA and green colored K_2 -TA were obtained.

3.3.4. Characterization of PA molecules by LC-MS

The identity and purity of PA molecules were assessed by LC-MS (Agilent Technologies 6530 Accurate-Mass QTOF system equipped with a Zorbax Zorbax Extend-C18 column) according to the optical density at 220 nm. A gradient of water (0.1% NH₄OH or 0.1% formic acid) and acetonitrile (0.1% NH₄OH or 0.1% formic acid) was used as the mobile phase.

3.3.5. Purification of PA Molecules

To purify the peptides, an Agilent preparative reverse-phase HPLC system equipped with Zorbax Extend-C18 21.2 mm × 150 mm column for basic conditions and Zorbax SB-C8 21.2 mm × 150 mm column for acidic conditions were used and a gradient of water (0.1% NH₄OH or 0.1% TFA) and acetonitrile (0.1% NH₄OH or 0.1% TFA) was used as the mobile phase. Positively charged PAs were treated with 1 mM HCl solution and lyophilized to remove residual TFA. Sample preparation method is explained in detail for each characterization technique.

3.3.6. FTIR Spectroscopy

Dried samples were mixed with KBr having KBr:sample ratio as 100:1 (w/w) to obtain a homogenous mixture and pressed to form transparent pellets. The absorbances of the samples were collected with a Bruker VERTEX 70 FT-IR Spectrometer in 4000-400 cm⁻¹ range.

3.3.7. Transmission Electron Microscopy

The transmission electron microscopy (TEM) images of the E₂/K₂ and E₂-TA/K₂-TA nanofibers were obtained using an FEI Tecnai G2 F30 TEM at 300 kV and negative staining was performed using 2% (w/v) uranyl acetate.

3.3.8. Scanning Electron Microscopy

For scanning electron microscopy imaging, samples were prepared on a Si-wafer surface by mixing oppositely charged PA solutions. E₂ and K₂, and E₂-TA and K₂-TA solutions (13 mM) were mixed at 1:1 ratio. 15 min after gel formation, ethanol exchange was carried out and then gels were dried by using a critical point dryer (Tousimis Autosamdri-815B). The dried samples were coated with 10 nm of Au/Pd and images were taken by using an FEI Quanta 200 FEG SEM.

3.3.9. Secondary Structure Analysis

The CD spectra of E₂/K₂ and E₂-TA/K₂-TA solutions and their oppositely charged mixtures at 1:1 molar ratio (25 mM), were measured in wavelengths between 500 nm to 190 nm with a data interval and pitch of 1 nm, DIT as 4 s, band width as 1 nm, the sensitivity as standard and scanning rate as 100 nm min⁻¹ by Jasco J-815 CD spectrophotometer and all measurements representing three accumulations.

3.3.10. Rheological Measurements

Rheological measurements of E₂/K₂ and E₂-TA/K₂-TA samples were carried out by Anton Paar MCR-301 rheometer equipped with PP25-SN17979 measuring device with 25 mm diameter and measuring distance was adjusted to 0.5 mm. The oppositely charged peptide solutions (13 mM) were mixed on the bottom stage of the rheometer and time sweep test was performed at a constant angular frequency ($\omega = 10$ rad/s) and deformation ($\gamma = 0.1\%$) for 30 min. Frequency and strain sweep tests were performed after equilibrium time of gel formation. For frequency sweep, the angular frequency was logarithmically ramped from $\omega = 0.1$ to 100 rad/s in the linear viscoelastic range ($\gamma = 0.1\%$). Strain sweep test was carried out at a constant strain of 0.1 %. Measurements were reported as the average of three repeats for each sample.

3.3.11. UV-vis-NIR Spectroscopy

UV-vis-NIR absorption spectra of the solutions of TA-dedoped and TA-doped (with HCl) in DMF, E₂-TA and K₂-TA solutions in water and E₂-TA/K₂-TA mixtures in water (0.125 mM) were measured from 1200 nm to 200 nm using Cary 5000 UV-vis-NIR Spectrophotometer.

3.3.12. Conductivity Measurements

For conductivity measurements, 20 μ L of E₂-TA and K₂-TA solutions or E₂-TA and K₂-TA solutions (13 mM) were mixed and casted on the surface of cleaned glass slides. After waiting for 30 min at room temperature, the sample coated glass slides were dried in a vacuum oven at 37 °C for 24 h. Then, gold electrodes (30 nm) with channel lengths of 20 μ m and channel widths of 3750 μ m were deposited via an Ossila OFET shadow mask using thermal evaporator. The current-voltage ($I-V$) characteristics of the samples were measured at ambient air and room temperature using a two-probe configuration on a Semiconductor Parameter Analyzer (Keithley 4200-SCS). The conductivity of the samples was determined from the following equation 1:

$$4. \quad \sigma = \frac{1}{R} \frac{l}{dW}$$

(1)

where σ is the conductivity of the sample, R is the resistance of the sample, W is channel width, l is the channel length of the gold electrodes and d is the thickness of the sample as determined by AFM measurements.

3.3.13. Peptide Coating and Cell Culture

PA solutions were UV sterilized prior to gel formation. 50 μ L volumes from each component were mixed to form 2 mM E₂/K₂ and E₂-TA/K₂-TA gels on 13 mm

glass coverslips. Coverslips were dried overnight and UV sterilized for 1 h prior to cell seeding. PLL was left in the well for 10 min and washed with 1X PBS at pH=7.4. 2×10^4 PC-12 cells were seeded on the coatings in expansion medium (Roswell Park Memorial Institute medium (RPMI-1640), 2 mM L-glutamine, 5% fetal bovine serum (FBS), 10% horse serum (HS), 1% penicillin/streptomycin (P/S)). The next day, the medium was replaced with the PC-12 induction medium. MEM medium (Gibco), 2 mM glutamine, 2% horse serum, 1% FBS, 1% P/S medium supplemented with 20 ng/mL rat nerve growth factor (NGF) was used to induce the cells. 3 days after induction, half of the medium was refreshed by supplementing with 40 ng/mL NGF (Sino Biological®, Cat no. 50385MNAC250).

3.3.14. Biocompatibility of PC-12 Cells

3×10^4 PC-12 cells (ATCC® CRL-1721™) were seeded on E₂-TA/K₂-TA, E₂/K₂ and PLL coated 13 mm coverslips in expansion medium. After 24 h, cell medium was discarded and cells were treated with 500 ng/mL Calcein-AM (Thermo Fisher Cat no. C3100MP) and 4 µg/mL ethidium homodimer-1 (Thermo Fisher Cat no. E1169) in 1X PBS at pH 7.4 for 30 min at room temperature. Images were taken with an inverted fluorescent microscope at 100x magnification.

For Alamar Blue Assay (Invitrogen), 40 µL from each component was mixed to form 2 mM E₂/K₂ and E₂-TA/K₂-TA gels in 96-well plate. Gels were dried overnight and UV sterilized. Coatings were washed with culture medium and 3×10^4 PC-12 cells were seeded onto them. For PLL coatings, PLL was left in the well for 10 min and washed with 1X PBS at pH 7.4. 24 h after seeding, 20 µL of Alamar Blue reagent was added to 200 µL of the medium and the cells were incubated at 37

°C for 4 h. The fluorescent signal was measured by microplate reader at 570 nm excitation and 585 emission wavelengths. Cell free controls were used as blanks for each experimental group. PLL group was taken as the positive control group and statistical significance was determined by one-way ANOVA test.

3.3.15. Quantification of Neurite Lengths

7 images per well were taken by an inverted microscope at 200x magnification from three replicates 6 days after induction. Neurite length was quantified by ImageJ software. Neurites that were at least 10 μm long were used for calculations. Cell number was determined by “Cell Counter” plugin in ImageJ software. Average neurite length was determined by dividing the total length by total cell number. Percentage of neurite bearing cells was determined by calculating the ratio of cells with neurites to the total cell number. Results were analyzed by one-way ANOVA.

3.3.16. Immunocytochemical Stainings

Peptide coating and cell culture were performed as described previously. Cells on day 6 were fixed with 4% paraformaldehyde/PBS for 15 min and permeabilized in 0.3% Triton X-100 for 15 min at room temperature. Samples were blocked with 10% (w/v) bovine serum albumin/PBS and 10% (w/v) goat serum/PBS for 30 min at room temperature, followed by incubation in β III tubulin primary antibody (ab78078, 1:1000) in 0.3% Triton X-100 overnight at 4°C. Goat anti-mouse IgG (H+L) Alexa Fluor 488 was used as the secondary antibody (Millipore AP124JA4, 1:500). The nuclei were stained with 1 μM TO-PRO-3 (Invitrogen) in PBS for 15 min at room temperature and samples were mounted with Prolong Gold anti-fade Reagent (Invitrogen). Negative staining lacking primary antibody was also

performed. Imaging of the samples was performed by using confocal microscopy (Zeiss LSM510).

3.3.17. Western Blotting

Peptide and PLL coatings were performed as explained in the neurite extension part. 1.05×10^4 cells/cm² were seeded on the coatings. Cells were lysed in RIPA buffer with 1x protease inhibitor cocktail (Thermo Scientific) 24 h after induction with NGF. Protein concentrations were determined with BCA Protein Assay. Equal amounts of proteins were loaded in three replicates for each group and separated by 12% SDS-PAGE gels. Proteins were transferred to PVDF membrane, blocked with 5% nonfat-milk in TBS-T at room temperature for 2 h and incubated overnight with ERK1/2, Abcam, ab130004, 1:2000) and pERK1/2 (Abcam, ab50011, 1:1000) primary antibodies at +4 °C; and incubated with HRP conjugated secondary antibody (Millipore 12–349 Goat Anti Mouse IgG, 1:1000) at room temperature for 1 h. Chemiluminescent signal enhancement system (Invitrogen, Novex ECL) was used to visualize the expected bands. Mild stripping was used to detect GAPDH (Millipore, MAB374 1990892, 1:600) bands as internal controls. Each band was normalized to its corresponding GAPDH band.

3.3.18. Statistical Analysis

The given values are represented as mean \pm sem (standard error of means). All experiments were performed in three replicates. As statistical analyses, one-way ANOVA was utilized as stated in each experimental section. As the post-hoc test, Bonferroni was used.

3.4. Results and Discussion

3.4.1. Design and Characterization of Peptide Amphiphile Nanofibers

In this study, a TA moiety was used as an electroactive core for the fabrication of self-assembling negatively (E_2 -TA) and positively (K_2 -TA) charged electroactive peptide amphiphile molecules.

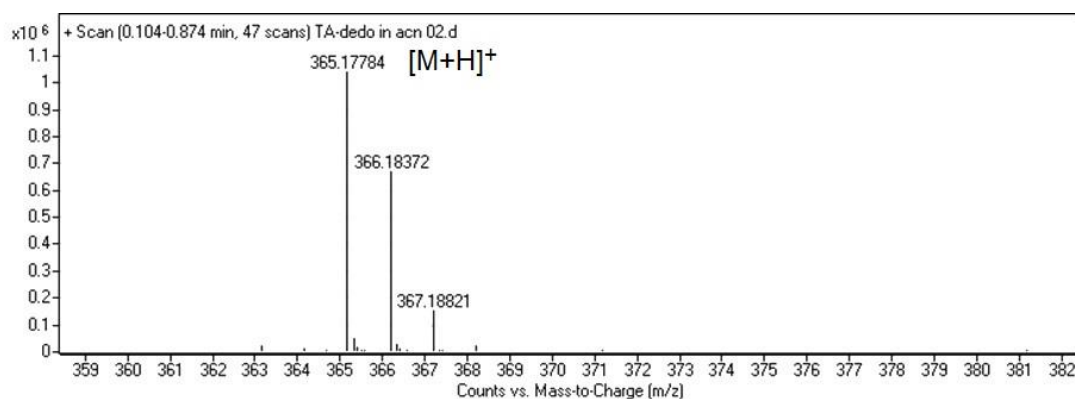


Figure 20 Mass spectrum of TA-EB in acetonitrile, $[M+H]^+$ (calculated) = 365.17, $[M+H]^+$ (observed) = 365.18.

The TA unit was synthesized from the aniline dimers and its mass spectrometry was measured as 365.2 (MH^+/e). TA coupling to the peptide sequence was achieved using a succinic anhydride linker. The TA unit promotes hydrophobic and π - π stacking interactions, while β -sheet forming amino acids (VVA) provide hydrogen bonding, and two glutamic acid (EE) or lysine (KK) residues facilitate solubility in water and further induce self-assembly into fibrillar nanostructures upon mixing oppositely charged molecules at neutral conditions via charge neutralization. To figure out the effect of the electroactive unit on neural regeneration, the results were compared with non-electroactive PA molecules containing lauryl group instead of

the TA moiety (E₂ and K₂). The chemical structures of the electroactive and non-electroactive PAs are shown in Figure 21.

All PAs were synthesized by using Fmoc solid phase peptide synthesis method. The LC-MS spectra of non-electroactive peptide amphiphiles (E₂ and K₂) and electroactive ones (E₂-TA and K₂-TA) are shown in Figure 21 (a-b) and Figure 21 (c-d), respectively.

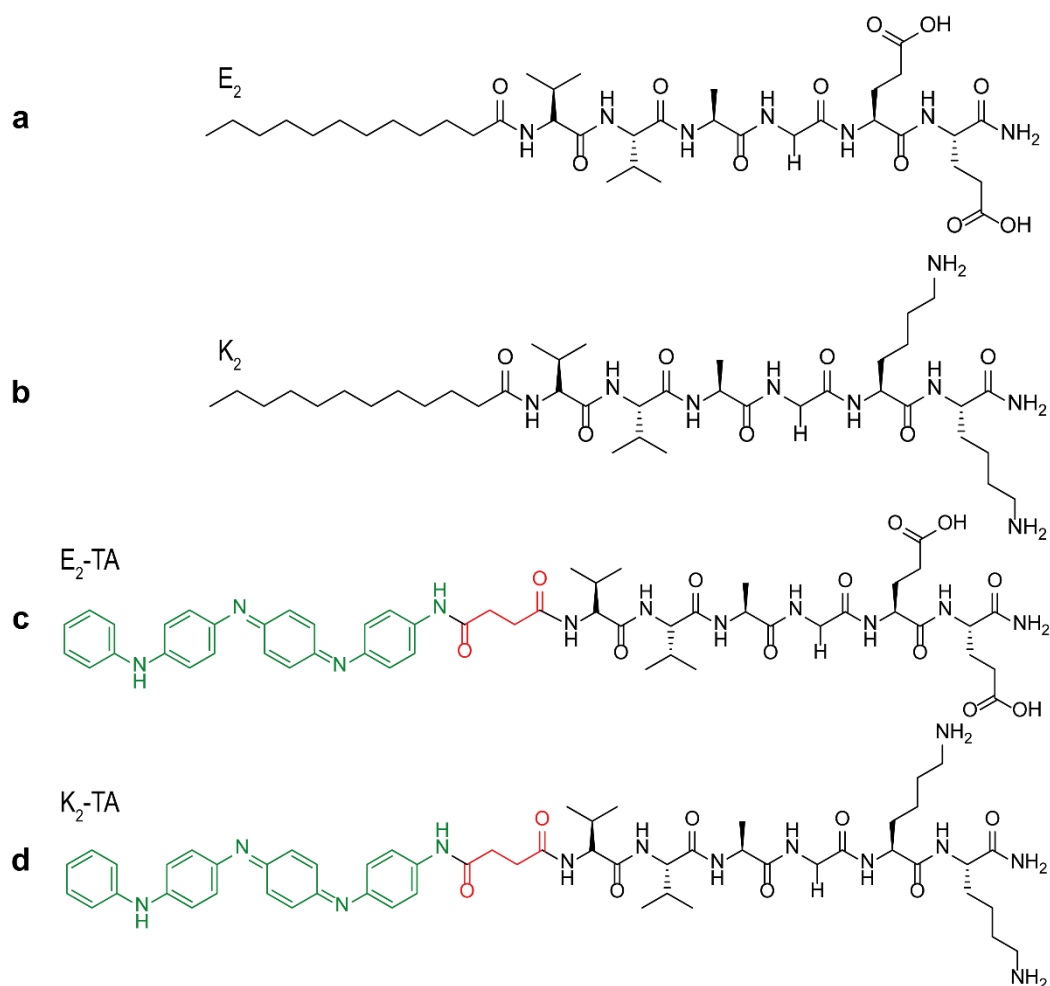


Figure 21 Chemical structures of peptide amphiphiles

The observed molecular mass values were in good agreement with the theoretical molecular mass and confirmed the chemical structures of the desired molecules.

Chemical structures of the TA and PAs were also characterized by FTIR (Figure 23). The 1600 and 1510 cm^{-1} peaks were assigned to the C=C stretching vibrations of quinoid and benzenoid rings of TA, respectively. The 1308, 1169 and 839 cm^{-1} bands

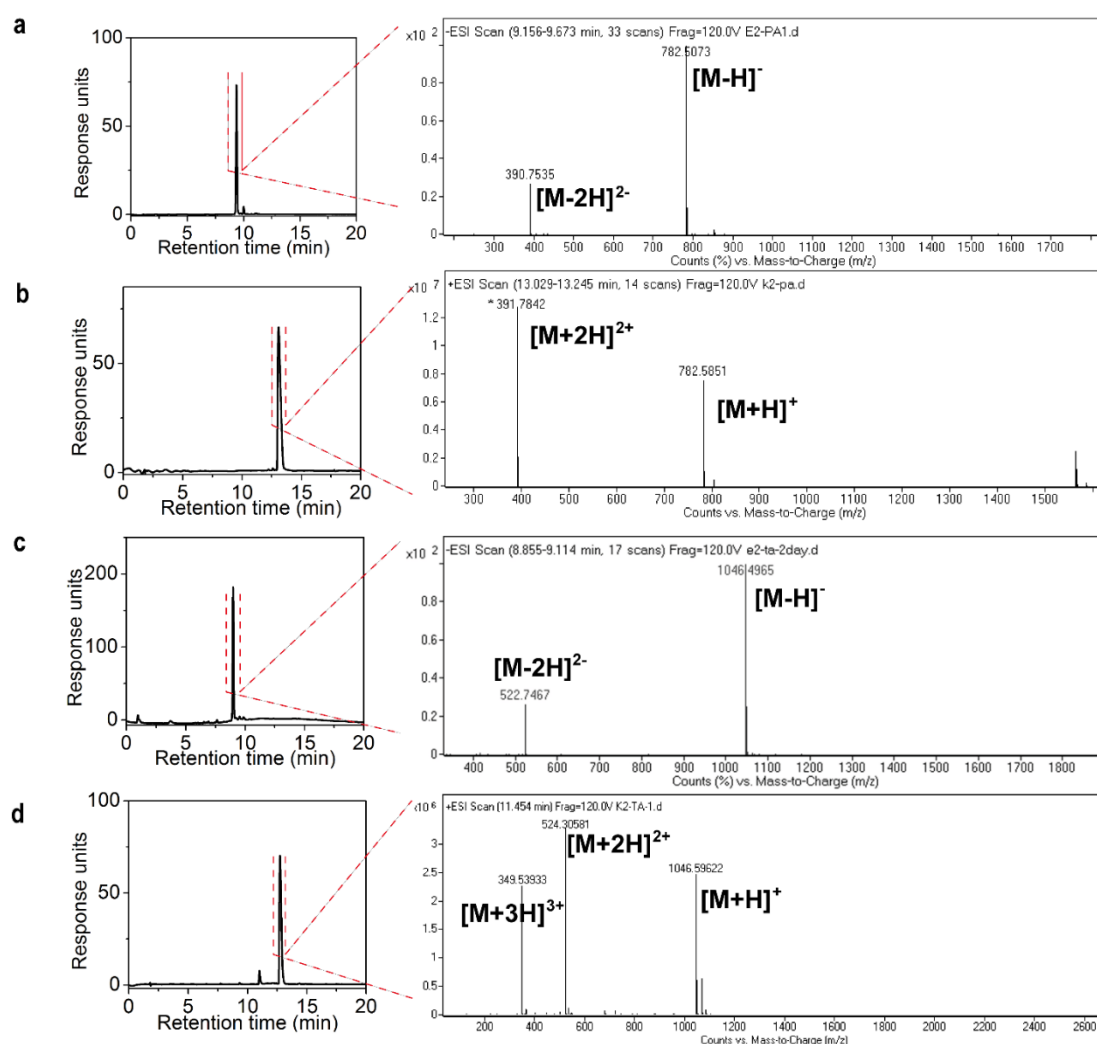


Figure 22 LC-MS spectrum of (a) E₂, [M-H]⁻ (calculated) = 782.47, [M-H]⁻ (observed) = 782.51, [M-2H]²⁻ (calculated) = 390.74, [M-2H]²⁻ (observed) = 390.75, (b) K₂, [M+H]⁺ (calculated) = 782.58, [M+H]⁺ (observed) = 782.59, [M+2H]²⁺ (calculated) = 391.79, [M+2H]²⁺ (observed) = 391.78, (c) E₂-TA, [M-H]⁻ (calculated) = 1046.48, [M-H]⁻ (observed) = 1046.50, [M-2H]²⁻ (calculated) = 522.74, [M-2H]²⁻ (observed) = 522.75, and (d) K₂-TA, [M+H]⁺ (calculated) =

1046.59, $[M+H]^+$ (observed) = 1046.60, $[M+2H]^{2+}$ (calculated) = 523.80, $[M+2H]^{2+}$ (observed) = 524.31, $[M+3H]^{3+}$ (calculated) = 349.53, $[M+3H]^{3+}$ (observed) = 349.54.

correspond to the secondary aromatic C–N stretching vibrations, aromatic C–H in

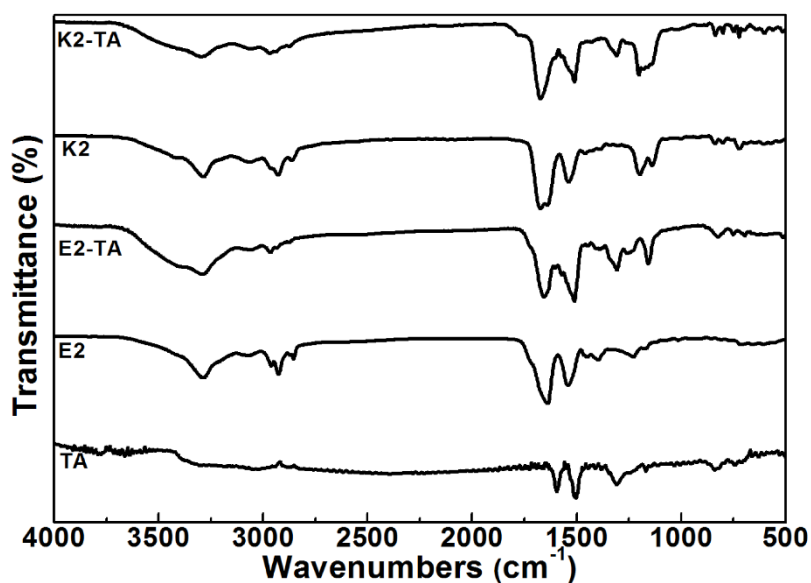


Figure 23 FTIR analysis of PAs.

plane bending vibrations and the C–H out-of-plane bending deformation in 1,4-disubstituted benzene rings, respectively [122]. Bands around 3287, 3072 and 2960-2874 cm⁻¹ in the FTIR spectrum of E₂ were attributed to N–H and C–H stretching vibrations indicating the presence of amide and aliphatic C–H groups in the PA structure, respectively. The peaks around 1640 cm⁻¹ and 1538 cm⁻¹ can be referred to amide-I bond and amide-II bond which was associated with vibration stretching of C=O and N–H bonds, respectively. Similar bands were also observed for K₂. In addition to the peaks observed for E₂, the following peaks were observed in E₂-TA;

1601, 1307 and 825 cm^{-1} , which can be ascribed to C=C stretching vibrations of quinoid ring, aromatic C-N stretching vibrations and the C-H out-of-plane bending vibrations of two adjacent hydrogen atoms on a 1,4-disubstituted benzene rings, respectively, indicating the successful conjugation of TA unit to the peptide structure. Distinctive absorption bands indicating TA presence was also observed for K₂-TA.

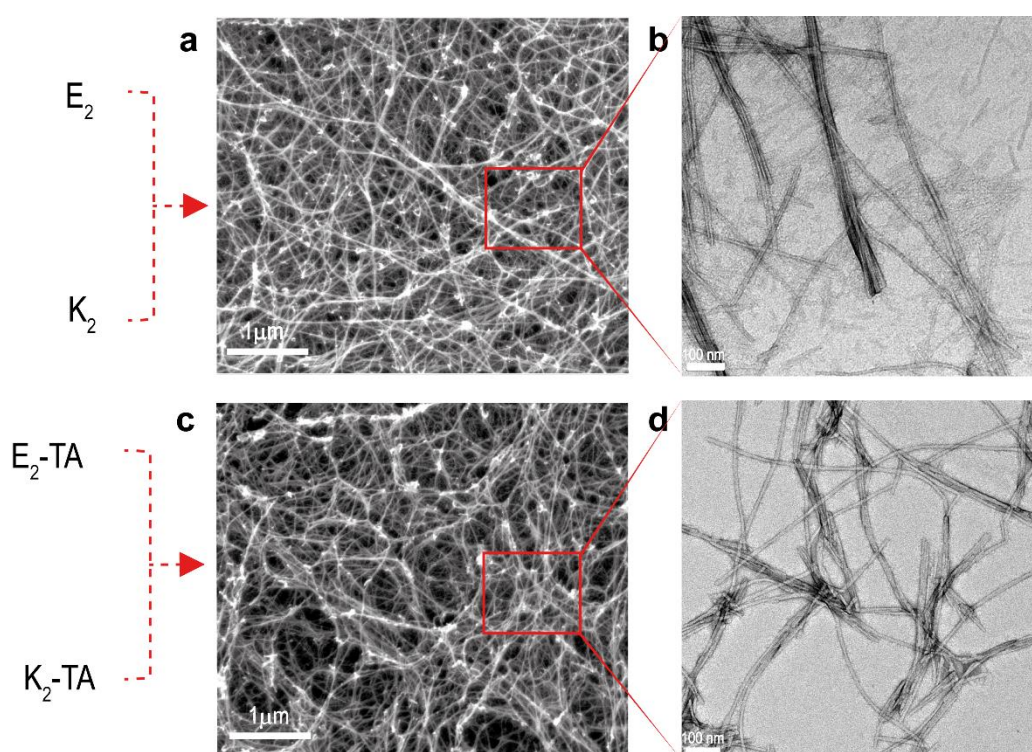


Figure 24 SEM and TEM analysis of PA mixtures.

SEM and TEM analyses were performed to understand the morphological features of the self-assembled nanostructures upon mixing oppositely charged PA molecules. The SEM images of E₂/K₂ (Figure 24e) and E₂-TA/K₂-TA (Figure 24f) revealed their self-assembled well-defined three-dimensional porous nanofiber

network structure. TEM images showed that the self-assembled nanofibers have a diameter of ca. 10 nm (Figure 24 g-h).

A positively charged molecule, K_2 , was used to induce nanofiber formation together with the negatively charged E_2 through electrostatic interactions. E_2 and E_2 -TA molecules form nanofibers through self-assembly when mixed at a 1:1 ratio with K_2 and K_2 -TA, respectively. Secondary structures of the electroactive and non-electroactive PAs and their self-assembled corresponding mixtures were studied

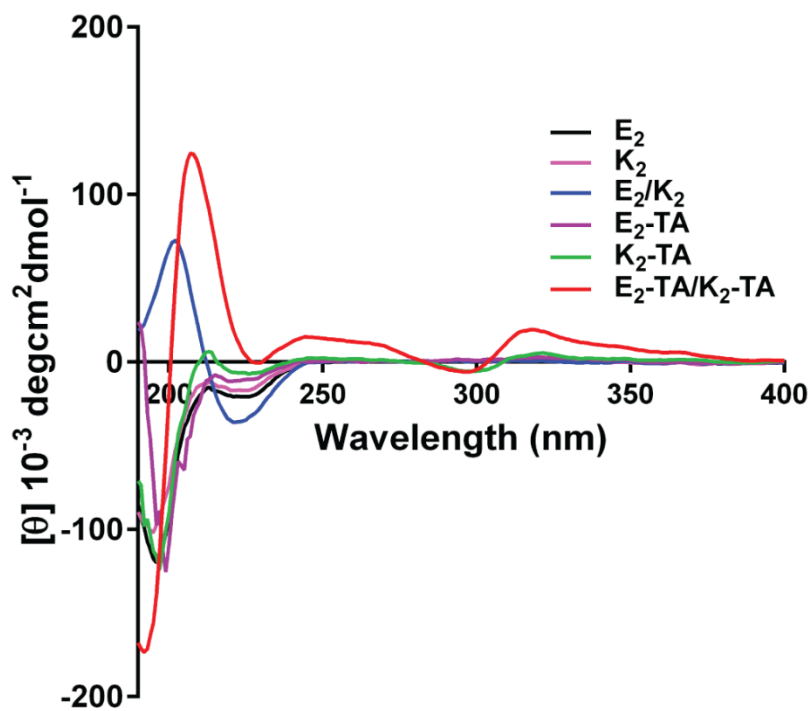


Figure 25 CD spectra results of individual PAs and their mixed forms.

with CD spectrometer. In Figure 25, individual PAs showed random coil structures (negative signals at around 197 nm and 225 nm) [123]. A chiral absorbance maximum at 202 nm and minimum at 222 nm was observed for E_2/K_2 corresponding to the β -sheet secondary structure of the nanostructures,

predominantly. On the other hand, E₂-TA/K₂-TA showed a negative signal at 295 nm and positive signals at 207 nm and 245 nm, which corresponds to the β -turn peptide structures. The shape of the CD curves was similar to that of β -turn peptides, which were characterized by a negative peak at 180–190 nm and two positive peaks at 200–205 nm and 220–230 nm [124]. In addition to these peaks, in the region of the characteristic absorption of the π - π^* transition of the benzenoid ring, a new positive signal appeared at 318 nm as a result of supramolecular chirality of the self-assembled TA motifs, which was not observed for individual electroactive peptides. Increased hydrophobic and H-bonding interactions between TA units with self-assembly are responsible for the supramolecular chirality of E₂-TA/K₂-TA [125, 126].

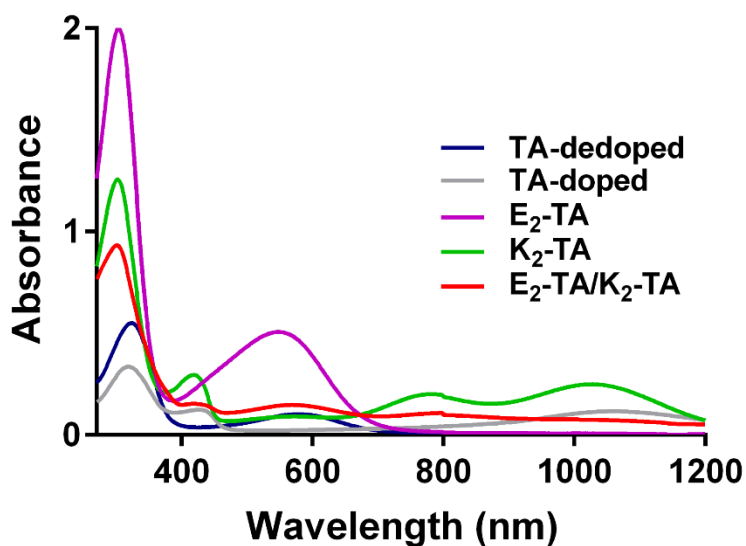


Figure 26 UV-vis-NIR absorption spectroscopy of PA molecules and their mixed forms.

Oligoaniline-based materials reversibly switch their emeraldine base (EB) state to emeraldine salt (ES) state by acid doping. With the addition of acid, quinoid N atoms in the EB state are protonated and this ES structure shows remarkable conductivity. This transition can be monitored via UV-vis-NIR absorption spectroscopy (Figure 26). Two peaks around 323 nm and 578 nm were attributed to the π - π^* transition of the benzene ring and excitonic transition from benzenoid to quinoid ring (π_B - π_Q) for TA-dedoped, respectively. After doping with acid, the peak at 578 nm disappeared because TA was fully doped by HCl. On the other hand, new peaks at 433 nm and 1053 nm appeared for the TA-doped system due to the formation of polarons and delocalized polaron transitions, respectively [127]. After the prep-HPLC purification step, it was obvious that the TA moiety was in the EB state for E₂-TA due to basic conditions, while it was in the ES state for K₂-TA due to acidic conditions. E₂-TA exhibited two absorption peaks similar to TA-dedoped at 304 nm and 549 nm corresponding to the characteristic absorptions of the π - π^* transition of the benzenoid ring and the excitonic π_B - π_Q transition, respectively, whereas K₂-TA showed absorption peaks at 420 nm, 781 nm and 1030 nm, which indicated that TA was in its conductive form and after conjugation of TA motif to the peptide sequence, TA retained its electroactivity. However, broad and weak absorption peak at 568 nm (the excitonic π_B - π_Q transition) indicated that K₂-TA in aqueous solution was partially doped. When oppositely charged electroactive peptide amphiphiles were mixed, E₂-TA/K₂-TA exhibited absorption peaks at 419 nm and 781 nm associated with existence of polaron species containing cation radicals and a weak absorption peak at 578 nm indicated partially doped TA in the structure. Additionally, characteristic absorption bands of TA showed hypochromic

shift for electroactive PAs due to the formation of an amide group which is an electron-withdrawing group compared to the amino group of TA, and the electron density of the quinoid ring decreased. In addition, non-electroactive peptide amphiphiles did not show any absorption peaks in the studied wavelength range.

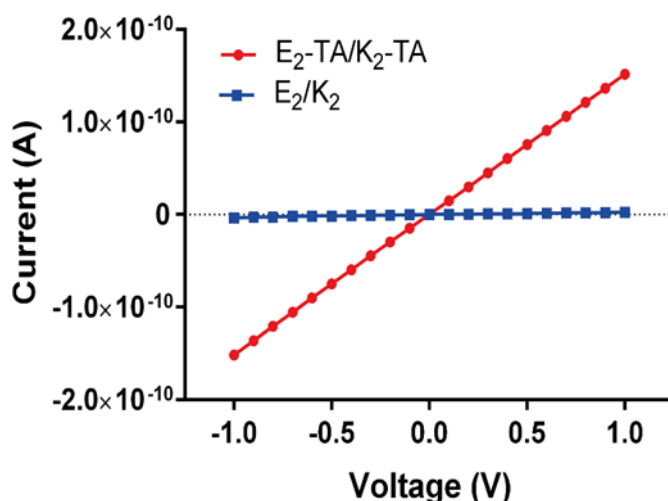


Figure 27 Current/voltage (I/V) curves of E_2/K_2 and E_2 -TA/ K_2 -TA.

For conductivity measurements, the current/voltage (I/V) curves of TA-doped, TA-dedoped, E_2/K_2 and E_2 -TA/ K_2 -TA were determined with the aid of patterned contact gold electrodes in a two-point probe configuration with an electrode separation of 20 μm . Representative sample casted glass substrate with patterned contact gold electrodes and $I-V$ curve for E_2 -TA/ K_2 -TA and E_2/K_2 are given in Figure 27 and the film thicknesses of the samples were determined via AFM analysis to calculate conductivity values of the samples. Representative AFM images of the samples are shown in Figure 28. The $I-V$ curves were linear for E_2 -TA/ K_2 -TA indicating Ohmic contact [128]. The conductivity values of the samples were determined as following: $\sigma_{E_2/K_2} = 1.10 \times 10^{-10} \text{ S}\cdot\text{cm}^{-1} < \sigma_{\text{TA-dedoped}} = 7.45 \times 10^{-7} <$

$\sigma_{E_2-TA/K_2-TA}=6.97 \times 10^{-6} \text{ S}\cdot\text{cm}^{-1} < \sigma_{TA-doped}=2.55 \times 10^{-3} \text{ S}\cdot\text{cm}^{-1}$. Non-electroactive species including simple alkyl blocks, oligopeptide, and other bio-based blocks, inorganic materials, and other structure-directing domains or functional units may lead TA to show decreased conductivity depending on the length of the conjugated group [129]. Nevertheless, it was clearly observed that conjugation of TA to an insulating peptide segment leads to obtaining higher conductivity compared to the non-electroactive E_2/K_2 . Guo *et al.* have reported an electroactive porous tubular scaffold for neural tissue engineering by blending hyperbranched degradable conducting copolymer and linear polycaprolactone. The conductivity of the blend films doped with (\pm)-10-camphorsulfonic acid was observed between 3.4×10^{-6} - $3.1 \times 10^{-7} \text{ S}\cdot\text{cm}^{-1}$ depending on the hyperbranched conducting copolymer content. It was reported that these conductivity values were sufficient for many tissue engineering applications [130]. Although the conductivity of the E_2 -TA/ K_2 -TA nanofibers was relatively low due to conjugation of insulating peptide moiety and not using any additional doping agent, the conductivity of this novel supramolecular electroactive nanofiber was nevertheless sufficient to transfer bioelectrical signals *in vivo* as living activity in the body involves low microcurrents [131].

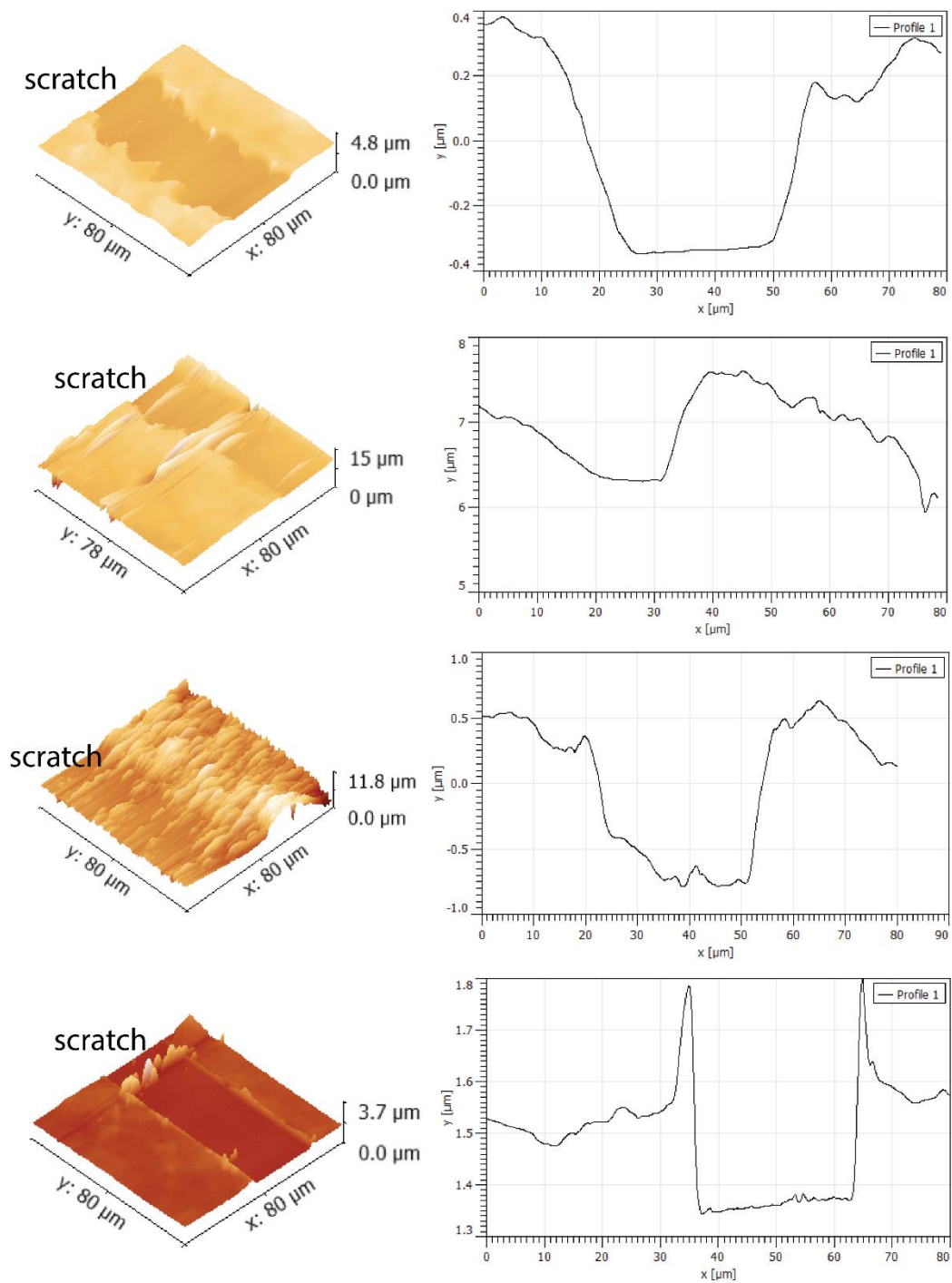


Figure 28 Representative AFM images and height profiles of (a) E₂/K₂ (b) E₂-TA/K₂-TA (c) TA-dedoped, (d) TA-doped samples casted on glass substrate (a

scratch has been made in the film closed to the contact gold electrode to determine film thickness).

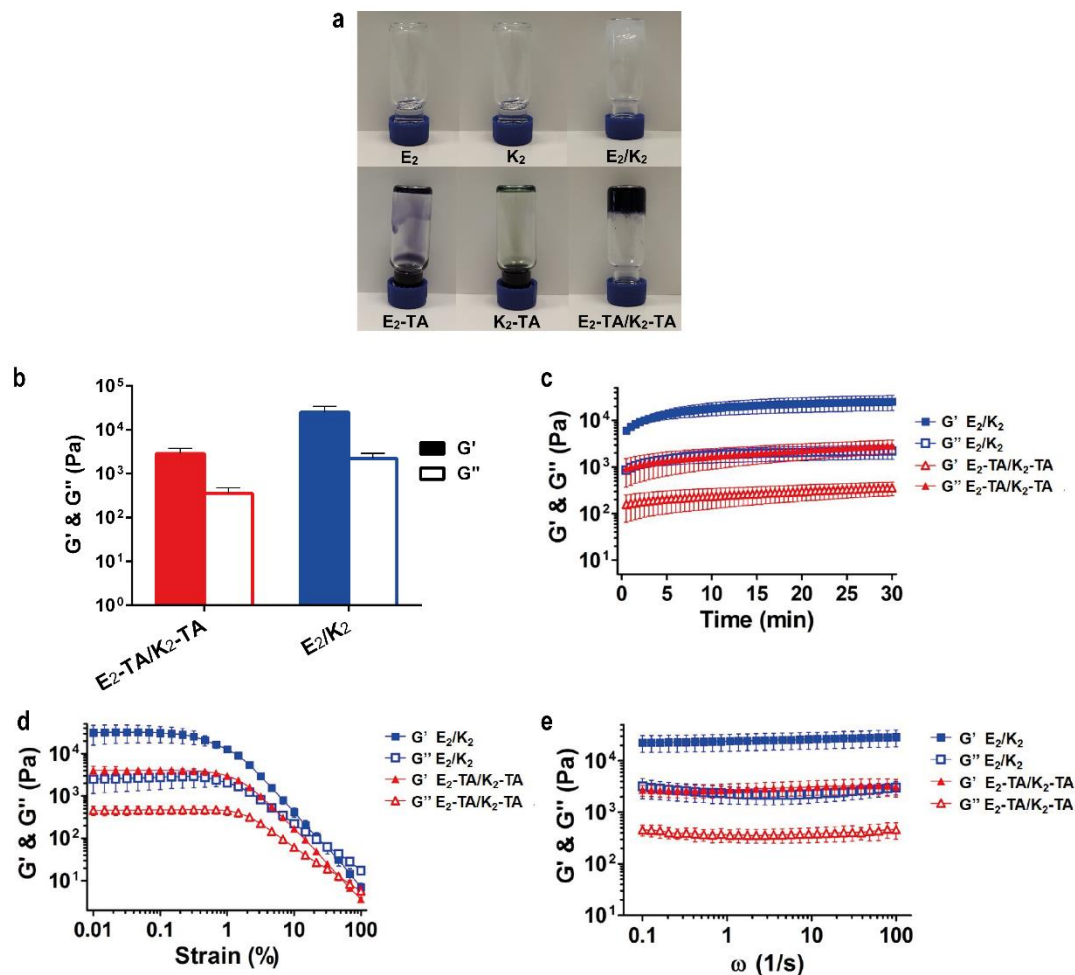


Figure 29 Gel formation and rheological analyses of PA hydrogels. The photo of the solution of non-electroactive and electroactive PAs and self-supporting gel behaviors upon their corresponding mixture (a). Elastic and viscous modulus of E_2/K_2 and $E_2\text{-TA}/K_2\text{-TA}$ gels (b). Time sweep test at constant angular frequency ($\omega = 10$ rad/s) (c). Strain (d) and frequency sweep tests of E_2/K_2 , $E_2\text{-TA}/K_2\text{-TA}$ gels (e).

Gel formations upon mixing oppositely charged PAs are shown in the Figure 29a. Stiffness and elasticity characteristics of the gel systems were studied by oscillatory rheology. The gelation kinetics were first monitored by time sweep test (Figure 29b) within the linear viscoelastic region (LVE) and both gels reached a plateau indicating the complete gelation. The moduli values at the end of 30 min are given in Figure 29c, where storage moduli (G') were determined to be higher than the loss moduli (G'') confirming the formation of gels with elastic character. G' of the E_2/K_2 gel was 9 times higher than E_2 -TA/ K_2 -TA gel and thus had more rigid network structure and higher entanglement density of the nanofibers. A strain sweep test was performed to investigate the viscoelastic properties and to determine critical strain value of both gels. In Figure 29d, change in modulus values was observed with increasing strain amplitudes and gels maintained their G' in LVE. As the strain was increased, the gel network began to break down and collapsed showing lower G' than G'' , i.e., displayed liquid-like behavior. E_2/K_2 showed a slightly lower critical strain value (γ_c was determined from the intersection of the tangents in the linear regime and the strain dependent regime) [132] than the E_2 -TA/ K_2 -TA. It can be attributed to the relatively higher network stability of E_2 -TA/ K_2 -TA due to the higher entanglement points of the nanofibers in the network. Furthermore, the gels maintained their moduli values within the studied frequency range as shown in Figure 29e due to having elastic dominant gel characteristics over the viscous one. It can be also concluded that the mechanical properties of the electroactive PA nanofiber were in the range of neural tissue as the natural stiffness values of the individual neurons and glial cells range from 0.5 to 1.6 kPa and the overall peripheral nerve tissue stiffness values change from 150–300 kPa [133].

In biomedical applications, the biocompatibility of a biomaterial is crucial. Ideally, the biomaterial should support adhesion and survival of the cells. To evaluate the biocompatibility and further investigate the bioactivity of E₂-TA/K₂-TA gels, PC-12 cells, derived from rat pheochromocytoma were used as a model cell line for

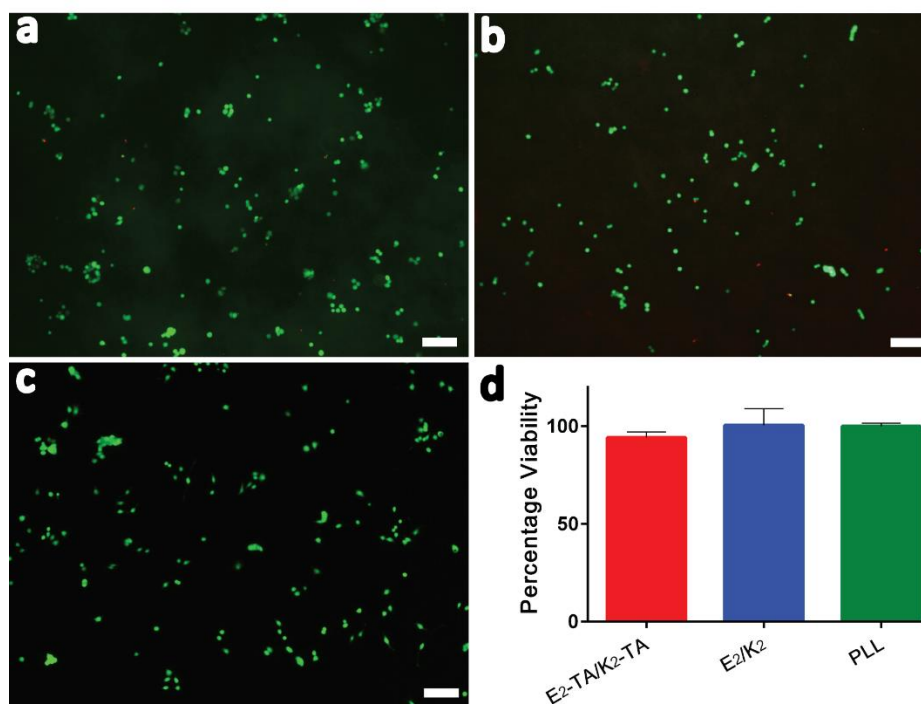


Figure 30 Biocompatibility of PC-12 cells on (a) E₂-TA/K₂-TA and (b) E₂/K₂ gels and (c) PLL coated surfaces. (d) AlamarBlue® viability analysis of PC-12 cells on E₂-TA/K₂-TA and E₂/K₂ gels and PLL coated surfaces.

neural differentiation. Live-dead and Alamar Blue® assays were utilized to determine cell viability. Figure 30 shows the live and dead cells stained in green and red, respectively. Peptide nanofibers were observed to provide a biocompatible environment for PC-12 cells. A PLL coated surface is conventionally used to attach the cells onto the surface, and thus was used as a positive control. The cell viability and metabolic activity were observed to be similar to these of PLL coated surfaces

for E₂-TA/K₂-TA and E₂/K₂ coated surfaces as determined by Alamar Blue® assay. Neurites are the projections that arise from the cell body of a neuron or a neuron-like cell before the neuron matures completely.

In a mature neuron, projections later become dendrites or axons. PC-12 cells can be induced with NGF to result in neurite outgrowth. Neurite lengths after NGF induction can give quantitative information about the degree of neural differentiation [134]. In order to determine the effect of E₂-TA/K₂-TA gels on neural differentiation, the neurite processes of PC-12 cells 6 days after NGF induction (Figure 31 a-c) were measured; average neurite length and percentage of cells with neurites were determined for each group, in addition to calculation of the relative percentage frequency of neurite length values as a histogram plot. The morphology of the cells and neurite projections on different groups can be visualized by staining against β III tubulin, a neural marker. The neurites on both E₂-TA/K₂-TA and PLL groups were observed to be slightly thicker and straighter, whereas neurites on E₂/K₂ seemed weaker and curved (Figure 31 a-c) The histogram data provide visual data showing that the frequency of low length neurites on E₂/K₂ peaks around 30-40 μ m neurite length, whereas the percentage frequency of longer neurites is higher on E₂-TA/K₂-TA and PLL. The histogram statistics proved that neurite lengths on E₂-TA/K₂-TA, E₂/K₂ and PLL have 25% percentile values of 34.5 ; 23.9 ; 32.8, median values of 57.3 ; 39.4 ; 53.4 and 75% percentile values of 93.5 ; 68.1 ; 90.2 respectively, which are all higher values compared to the values of E₂/K₂ (Figure 31d and Table 1). Measurements of the average neurite length showed that there were significantly longer neurites on E₂-TA/K₂-TA gels compared to E₂/K₂ gels as shown in Figure 31e. PLL was used as a

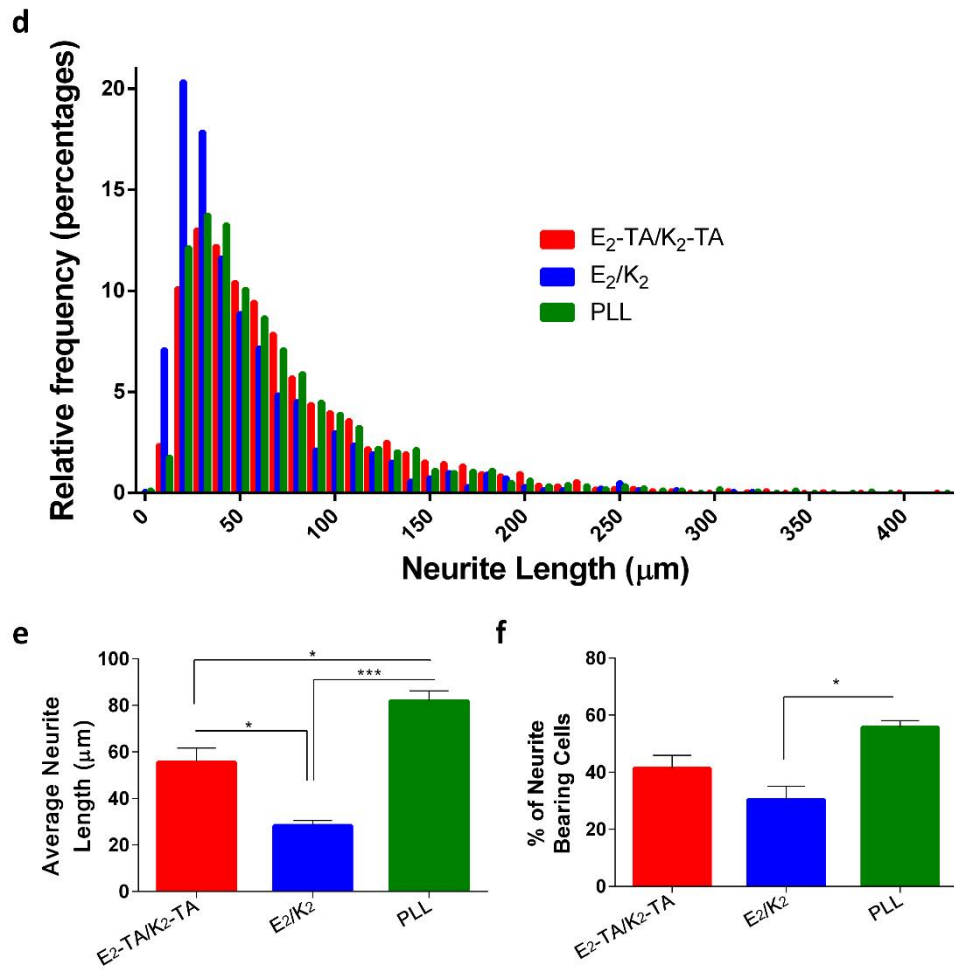
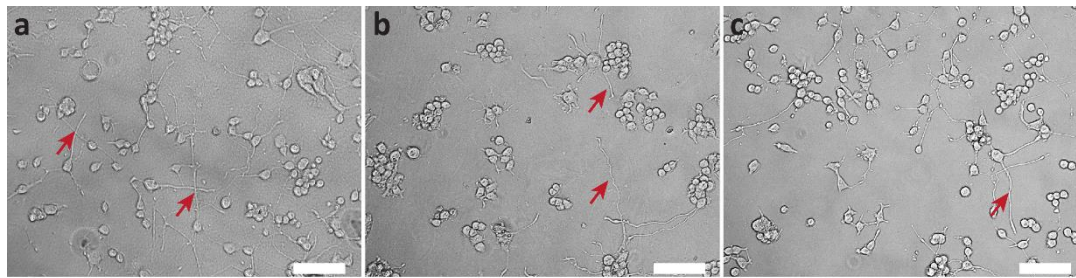


Figure 31 The effect of E₂-TA/K₂-TA gels on neural differentiation, the neurite processes of PC-12 cells. Bright field images of neurite outgrowth of PC-12 cells on E₂-TA/K₂-TA, E₂/K₂ gel and PLL coated surfaces (a-c), scale bars=100 μm. Percentage relative frequency distribution of neurite lengths (d). Average neurite length and percentage of neurite bearing PC-12 cells on E₂-TA/K₂-TA and E₂/K₂ gels and PLL coated surfaces (e-f).

positive control in neurite outgrowth analyses (Figure 31e). The rate of neurite bearing cells did not significantly change for E₂-TA/K₂-TA gels compared to E₂/K₂ gels (Figure 31f). This is probably due to short neurites on E₂/K₂ gels increasing the number of neurite bearing cells, but not the average neurite length, gels on the histogram data (Figure 31d). Also, neural differentiation of PC-12 cells on E₂-TA/K₂-TA scaffolds was also observed to be NGF dependent (Figure 33).

Table 1 Histogram data of relative percentage frequency distribution of neurite length values on E₂-TA/K₂-TA and E₂/K₂ gels and PLL.

	E₂-TA/K₂-TA	E₂/K₂	PLL
25% Percentile	34.5	23.9	32.8
Median	57.3	39.4	53.4
75% Percentile	93.5	68.1	90.2
Maximum	416.3	320.6	417.5

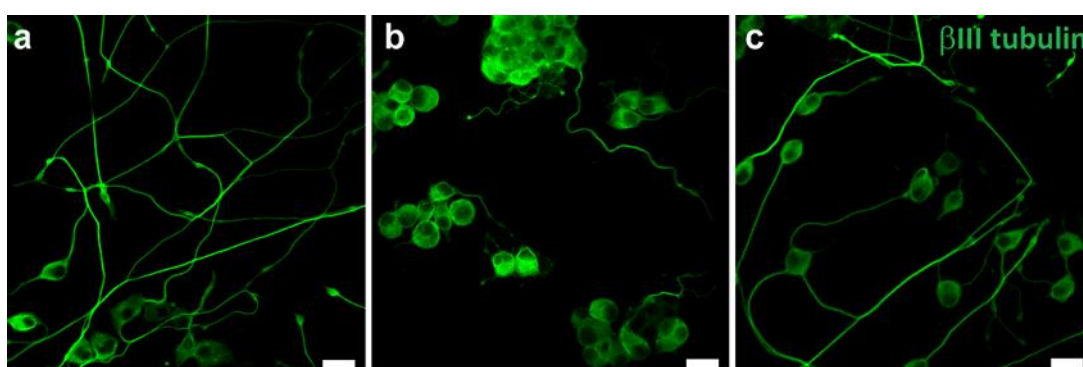


Figure 32 Confocal images of β III tubulin stained PC-12 cells grown on E₂-TA/K₂-TA, E₂/K₂ gel and PLL coated surfaces (a-c). Scale bars=20 μ m.

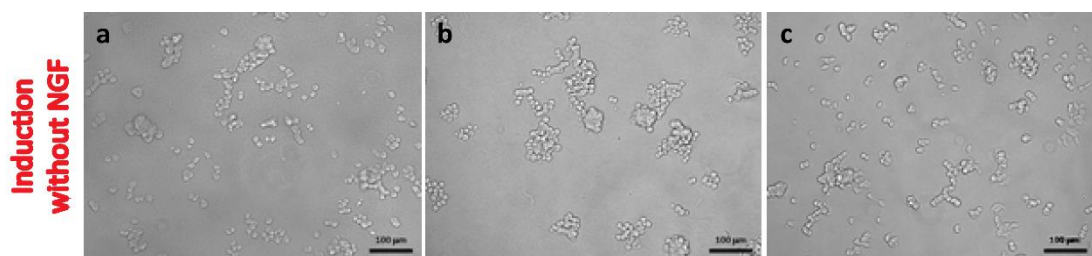


Figure 33 Bright-field images of PC-12 cells on E₂-TA/K₂-TA, E₂/K₂ gels and PLL coated surfaces on day 6 without NGF induction (a-c).

We also investigated the upstream pathways of NGF-induced neural differentiation. Upon binding of NGF to the TrkA surface receptor, a set of signaling pathways including Mitogen activated protein kinase/Extracellular signal-regulated kinase 1/2 (MAPK/ERK) signaling as the major one, as well as AKT and protein kinase C (PKC) pathways are initiated on PC-12 cells, resulting in activation of genes that play role in neuronal differentiation. In the literature, the ERK1/2 pathway was also seen to be phosphorylated in case of electrical stimulation [135]. It remains to be determined exactly which pathways take place in electrical stimulation or conductive scaffold mediated neurite outgrowth. However, here we observed an upregulation of the phosphorylation level of the ERK1/2 pathway (Figure 34). Although the cells were primed with the same amount of NGF, 20 ng/mL, upregulation of this pathway on E₂-TA/K₂-TA might suggest that intrinsic microcurrents of the cells have been enhanced by the conductive scaffold.

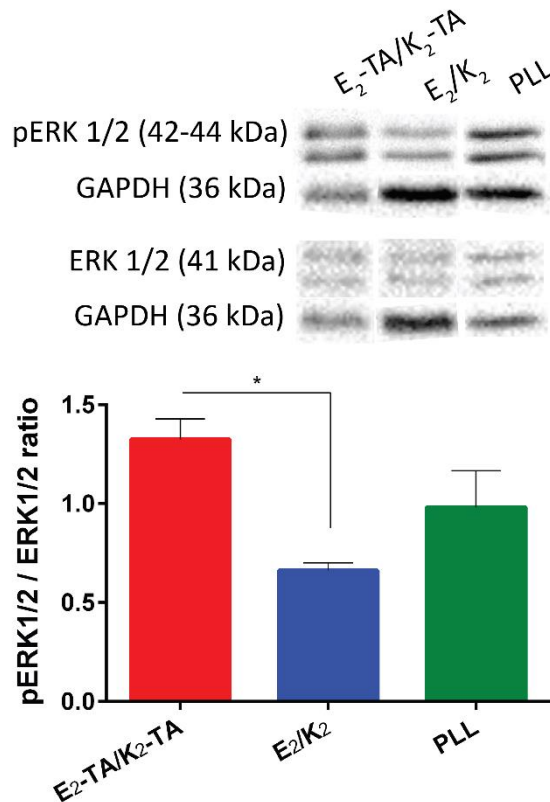


Figure 34 Protein expression levels of ERK1/2 phosphorylation of PC-12 cells cultured on E₂-TA/K₂-TA and E₂/K₂ gels and PLL coated surfaces. Data presented as mean±SEM (n=3), *p<0.05.

Conductive biomaterials have been extensively explored for many biomedical applications. The electrical excitability and the intrinsic electrical connectivity of the nature of the nerve tissue make conductive biomaterials promising candidates for nerve injury therapies. These types of materials can be used as scaffolds, films or coating materials, however tuning the mechanical, topographical and biological properties of the biomaterial expedites the integration of the regenerating host tissue. Ideally, the scaffold should mimic the host tissue. Here we showed an

electroactive, nanofibrous peptide hydrogel system for improved neural differentiation of model cell line PC-12.

3.4.2. Conclusion and Future Perspectives

To date, many different materials have been used to support and induce the regenerative capacity of the nervous tissue. Biomaterial scaffold applications have been considered as a promising approach in terms of providing a physical, mechanical and topographical substrate to support cell adhesion, proliferation and differentiation. These biomaterials include synthetic polymers, natural polymers or composites of synthetic and natural polymers [136]. Synthetic materials are advantageous since it is relatively easier to manipulate their mechanical or topographical properties. Within this class of materials, natural ones are recently preferred in order not to cause an aberrant activity in the body; however, to create the necessary effect, finding the balance between the expediency and the biocompatibility is vital. Hydrogels have a particular importance in this category because of their soft structure.

Conductive materials are known to promote neural differentiation and axon elongation, with and partially without electrical stimulation. However, it has always been a problem to use conductive polymers as films in soft tissue engineering because of their rigid, brittle and nonbiodegradable function.

In this study, we showed TA containing peptide conjugates that can self-assemble into a fibrillar network structure at neutral conditions and show electroactivity. E₂-TA/K₂-TA scaffolds showed good biocompatibility towards PC-12 cells and did not

alter the metabolic activity of the cells. Our results suggest that neural differentiation of PC-12 cells was enhanced when cultured on E₂-TA/K₂-TA gels. Also, we observed that phosphorylation levels of ERK1/2 were increased on PC-12 cells on the conductive scaffolds compared to the nonconductive nanofiber gels. The E₂-TA/K₂-TA gels could be used as a promising material in peripheral nerve regeneration. Further studies should be performed to test the performance of the material in *in vivo* peripheral nerve injury models and investigate the mechanism of improved neural differentiation.

Bibliography

- [1] M. J. Webber, E. A. Appel, E. Meijer, and R. Langer, "Supramolecular biomaterials," *Nature materials*, vol. 15, p. 13, 2016.
- [2] C. Schmitz-Antoniak, "X-ray absorption spectroscopy on magnetic nanoscale systems for modern applications," *Reports on Progress in Physics*, vol. 78, p. 062501, 2015.
- [3] S. Yao, X. Liu, X. Wang, A. Merolli, X. Chen, and F. Cui, "Directing neural stem cell fate with biomaterial parameters for injured brain regeneration," *Progress in Natural Science: Materials International*, vol. 23, pp. 103-112, 2013.
- [4] H. S. Nalwa, "A special issue on reviews in biomedical applications of nanomaterials, tissue engineering, stem cells, bioimaging, and toxicity," *Journal of biomedical nanotechnology*, vol. 10, pp. 2421-2423, 2014.
- [5] R. W. Siegel and G. E. Fougere, "Mechanical properties of nanophase metals," *Nanostructured Materials*, vol. 6, pp. 205-216, 1995.

- [6] B. D. Fahlman, "Semiconducting Materials," in *Materials Chemistry*, ed: Springer, 2007, pp. 153-219.
- [7] L. Zhang and T. J. Webster, "Nanotechnology and nanomaterials: promises for improved tissue regeneration," *Nano today*, vol. 4, pp. 66-80, 2009.
- [8] R. Langer and J. Vacanti, "1993Tissue engineering," *Science*, vol. 260, pp. 920-927, 1993.
- [9] A. Solanki, J. D. Kim, and K.-B. Lee, "Nanotechnology for regenerative medicine: nanomaterials for stem cell imaging," *Nanomedicine*, vol. 3, pp. 567-578, 2008.
- [10] P. Kerativitayanan, J. K. Carrow, and A. K. Gaharwar, "Nanomaterials for engineering stem cell responses," *Advanced healthcare materials*, vol. 4, pp. 1600-1627, 2015.
- [11] R. Murugan and S. Ramakrishna, "Design strategies of tissue engineering scaffolds with controlled fiber orientation," *Tissue engineering*, vol. 13, pp. 1845-1866, 2007.
- [12] M. J. Webber, E. J. Berns, and S. I. Stupp, "Supramolecular nanofibers of peptide amphiphiles for medicine," *Israel journal of chemistry*, vol. 53, pp. 530-554, 2013.
- [13] S. J. Singer and G. L. Nicolson, "The fluid mosaic model of the structure of cell membranes," *Science*, vol. 175, pp. 720-731, 1972.
- [14] M. D. Shoulders and R. T. Raines, "Collagen structure and stability," *Annual review of biochemistry*, vol. 78, pp. 929-958, 2009.
- [15] E. Nogales and H.-W. Wang, "Structural mechanisms underlying nucleotide-dependent self-assembly of tubulin and its relatives," *Current opinion in structural biology*, vol. 16, pp. 221-229, 2006.
- [16] J. B. Matson and S. I. Stupp, "Self-assembling peptide scaffolds for regenerative medicine," *Chemical communications*, vol. 48, pp. 26-33, 2012.

- [17] J. D. Hartgerink, E. R. Zubarev, and S. I. Stupp, "Supramolecular one-dimensional objects," *Current Opinion in Solid State and Materials Science*, vol. 5, pp. 355-361, 2001.
- [18] R. P. Nagarkar and J. P. Schneider, "Synthesis and primary characterization of self-assembled peptide-based hydrogels," *Nanostructure design: methods and protocols*, pp. 61-77, 2008.
- [19] J. M. Palomo, "Solid-phase peptide synthesis: an overview focused on the preparation of biologically relevant peptides," *RSC Advances*, vol. 4, pp. 32658-32672, 2014.
- [20] S. Zhang, "Emerging biological materials through molecular self-assembly," *Biotechnology advances*, vol. 20, pp. 321-339, 2002.
- [21] X.-D. Xu, Y. Jin, Y. Liu, X.-Z. Zhang, and R.-X. Zhuo, "Self-assembly behavior of peptide amphiphiles (PAs) with different length of hydrophobic alkyl tails," *Colloids and Surfaces B: Biointerfaces*, vol. 81, pp. 329-335, 2010.
- [22] T. Courtney, M. S. Sacks, J. Stankus, J. Guan, and W. R. Wagner, "Design and analysis of tissue engineering scaffolds that mimic soft tissue mechanical anisotropy," *Biomaterials*, vol. 27, pp. 3631-3638, 2006.
- [23] I. Hamley, "Self-assembly of amphiphilic peptides," *Soft Matter*, vol. 7, pp. 4122-4138, 2011.
- [24] J. T. Rutka, G. Apodaca, R. Stern, and M. Rosenblum, "The extracellular matrix of the central and peripheral nervous systems: structure and function," *J Neurosurg*, vol. 69, pp. 155-70, Aug 1988.
- [25] W. Pan, W. A. Banks, and A. J. Kastin, "Permeability of the blood-brain and blood-spinal cord barriers to interferons," *Journal of neuroimmunology*, vol. 76, pp. 105-111, 1997.

- [26] P. D. Yurchenco and Y. Cheng, "Laminin self-assembly: a three-arm interaction hypothesis for the formation of a network in basement membranes," 1994.
- [27] A. Aszodi, K. R. Legate, I. Nakchbandi, and R. Fassler, "What mouse mutants teach us about extracellular matrix function," *Annu Rev Cell Dev Biol*, vol. 22, pp. 591-621, 2006.
- [28] T. Hubert, S. Grimal, P. Carroll, and A. Fichard-Carroll, "Collagens in the developing and diseased nervous system," *Cellular and molecular life sciences*, vol. 66, pp. 1223-1238, 2009.
- [29] G. J. Siegel, B. W. Agranoff, R. W. Albers, S. K. Fisher, M. D. Uhler, and D. E. Pleasure, "Regeneration in the Central and Peripheral Nervous Systems," 1999.
- [30] M. B. Bunge, P. M. Wood, L. B. Tynan, and M. L. Bates, "Perineurium originates from fibroblasts: demonstration in vitro with a retroviral marker," *Science*, vol. 243, pp. 229-231, 1989.
- [31] M. H. Verheijen, R. Chrast, P. Burrola, and G. Lemke, "Local regulation of fat metabolism in peripheral nerves," *Genes Dev*, vol. 17, pp. 2450-64, Oct 1 2003.
- [32] R. P. Bunge, "Expanding roles for the Schwann cell: ensheathment, myelination, trophism and regeneration," *Curr Opin Neurobiol*, vol. 3, pp. 805-9, Oct 1993.
- [33] G. B. Shellswell, D. J. Restall, V. C. Duance, and A. J. Bailey, "Identification and differential distribution of collagen types in the central and peripheral nervous systems," *FEBS Lett*, vol. 106, pp. 305-8, Oct 15 1979.
- [34] R. Milner, M. Wilby, S. Nishimura, K. Boylen, G. Edwards, J. Fawcett, *et al.*, "Division of labor of Schwann cell integrins during migration on peripheral nerve extracellular matrix ligands," *Developmental biology*, vol. 185, pp. 215-228, 1997.

- [35] M. V. Tsiper and P. D. Yurchenco, "Laminin assembles into separate basement membrane and fibrillar matrices in Schwann cells," *J Cell Sci*, vol. 115, pp. 1005-15, Mar 1 2002.
- [36] G. Koopmans, B. Hasse, and N. Sinis, "Chapter 19: The role of collagen in peripheral nerve repair," *Int Rev Neurobiol*, vol. 87, pp. 363-79, 2009.
- [37] M. A. Chernousov, K. Rothblum, R. C. Stahl, A. Evans, L. Prentiss, and D. J. Carey, "Glypican-1 and $\alpha 4$ (V) collagen are required for Schwann cell myelination," *The Journal of neuroscience*, vol. 26, pp. 508-517, 2006.
- [38] B. G. Hudson, S. T. Reeders, and K. Tryggvason, "Type IV collagen: structure, gene organization, and role in human diseases. Molecular basis of Goodpasture and Alport syndromes and diffuse leiomyomatosis," *J Biol Chem*, vol. 268, pp. 26033-6, Dec 15 1993.
- [39] T. F. Eather, M. Pollock, and D. B. Myers, "Proximal and distal changes in collagen content of peripheral nerve that follow transection and crush lesions," *Experimental neurology*, vol. 92, pp. 299-310, 1986.
- [40] A. M. Sheppard, S. K. Hamilton, and A. L. Pearlman, "Changes in the distribution of extracellular matrix components accompany early morphogenetic events of mammalian cortical development," *The Journal of neuroscience*, vol. 11, pp. 3928-3942, 1991.
- [41] Z. Ahmed and R. A. Brown, "Adhesion, alignment, and migration of cultured Schwann cells on ultrathin fibronectin fibres," *Cell Motil Cytoskeleton*, vol. 42, pp. 331-43, 1999.
- [42] K. H. Braunewell, P. Pesheva, J. B. McCarthy, L. T. Furcht, B. Schmitz, and M. Schachner, "Functional involvement of sciatic nerve-derived versican- and decorin-like molecules and other chondroitin sulphate proteoglycans in ECM-

mediated cell adhesion and neurite outgrowth," *Eur J Neurosci*, vol. 7, pp. 805-14, Apr 1 1995.

- [43] A. Waller, "Experiments on the section of the glossopharyngeal and hypoglossal nerves of the frog, and observations of the alterations produced thereby in the structure of their primitive fibres," *Philosophical Transactions of the Royal Society of London*, vol. 140, pp. 423-429, 1850.
- [44] J. W. GRIFFIN, E. B. GEORGE, S.-T. HSIEH, and J. D. GLASS, "Axonal degeneration and disorders of the axonal cytoskeleton," *The Axon: Structure, Function, and Pathophysiology*, p. 375, 1995.
- [45] R. Gilliatt and R. Hjorth, "Nerve conduction during Wallerian degeneration in the baboon," *Journal of Neurology, Neurosurgery & Psychiatry*, vol. 35, pp. 335-341, 1972.
- [46] D. P. Stirling and P. K. Stys, "Mechanisms of axonal injury: internodal nanocomplexes and calcium deregulation," *Trends in molecular medicine*, vol. 16, pp. 160-170, 2010.
- [47] M. S. Wang, A. A. Davis, D. G. Culver, Q. Wang, J. C. Powers, and J. D. Glass, "Calpain inhibition protects against Taxol-induced sensory neuropathy," *Brain*, vol. 127, pp. 671-679, 2004.
- [48] S. Y. Fu and T. Gordon, "The cellular and molecular basis of peripheral nerve regeneration," *Molecular neurobiology*, vol. 14, pp. 67-116, 1997.
- [49] L. R. Williams, F. M. Longo, H. C. Powell, G. Lundborg, and S. Varon, "Spatial-temporal progress of peripheral nerve regeneration within a silicone chamber: Parameters for a bioassay," *Journal of comparative neurology*, vol. 218, pp. 460-470, 1983.

- [50] I. V. Yannas, M. Zhang, and M. H. Spilker, "Standardized criterion to analyze and directly compare various materials and models for peripheral nerve regeneration," *Journal of Biomaterials Science, Polymer Edition*, vol. 18, pp. 943-966, 2007.
- [51] J. Silver and J. H. Miller, "Regeneration beyond the glial scar," *Nat Rev Neurosci*, vol. 5, pp. 146-56, Feb 2004.
- [52] T. G. Bush, N. Puvanachandra, C. H. Horner, A. Polito, T. Ostefeld, C. N. Svendsen, *et al.*, "Leukocyte infiltration, neuronal degeneration, and neurite outgrowth after ablation of scar-forming, reactive astrocytes in adult transgenic mice," *Neuron*, vol. 23, pp. 297-308, Jun 1999.
- [53] J. W. Fawcett and R. A. Asher, "The glial scar and central nervous system repair," *Brain Res Bull*, vol. 49, pp. 377-91, Aug 1999.
- [54] A. Alovskaya, T. Alekseeva, J. Phillips, V. King, and R. Brown, "Fibronectin, collagen, fibrin-components of extracellular matrix for nerve regeneration," *Topics in Tissue Engineering*, vol. 3, pp. 1-26, 2007.
- [55] P. H. Larsen, J. E. Wells, W. B. Stallcup, G. Opdenakker, and V. W. Yong, "Matrix metalloproteinase-9 facilitates remyelination in part by processing the inhibitory NG2 proteoglycan," *The Journal of neuroscience*, vol. 23, pp. 11127-11135, 2003.
- [56] J. C. Kwok, D. Carulli, and J. W. Fawcett, "In vitro modeling of perineuronal nets: hyaluronan synthase and link protein are necessary for their formation and integrity," *J Neurochem*, vol. 114, pp. 1447-59, Sep 1 2010.
- [57] X. Tang, J. E. Davies, and S. J. Davies, "Changes in distribution, cell associations, and protein expression levels of NG2, neurocan, phosphacan, brevican, versican V2, and tenascin-C during acute to chronic maturation of spinal cord scar tissue," *Journal of neuroscience research*, vol. 71, pp. 427-444, 2003.

- [58] A. S. Hunanyan, G. Garcia-Alias, J. M. Levine, J. W. Fawcett, L. M. Mendell, and V. L. Arvanian, "Role of chondroitin sulfate proteoglycans (CSPGs) in synaptic plasticity and neurotransmission in mammalian spinal cord," 2009.
- [59] C. G. Becker and T. Becker, "Repellent guidance of regenerating optic axons by chondroitin sulfate glycosaminoglycans in zebrafish," *The Journal of neuroscience*, vol. 22, pp. 842-853, 2002.
- [60] K. Sharma, M. E. Selzer, and S. Li, "Scar-mediated inhibition and CSPG receptors in the CNS," *Exp Neurol*, vol. 237, pp. 370-8, Oct 2012.
- [61] R. J. McKeon, M. J. Jurynek, and C. R. Buck, "The chondroitin sulfate proteoglycans neurocan and phosphacan are expressed by reactive astrocytes in the chronic CNS glial scar," *The Journal of Neuroscience*, vol. 19, pp. 10778-10788, 1999.
- [62] L. L. Jones, R. U. Margolis, and M. H. Tuszynski, "The chondroitin sulfate proteoglycans neurocan, brevican, phosphacan, and versican are differentially regulated following spinal cord injury," *Experimental neurology*, vol. 182, pp. 399-411, 2003.
- [63] T. L. Dickendesher, K. T. Baldwin, Y. A. Mironova, Y. Koriyama, S. J. Raiker, K. L. Askew, *et al.*, "NgR1 and NgR3 are receptors for chondroitin sulfate proteoglycans," *Nat Neurosci*, vol. 15, pp. 703-12, May 2012.
- [64] A. Faroni, S. A. Mobasseri, P. J. Kingham, and A. J. Reid, "Peripheral nerve regeneration: experimental strategies and future perspectives," *Adv Drug Deliv Rev*, vol. 82-83, pp. 160-7, Mar 2015.
- [65] G. Stoll, J. W. Griffin, C. Y. Li, and B. D. Trapp, "Wallerian degeneration in the peripheral nervous system: participation of both Schwann cells and macrophages in myelin degradation," *J Neurocytol*, vol. 18, pp. 671-83, Oct 1989.

- [66] V. Chaudhry, J. D. Glass, and J. W. Griffin, "Wallerian degeneration in peripheral nerve disease," *Neurol Clin*, vol. 10, pp. 613-27, Aug 1992.
- [67] C. E. Schmidt and J. B. Leach, "Neural tissue engineering: strategies for repair and regeneration," *Annu Rev Biomed Eng*, vol. 5, pp. 293-347, 2003.
- [68] S. K. Lee and S. W. Wolfe, "Peripheral nerve injury and repair," *J Am Acad Orthop Surg*, vol. 8, pp. 243-52, Jul-Aug 2000.
- [69] J. J. Bernstein and W. J. Goldberg, "Experimental spinal cord transplantation as a mechanism of spinal cord regeneration," *Paraplegia*, vol. 33, pp. 250-3, May 1995.
- [70] T. Carlstedt, "Nerve fibre regeneration across the peripheral-central transitional zone," *J Anat*, vol. 190 (Pt 1), pp. 51-6, Jan 1997.
- [71] K. R. Bulsara, B. J. Iskandar, A. T. Villavicencio, and J. H. Skene, "A new millenium for spinal cord regeneration: growth-associated genes," *Spine (Phila Pa 1976)*, vol. 27, pp. 1946-9, Sep 1 2002.
- [72] A. M. Avellino, D. Hart, A. T. Dailey, M. MacKinnon, D. Ellegala, and M. Kliot, "Differential macrophage responses in the peripheral and central nervous system during wallerian degeneration of axons," *Exp Neurol*, vol. 136, pp. 183-98, Dec 1995.
- [73] R. J. McKeon, R. C. Schreiber, J. S. Rudge, and J. Silver, "Reduction of neurite outgrowth in a model of glial scarring following CNS injury is correlated with the expression of inhibitory molecules on reactive astrocytes," *J Neurosci*, vol. 11, pp. 3398-411, Nov 1991.
- [74] C. Redies, "Cadherins and the formation of neural circuitry in the vertebrate CNS," *Cell and tissue research*, vol. 290, pp. 405-413, 1997.

- [75] M. B. Luskin, "Restricted proliferation and migration of postnatally generated neurons derived from the forebrain subventricular zone," *Neuron*, vol. 11, pp. 173-189, 1993.
- [76] F. H. Gage, "Mammalian neural stem cells," *Science*, vol. 287, pp. 1433-1438, 2000.
- [77] C. Lois and A. Alvarez-Buylla, "Long-distance neuronal migration in the adult mammalian brain," *Science*, vol. 264, pp. 1145-1149, 1994.
- [78] R. Galli, A. Gritti, L. Bonfanti, and A. L. Vescovi, "Neural stem cells," *Circulation research*, vol. 92, pp. 598-608, 2003.
- [79] A. M. Parr, C. H. Tator, and A. Keating, "Bone marrow-derived mesenchymal stromal cells for the repair of central nervous system injury," *Bone marrow transplantation*, vol. 40, p. 609, 2007.
- [80] D. Bottai, R. Fiocco, F. Gelain, L. Defilippis, R. Galli, A. Gritti, *et al.*, "Neural stem cells in the adult nervous system," *Journal of hematotherapy & stem cell research*, vol. 12, pp. 655-670, 2003.
- [81] H. H. Chan, C. A. Wathen, M. Ni, and S. Zhuo, "Stem cell therapies for ischemic stroke: current animal models, clinical trials and biomaterials," *RSC Advances*, vol. 7, pp. 18668-18680, 2017.
- [82] N. J. Gardiner, "Integrins and the extracellular matrix: key mediators of development and regeneration of the sensory nervous system," *Developmental neurobiology*, vol. 71, pp. 1054-1072, 2011.
- [83] S.-i. Murase and A. F. Horwitz, "Deleted in colorectal carcinoma and differentially expressed integrins mediate the directional migration of neural precursors in the rostral migratory stream," *Journal of Neuroscience*, vol. 22, pp. 3568-3579, 2002.

- [84] S. Bovetti, P. Bovolin, I. Perroteau, and A. C. Puche, "Subventricular zone-derived neuroblast migration to the olfactory bulb is modulated by matrix remodelling," *European Journal of Neuroscience*, vol. 25, pp. 2021-2033, 2007.
- [85] R. Riopelle and K. Dow, "Functional interactions of neuronal heparan sulphate proteoglycans with laminin," *Brain research*, vol. 525, pp. 92-100, 1990.
- [86] K. E. Dow, S. Mirski, J. Roder, and R. Riopelle, "Neuronal proteoglycans: biosynthesis and functional interaction with neurons in vitro," *Journal of Neuroscience*, vol. 8, pp. 3278-3289, 1988.
- [87] J. Hatakeyama, Y. Wakamatsu, A. Nagafuchi, R. Kageyama, R. Shigemoto, and K. Shimamura, "Cadherin-based adhesions in the apical endfoot are required for active Notch signaling to control neurogenesis in vertebrates," *Development*, vol. 141, pp. 1671-1682, 2014.
- [88] S. Hansen, V. Berezin, and E. Bock, "Signaling mechanisms of neurite outgrowth induced by the cell adhesion molecules NCAM and N-cadherin," *Cellular and molecular life sciences*, vol. 65, pp. 3809-3821, 2008.
- [89] J. L. Bixby and R. Zhang, "Purified N-cadherin is a potent substrate for the rapid induction of neurite outgrowth," *The Journal of Cell Biology*, vol. 110, pp. 1253-1260, 1990.
- [90] J. C. Vega L, M. K. Lee, J. H. Jeong, C. E. Smith, K. Y. Lee, H. J. Chung, *et al.*, "Recapitulating cell-cell adhesion using n-cadherin biologically tethered to substrates," *Biomacromolecules*, vol. 15, pp. 2172-2179, 2014.
- [91] Y. Wang, Z. Xu, L. C. Kam, and P. Shi, "Site-Specific Differentiation of Neural Stem Cell Regulated by Micropatterned Multicomponent Interfaces," *Advanced healthcare materials*, vol. 3, pp. 214-220, 2014.

- [92] O. W. Blaschuk, R. Sullivan, S. David, and Y. Pouliot, "Identification of a cadherin cell adhesion recognition sequence," *Developmental biology*, vol. 139, pp. 227-229, 1990.
- [93] S. M. Burden-Gulley, T. J. Gates, S. E. Craig, S. F. Lou, S. A. Oblander, S. Howell, *et al.*, "Novel peptide mimetic small molecules of the HAV motif in N-cadherin inhibit N-cadherin-mediated neurite outgrowth and cell adhesion," *Peptides*, vol. 30, pp. 2380-2387, 2009.
- [94] Y. Shao, J. Sang, and J. Fu, "On human pluripotent stem cell control: The rise of 3D bioengineering and mechanobiology," *Biomaterials*, vol. 52, pp. 26-43, 2015.
- [95] J. T. Seil and T. J. Webster, "Electrically active nanomaterials as improved neural tissue regeneration scaffolds," *Wiley Interdisciplinary Reviews: Nanomedicine and Nanobiotechnology*, vol. 2, pp. 635-647, 2010.
- [96] R. B. Borgens, J. W. Vanable, and L. F. Jaffe, "Small artificial currents enhance *Xenopus* limb regeneration," *Journal of Experimental Zoology*, vol. 207, pp. 217-226, 1979.
- [97] E. Udina, M. Furey, S. Busch, J. Silver, T. Gordon, and K. Fouad, "Electrical stimulation of intact peripheral sensory axons in rats promotes outgrowth of their central projections," *Experimental neurology*, vol. 210, pp. 238-247, 2008.
- [98] L. M. Marquardt and S. E. Sakiyama-Elbert, "Engineering peripheral nerve repair," *Current opinion in biotechnology*, vol. 24, pp. 887-892, 2013.
- [99] C. E. Schmidt, V. R. Shastri, J. P. Vacanti, and R. Langer, "Stimulation of neurite outgrowth using an electrically conducting polymer," *Proceedings of the National Academy of Sciences*, vol. 94, pp. 8948-8953, 1997.
- [100] L. Ghasemi-Mobarakeh, M. P. Prabhakaran, M. Morshed, M. H. Nasr-Esfahani, H. Baharvand, S. Kiani, *et al.*, "Application of conductive polymers, scaffolds and

- electrical stimulation for nerve tissue engineering," *Journal of tissue engineering and regenerative medicine*, vol. 5, 2011.
- [101] M. Gajendiran, J. Choi, S.-J. Kim, K. Kim, H. Shin, H.-J. Koo, *et al.*, "Conductive biomaterials for tissue engineering applications," *Journal of Industrial and Engineering Chemistry*, 2017.
- [102] T. J. Rivers, T. W. Hudson, and C. E. Schmidt, "Synthesis of a novel, biodegradable electrically conducting polymer for biomedical applications," *Advanced Functional Materials*, vol. 12, pp. 33-37, 2002.
- [103] X. Wang, X. Gu, C. Yuan, S. Chen, P. Zhang, T. Zhang, *et al.*, "Evaluation of biocompatibility of polypyrrole in vitro and in vivo," *Journal of biomedical materials research Part A*, vol. 68, pp. 411-422, 2004.
- [104] P. M. George, D. A. LaVan, J. A. Burdick, C. Y. Chen, E. Liang, and R. Langer, "Electrically Controlled Drug Delivery from Biotin-Doped Conductive Polypyrrole," *Advanced Materials*, vol. 18, pp. 577-581, 2006.
- [105] Y. Li, K. G. Neoh, and E.-T. Kang, "Plasma protein adsorption and thrombus formation on surface functionalized polypyrrole with and without electrical stimulation," *Journal of colloid and interface science*, vol. 275, pp. 488-495, 2004.
- [106] N. K. Guimard, N. Gomez, and C. E. Schmidt, "Conducting polymers in biomedical engineering," *Progress in Polymer Science*, vol. 32, pp. 876-921, Aug-Sep 2007.
- [107] C. E. Schmidt, V. R. Shastri, J. P. Vacanti, and R. Langer, "Stimulation of neurite outgrowth using an electrically conducting polymer," *Proc Natl Acad Sci U S A*, vol. 94, pp. 8948-53, Aug 19 1997.
- [108] Z. Zhang, M. Rouabhia, Z. Wang, C. Roberge, G. Shi, P. Roche, *et al.*, "Electrically Conductive Biodegradable Polymer Composite for Nerve Regeneration: Electricity-

- Stimulated Neurite Outgrowth and Axon Regeneration," *Artificial organs*, vol. 31, pp. 13-22, 2007.
- [109] G. Kang, R. Ben Borgens, and Y. N. Cho, "Well-Ordered Porous Conductive Polypyrrole as a New Platform for Neural Interfaces," *Langmuir*, vol. 27, pp. 6179-6184, May 17 2011.
- [110] X. Gu, F. Ding, and D. F. Williams, "Neural tissue engineering options for peripheral nerve regeneration," *Biomaterials*, vol. 35, pp. 6143-56, Aug 2014.
- [111] L. M. Y. Yu, N. D. Leipzig, and M. S. Shoichet, "Promoting neuron adhesion and growth," *Materials Today*, vol. 11, pp. 36-43, May 2008.
- [112] C. Ding, Y. Wang, and S. Zhang, "Synthesis and characterization of degradable electrically conducting copolymer of aniline pentamer and polyglycolide," *European Polymer Journal*, vol. 43, pp. 4244-4252, 2007.
- [113] H. T. Nguyen, C. Wei, J. K. Chow, L. Nguy, H. K. Nguyen, and C. E. Schmidt, "Electric field stimulation through a substrate influences Schwann cell and extracellular matrix structure," *Journal of neural engineering*, vol. 10, p. 046011, 2013.
- [114] C. D. McCaig, A. M. Rajniecek, B. Song, and M. Zhao, "Controlling cell behavior electrically: current views and future potential," *Physiological reviews*, vol. 85, pp. 943-978, 2005.
- [115] L. Yao, A. Pandit, S. Yao, and C. D. McCaig, "Electric field-guided neuron migration: a novel approach in neurogenesis," *Tissue Engineering Part B: Reviews*, vol. 17, pp. 143-153, 2011.
- [116] S. Sirivisoot, R. Pareta, and B. S. Harrison, "Protocol and cell responses in three-dimensional conductive collagen gel scaffolds with conductive polymer nanofibres for tissue regeneration," *Interface focus*, vol. 4, p. 20130050, 2014.

- [117] V. M. Tysseling-Mattiace, V. Sahni, K. L. Niece, D. Birch, C. Czeisler, M. G. Fehlings, *et al.*, "Self-assembling nanofibers inhibit glial scar formation and promote axon elongation after spinal cord injury," *J Neurosci*, vol. 28, pp. 3814-23, Apr 2 2008.
- [118] H. Cui, M. J. Webber, and S. I. Stupp, "Self-assembly of peptide amphiphiles: from molecules to nanostructures to biomaterials," *Biopolymers*, vol. 94, pp. 1-18, 2010.
- [119] G. A. Silva, "Neuroscience nanotechnology: progress, opportunities and challenges," *Nat Rev Neurosci*, vol. 7, pp. 65-74, Jan 2006.
- [120] G. A. Silva, C. Czeisler, K. L. Niece, E. Beniash, D. A. Harrington, J. A. Kessler, *et al.*, "Selective differentiation of neural progenitor cells by high-epitope density nanofibers," *Science*, vol. 303, pp. 1352-5, Feb 27 2004.
- [121] Z. Sun, L. Kuang, X. Jing, X. Wang, J. Li, and F. Wang, "Synthesis of phenyl/amino-capped tetraaniline by chemical and electrochemical methods," *Chemical Journal of Chinese Universities-Chinese*, vol. 23, pp. 496-99, 2002.
- [122] W. Lv, J. Feng, W. Yan, and C. F. Faul, "Self-assembly and pH response of electroactive liquid core-tetra (aniline) shell microcapsules," *Journal of Materials Chemistry B*, vol. 2, pp. 4720-4725, 2014.
- [123] N. J. Greenfield and G. D. Fasman, "Computed circular dichroism spectra for the evaluation of protein conformation," *Biochemistry*, vol. 8, pp. 4108-4116, 1969.
- [124] R. Huang, R. Su, W. Qi, J. Zhao, and Z. He, "Hierarchical, interface-induced self-assembly of diphenylalanine: formation of peptide nanofibers and microvesicles," *Nanotechnology*, vol. 22, p. 245609, 2011.
- [125] X. Huang, C. Li, S. Jiang, X. Wang, B. Zhang, and M. Liu, "Self-assembled spiral nanoarchitecture and supramolecular chirality in Langmuir-Blodgett films of an

- achiral amphiphilic barbituric acid," *Journal of the American Chemical Society*, vol. 126, pp. 1322-1323, 2004.
- [126] R. Garifullin and M. O. Guler, "Supramolecular chirality in self-assembled peptide amphiphile nanostructures," *Chemical Communications*, vol. 51, pp. 12470-12473, 2015.
- [127] Q. Wang, W. He, J. Huang, S. Liu, G. Wu, W. Teng, *et al.*, "Synthesis of water soluble, biodegradable, and electroactive polysaccharide crosslinker with aldehyde and carboxylic groups for biomedical applications," *Macromolecular bioscience*, vol. 11, pp. 362-372, 2011.
- [128] S. K. M. Nalluri, N. Shivarova, A. L. Kanibolotsky, M. Zelzer, S. Gupta, P. W. Frederix, *et al.*, "Conducting nanofibers and organogels derived from the self-assembly of tetrathiafulvalene-appended dipeptides," *Langmuir*, vol. 30, pp. 12429-12437, 2014.
- [129] C. U. Udeh, N. Fey, and C. F. Faul, "Functional block-like structures from electroactive tetra (aniline) oligomers," *Journal of Materials Chemistry*, vol. 21, pp. 18137-18153, 2011.
- [130] B. Guo, Y. Sun, A. Finne-Wistrand, K. Mustafa, and A.-C. Albertsson, "Electroactive porous tubular scaffolds with degradability and non-cytotoxicity for neural tissue regeneration," *Acta biomaterialia*, vol. 8, pp. 144-153, 2012.
- [131] H. Huang, W. Li, H. Wang, X. Zeng, Q. Wang, and Y. Yang, "Conducting hydrogels of tetraaniline-g-poly (vinyl alcohol) in situ reinforced by supramolecular nanofibers," *ACS applied materials & interfaces*, vol. 6, pp. 1595-1600, 2014.
- [132] L. Niu, J. Song, J. Li, N. Tao, M. Lu, and K. Fan, "Solvent effects on the gelation performance of melamine and 2-ethylhexylphosphoric acid mono-2-ethylhexyl ester in water-organic mixtures," *Soft Matter*, vol. 9, pp. 7780-7786, 2013.

- [133] Y.-J. Chang, C.-M. Hsu, C.-H. Lin, M. S.-C. Lu, and L. Chen, "Electrical stimulation promotes nerve growth factor-induced neurite outgrowth and signaling," *Biochimica et Biophysica Acta (BBA)-General Subjects*, vol. 1830, pp. 4130-4136, 2013.
- [134] J. A. Harrill and W. R. Mundy, "Quantitative assessment of neurite outgrowth in PC12 cells," *In Vitro Neurotoxicology: Methods and Protocols*, pp. 331-348, 2011.
- [135] Q. Wang, *Smart Materials for Tissue Engineering: Applications* vol. 25: Royal Society of Chemistry, 2017.
- [136] A. R. Murphy, A. Laslett, C. M. O'Brien, and N. R. Cameron, "Scaffolds for 3D In Vitro Culture of Neural Lineage Cells," *Acta Biomaterialia*, 2017.